Vibration Characteristic of Lightweight Sandwich Structure Interacting with Ambient Air

周囲空気と相互作用する軽量サンドイッチ構造の振動特性

Saharat Chanthanumataporn

Department of Aerospace Engineering

Graduate School of System Design

Tokyo Metropolitan University

August 2017

Vibration Characteristic of Lightweight Sandwich Structure Interacting with Ambient Air

周囲空気と相互作用する軽量サンドイッチ構造の振動特性

by

Saharat Chanthanumataporn
Student ID 13991574

Submitted to the Division of Aerospace Engineering,
Graduate School of System Design,
in partial fulfillment of the requirements for the degree of
Doctor of Philosophy in Aerospace Engineering
at
TOKYO METROPOLITAN UNIVERSITY
August 2017

Certified by advisor

Professor Naoyuki Watanabe
Division of Aerospace Engineering
Graduate School of System Design
Tokyo Metropolitan University

Doctoral thesis committee:

Professor Naoyuki Watanabe	Tokyo Metropolitan University (Chairman)
Professor Koichi Kitazono	Tokyo Metropolitan University
Professor Hironori Sahara	Tokyo Metropolitan University
Professor Ayumu Inasawa	Tokyo Metropolitan University

Abstract

Due to the extremely lightweight characteristic of sandwich structures, ambient air can significantly affect their natural frequency. In order to clarify the importance and magnitude of this effect, the natural frequency of a sandwich panel surrounded by air layer using experiment and numerical simulation was investigated in this study. The experiment setup based on modal testing was proposed with the feature of simulating air layer around the sandwich panel. The effect of air layer thickness was examined. The analytical model was formulated on the basis of sandwich theory and fluid-structure interaction analysis. The shear deformation of sandwich core was taken into account and the thickness of sandwich structure was included into the mesh model. The assumption of viscous incompressible flow was employed for the motion of air domain. The accuracy of the formulation was verified by comparing the obtained results with other analytical solutions and experimental results. The parametric studies on the effect of shear deformation and ambient air were conducted and the results indicate the necessity of taking into account these effects. As a conclusion, the experimental and numerical simulation results correspondingly demonstrated that when the air layer thickness becomes thinner than 3 mm, the fundamental natural frequency of sandwich panel greatly decreases of more than 80% as compared with the natural frequency without air effect.

Keywords: Sandwich panel; Lightweight structure; Natural frequency; Air effect; Air layer

Contents

List of Figures

List of Tables

Nomenclature

Symbols	Definition
b	Panel width
c	Speed of sound
$[C]$	System damping matrix
d	Panel lateral displacement
$\{d\}$	Nodal panel lateral displacement matrix
D_B	Panel flexural rigidity
D_f	Face flexural rigidity
E_c	Core Young's modulus
E_f	Face Young's modulus
f	Panel natural frequencies
G_c	Core effective shear stiffness
$[G_A^e]$	Air element coupling interface matrix
$[G_B^e]$	Panel element coupling interface matrix
$[H^e]$	Air element penalty matrix
$[K]$	System stiffness matrix
$[K_A^e]$	Air stiffness matrix
$[K_B^e]$	Panel stiffness matrix
L	Panel length
l	Panel element length
$[M]$	System mass matrix
$[M_A^e]$	Air element mass matrix
$[M_B^e]$	Panel element mass matrix
n	Vibrational mode order
$\boldsymbol{n}$	Normal unit vector on the coupled boundary surface
$\boldsymbol{n}_A$	Normal unit vector outward from the air region

$\boldsymbol{n}_B$	Normal unit vector outward from the panel region
N	Number of panel element
$\lfloor \mathrm{N_d} \rfloor$	Shape function matrix for the panel lateral displacement
$\lfloor \mathrm{N_p} \rfloor$	Shape function matrix for the air pressure
$\lfloor \mathrm{N_u} \rfloor$	Shape function matrix for the air velocity
p	Air pressure
$\{p\}$	Nodal air pressure term matrix
$[P^e]$	Air element pressure matrix
q	Lateral surface force acting on the panel
t	Time
t_a	Air layer thickness
t_b	Panel thickness
t_c	Core thickness
t_f	Face thickness
$\boldsymbol{u}$	Air velocity vector, $\boldsymbol{u} = (u,v)$
$\{\boldsymbol{u}\}$	Nodal air velocity vector matrix
$\boldsymbol{w}$	Global variable defined in entire system, which can be either $\boldsymbol{u}$ or λd
$\{\boldsymbol{w}\}$	System velocity vector matrix
$\boldsymbol{\sigma}_A$	Air stress tensor
$\boldsymbol{\sigma}_B$	Panel stress tensor
σ_{ij}	Stress tensor
σ_{A_n}	Normal stress component of air
σ_{B_n}	Normal stress component of panel
σ_{A_τ}	Tangent stress component of air
δ_{ij}	Kronecker delta
ε_p	Penalty parameter
λ	Complex eigenvalue

μ	Air viscosity coefficient
ρ_A	Air density
ρ_B	Panel mass per unit length
Ω_1	Panel domain
Ω_2	Air domain
ζ, η	Local coordinates
∇	Gradient operator
∇	Laplace operator

Chapter 1
Introduction

1.1 Background and literature review

1.1.1 Sandwich structure

Sandwich structures are extensively accepted in advance engineering applications (e.g., aeronautics, automobiles, marines, and buildings) because of their excellent strength-to-weight ratio, which results in significant weight reduction and efficiency improvement [1-5]. A typical sandwich structure consists of two thin face sheets and a thick core as illustrated in **Figure 1.1**. The face sheets, generally made of metals or composite materials are responsible for carrying in-plane and bending load. The core, commonly a lightweight structure such as aluminum honeycomb, is sandwiched between the face sheets to keep them in a designed distance. The core thickness is a main parameter that determines the bending stiffness of sandwich structures. To clarify the outstanding properties of sandwich structure, the comparative bending stiffness and weight of a sandwich structure with different core thickness are presented in **Figure 1.2**. The bending stiffness and weight of each condition are normalized by the values of two face sheets perfectly bonded without core. The condition of the perfectly bonded face sheets is equivalent to a typical homogeneous structure. By adding the core thickness, the bending stiffness efficiently improves but the weight slightly increases. This comparison answers the question, “Why sandwich structures are in continuous demand?”.

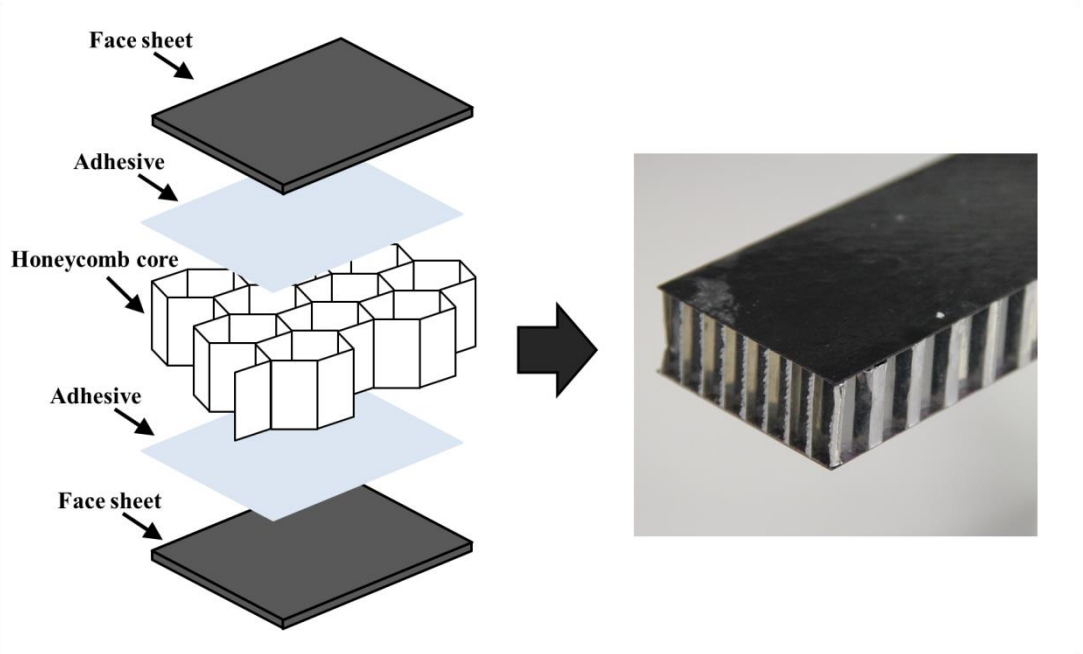

Figure 1.1 Honeycomb sandwich structure

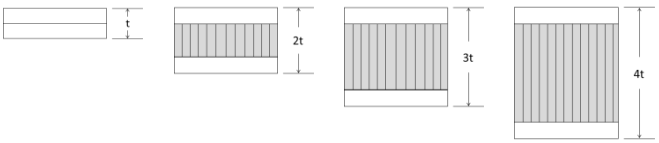

Comparative core thickness	0t	1t	2t	3t
Comparative Bending stiffness	1	7	19	37
Comparative Weight	1	1.02	1.04	1.06

Figure 1.2 Comparative core thickness, bending stiffness and weight of sandwich structure [6]

Due to the prominent characteristic of light weight and high bending stiffness, the honeycomb sandwich panel is commonly utilized as the main structure of satellite solar panel. To minimize the size of space shuttle, in launching process, the solar panels are generally arranged in folded configuration as shown in **Figure 1.3**.

However, because the solar panels are arranged in the earth's atmosphere, there are inevitably air layers presenting in the tolerance gap between the panels. Based on the condition of satellite solar panel in launching process, the vibration characteristic of honeycomb sandwich panel was studied and the influence of air layers presenting in the gap was also considered in this dissertation.

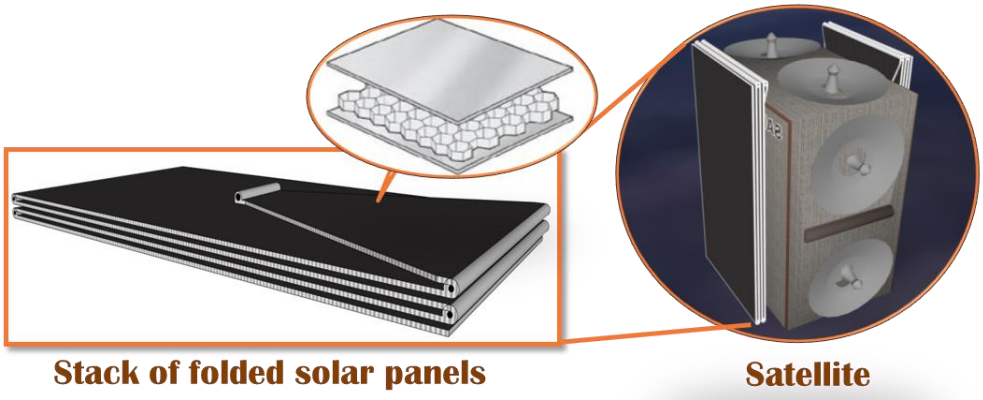

Figure 1.3 Satellite and solar panel

1.1.2 Vibration of sandwich structure

For structural verification, vibration test is a major requisite because almost all objects, when hit or disturbed, will vibrate and tend to vibrate at a particular frequency or a set of frequencies [7]. These frequencies are called that the natural frequency. The natural frequencies of each component must be estimated and may be redesigned to avoid the resonance with vibrational sources. The explanation based on the fundamental of vibration is given that a large amplitude of vibration presents when a natural frequency of any structure or part is matching with the operating frequency of any equipment [8-12]. For sandwich structures, bending vibration is an interesting case study that has been analyzed by various techniques. The simplest and

most functional technique is the approximation of Bernoulli-Euler theory, developed in the eighteenth century for describing the bending deformation of slender beams [13]. In the Bernoulli-Euler theory, the shear modulus is considered to be infinite and the bending deformation of a beam is relied on pure bending as shown in **Figure 1.4(a)**. In 1887, an improvement on the Bernoulli-Euler approximation was done by Lord Rayleigh [14]. This approximation is called Rayleigh beam model, in which the effect of rotational inertia of beam cross-section is taken into account [15]. Later, Shear beam approximation was developed by including shear deformation to the Bernoulli-Euler approximation. This model can considerably improve the estimated natural frequency [16]. In 1922, Timoshenko approximation was proposed, in which the effects of rotational inertia and shear deformation were included into the Bernoulli-Euler approximation [17]. This improvement makes the model to be suitable for thick beams with high frequency response [16]. The bending deformation of Shear/Timoshenko approximation is illustrated in **Figure 1.4(b)**.

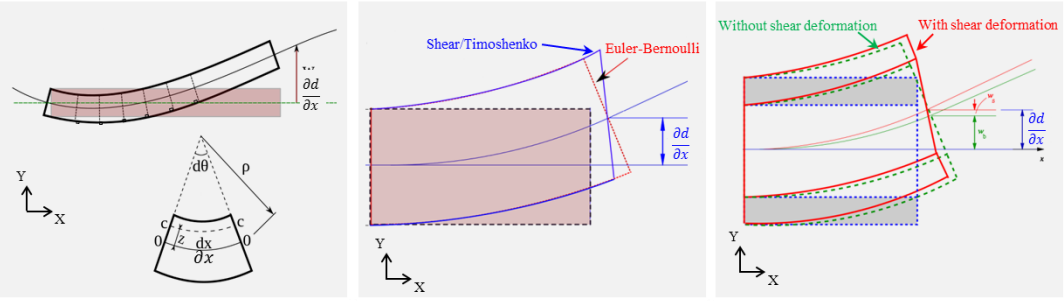

Figure 1.4 Bending deformation of **(a)** Bernoulli-Euler approximation **(b)** Shear/Timoshenko approximation **(c)** Sandwich approximation

However, the explained approximations are more suitable for homogeneous structures than for sandwich structures because the bending deformation of sandwich structure is quite different from that of homogenous structures as displayed in **Figure 1.4(c)**. Since the late nineteenth century, there have been an increasing number of researches on the flexural deformation of sandwich structures. DiTaranto, (1965) [18] and Mead and Markus, (1969) [19] proposed a sixth-order differential equation for describing the transverse motion of three-layer sandwich panels. In their model, the motion of laminates was based on the Bernoulli-Euler theory and the motion of core was estimated only from shear deformation. Mead, (1982) [20] introduced the sixth and eighth-order differential equations for defining the lateral displacement of symmetric and asymmetric sandwich panels, respectively. Nilsson, (1990) [21] exactly derived a model for governing the flexural deformation of three-layer sandwich panels. In this model, the laminates and core were considered to be isotropic and the effects of bending shear and rotation in core were included. Besides exact formulation, a governing equation can be formulated by variational technique. For example, the governing equations in References [22-25] were derived based on Hamilton's variational principle. Although, the high order differential equation up to tenth-order is investigated in References [24], their conclusion shows that only sixth-order equation is sufficient to govern the lateral displacement of sandwich panels for high frequency range up to 5 kHz. Moreover, Nilsson and Nilsson, (2002) [23] concluded that for typical lightweight sandwich structures, the effect of shear deformation tends to dominate that of rotational inertia.

1.1.3 Influence of ambient air

On lightweight structures, the influence of ambient air is very significant because it can alter the dynamic behaviors of the structures. Therefore, it is important to be included into the vibration analysis of light weight sandwich structures. A number of researches have discussed the dynamic response of air-coupled structures [23,26-38] Experimentation and/or numerical simulation were conducted in their studies to solve the problem of Fluid-Structure Interaction (FSI).

However, until present, there are few literatures that study the vibration of sandwich structures coupled with ambient air [23,28,34,35]. In 1966, Powell and Stephens [34] experimentally investigated the vibration characteristics of sandwich panels in various conditions of air density. This publication probably is the first study that discussed the vibration response of a sandwich structure coupled with ambient air. They performed the vibration testing in vacuum chamber as schematically shown in **Figure 1.5(a)**. The sandwich panel was excited from the bottom via spring supports and the vibration response was sensed by the lightweight piezoelectric crystal accelerometers mounted on the panel. By using this system, the first three natural frequencies were obtained over a pressure variation from 1 to 1.32×10^{-9} atm. Their conclusion was given that the effect of ambient air is in form of air added mass, which results in the decrease in natural frequency of 2 to 10% as compared with the natural frequency without air effect. Nilsson and Nilsson, (2002) [23] also conducted a vibration experiment in two pressure conditions; the first in vacuum situation and the second under normal pressure in order to investigate the effect of air added mass on a lightweight sandwich panel. As schematically shown in **Figure 1.5(b)**, the panel was

suspended in the vacuum chamber and excited by a shaker. The panel response was sensed by a laser vibrometer via a glass window on the vacuum chamber. They concluded that the added mass effect can disturb the first few natural frequencies of a lightweight panel, where the effect is of 30% of the panel actual mass and the effect is decreasing for increasing frequencies up to the critical frequency. For frequencies above the critical frequency, the acoustic radiation from the structure will increase the losses of the structure.

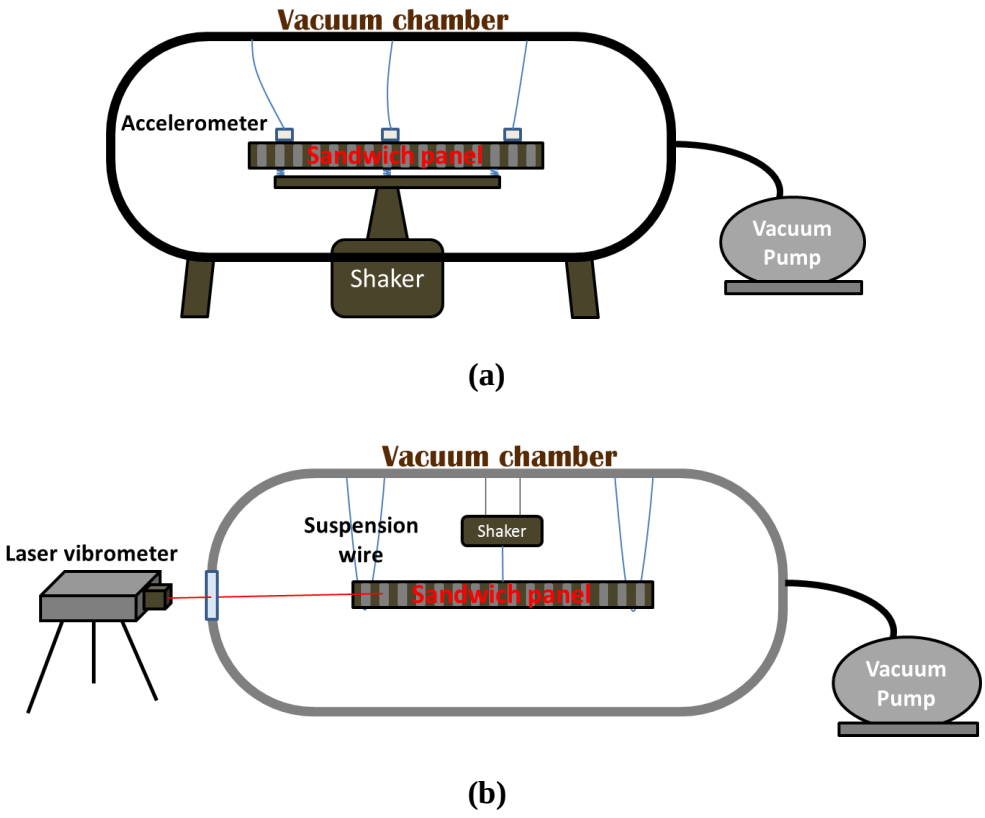

Figure 1.5 Vibration testing of sandwich panel in vacuum chamber performed by **(a)** Powell and Stephens [34] **(b)** Nilsson and Nilsson [23]

Besides, there are some literatures that investigating the vibration of sandwich panel coupled with air by using numerical analysis. Chimeno Manguán et al., (2014) [28] numerically simulated the vibro-acoustic response of a satellite solar array in folded configuration based on three difference approaches: finite element method (FEM), boundary element method (BEM), and statistical energy analysis (SEA). In this literature, the efficiency of each numerical approach was compared and the result showed that the FEM is an efficient technique for analysis in low frequency range. The FEM was also used in many researches for example in References [26,27]. The authors in References [26,27] performed a series of researches on the rigid and flexible plate coupled with a single air layer, where the assumption is the pressure constant across the air layer thickness. Moreover, they also conducted the vibration experiment, as schematically presented in **Figure 1.6**, to verify their numerical results. Their results were concluded that the thickness of air layer is an influential factor that can alter the air effect. In the condition of extremely thin air layer and low frequencies, the coupling of the air-structure is extremely strong and the viscous damping effect plays an important role in the dynamic behavior of the system. Their conclusions are also in agreement with the those of many literatures [26,27,29,32,37,38] that the thickness of air layer can significantly affect the structural natural frequencies; and the effect of air viscosity is more influential than that of compressibility especially for the problem of thin air layer.

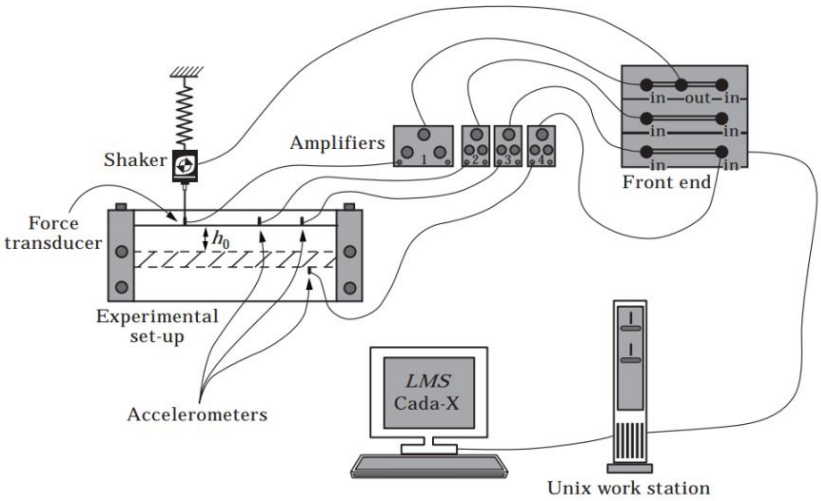

Figure 1.6 Vibration testing of flexible plate interacting with single air layer [27]

1.2 Problem statements and objectives of dissertation

After extensively reviewing the literatures, the stated problems are concluded below:

1. A few modal experiments of a sandwich panel coupled with air were found as described in the previous section. The indispensable influence of air layer thickness was frequently abandoned.

2. A few analytical models were proposed for studying the vibration of sandwich panel coupled with air. The available models focused on the configuration of single air layer and pressure constant across the layer thickness. However, the configuration of air layers fully enveloping the structure is more realistic than that of single air layer interacting with the structure. Although the assumption of constant pressure, extensively used in various literatures [29,32,33], can simplify the formulation and can provide practical results, it has some limitations that confine the thickness of air layer to be smaller than the acoustic wavelength of the system. For the structural

region, the sandwich structure was simply modelled as a homogeneous structure. Although, the homogeneous model is able to simplify the formulation, it is not sufficient for governing the lateral motion of the sandwich structure [39]. Another issue is that the thickness of the sandwich structure was not included into the boundary condition of the finite element mesh model. In the case of thin air layers fully enveloping the sandwich structure, the thickness of the structure is quite large as compared to the air layer thickness.

The described problem statements originate the inspiration of this dissertation. The objectives of this dissertation are listed below:

1. To establish an experimental modal testing with the feature of simulating an air layer around a sandwich panel and investigate the influence of ambient air layer on the natural frequency of the sandwich panel.

2. To formulate the analytical model for studying the vibration of a sandwich panel coupled with air, where the configuration of air layer fully enveloping the structure and the incorporation of pressure distribution across the layer are modelled. The sandwich panel is modelled based on sandwich theory and the sandwich panel thickness is included into the mesh model.

3. To numerically evaluate the influence of ambient air layer in various aspects and indicate the necessity of considering the shear deformation in sandwich core and of including the sandwich panel thickness into the mesh model.

1.3 Overview of dissertation

This dissertation is organized into 5 chapters as follows:

Chapter 1 presents the background, literature review, problem statements, objectives, and overview of this dissertation. Literature study on the vibration of sandwich structures is provided and various analytical models for describing the bending vibration are clarified. Literature reviews on the influence of the ambient air on the vibration of sandwich structures are presented. The pros and cons of the literatures have been concluded.

Chapter 2 describes the detail of experimental setup and the effect of ambient air layer on the fundamental natural frequency of a honeycomb sandwich panel. The experimental setup based on modal testing was proposed with the feature of simulating air layers around the sandwich panel. To clearly clarify the effect of air layer surrounding the sandwich panel, 15 conditions of air layer thickness were determined for performing modal testing.

Chapter 3 presents the concept and finite element formulation for analyzing free vibration of a sandwich panel coupled with ambient air. The model configuration is a vibrating flexible sandwich panel coupled with ambient air surrounded by rigid walls. The flexural vibration of a sandwich panel was described by the governing equation formulated based on the sandwich theory, where the shear deformation of sandwich assumption was employed. The penalty function method was applied for the formulation of the Navier-Stokes equations system to minimize the computational time and effort. Based on the methods of Galerkin weight residual and finite element, the governing equations were derived in weak-form and then a set of discrete matrix

equations. The coupled discrete matrix equation was derived based on the monolithic approach and eigenvalue problem. The implementation of finite element model is also provided in chapter 3. The types of element for discretizing the panel and air domain as well as the integral scheme are explained. The finite element mesh models including and excluding the panel thickness are illustrated.

Chapter 4 presents the results of parametric studies and discussions. In addition, the validation of the finite element model was examined by investigating the convergence of the obtained results and comparing the results with other analytical solutions and experimental results. The influences of shear deformation and ambient air on the natural frequencies of three honeycomb sandwich panel are studied to demonstrate the importance of each effects and the efficiency of the proposed finite element model. The shear modulus of sandwich core, the thickness of sandwich core, and the thickness of face sheets are varied to clarify the significance of considering the shear deformation effect for the studying the bending vibration of sandwich panels. In order to demonstrate the degree of ambient air effect, the parametric studies on the air layer thickness, viscosity, and density as well as the panel length, bending stiffness, mass density, and thickness are conducted.

Chapter 5 concludes the finding and achievement of this thesis. In addition, the recommendations for future research are summarized in this chapter.

Chapter 2
Experimental modal testing

2.1 Overview

As explained in Chapter 1, a few modal experiments of a sandwich panel coupled with air were found and the indispensable influence of air layer thickness was frequently abandoned. In this chapter, the modal experiment of a honeycomb sandwich panel coupled with ambient air layer was setup originally to study the effect of thin air layer on the natural frequency of the sandwich panel. The air layer surrounding the sandwich panel was implemented by fixing the sandwich panel in the specially designed air tight box, in which the air layer thickness can be adjusted. To clearly clarify the effect of air layer surrounding the sandwich panel, 15 conditions of air layer thickness were determined for performing modal testing.

2.2 Experimental setup

The testing system, as schematically illustrated in **Figure 2.1**, mainly consists of an air tight container, a sandwich specimen, an electromagnetic exciter, a force transducer, an optical displacement meter, and a FFT analyzer. The air tight box is specially designed for fixing the specimen and simulating the air layer surrounding the sandwich specimen. It composes of a base box and transparent acrylic cover. As shown in **Figure 2.2**, the base box is made with heavy weight stainless steel and securely fixed on the strong vibration test table in order to protect the vibration of the base box. The base box and cover are assembled by using bolts (M6×10) and a rubber

seal is installed between them to protect air leakage.

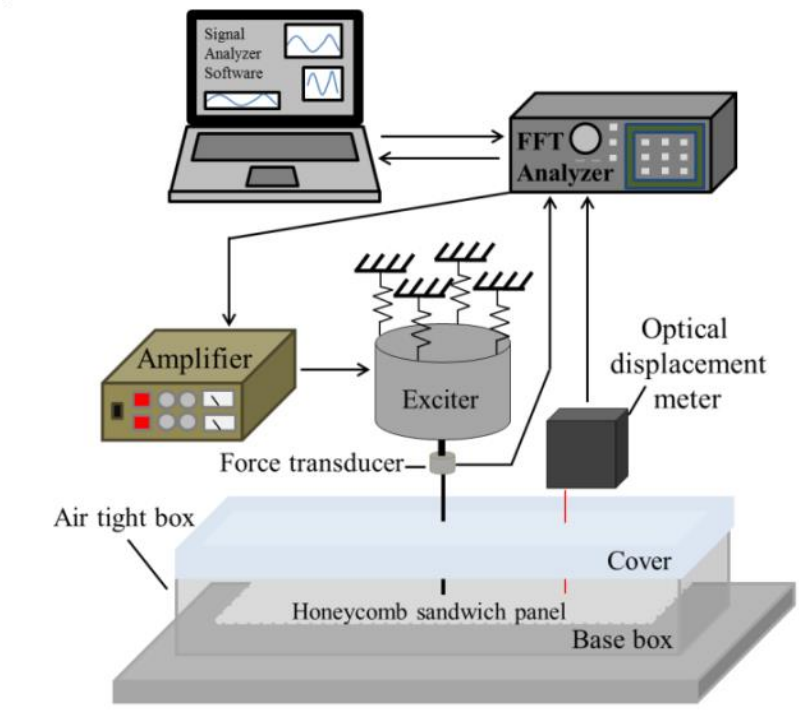

Figure 2.1 Experimental schematic diagram

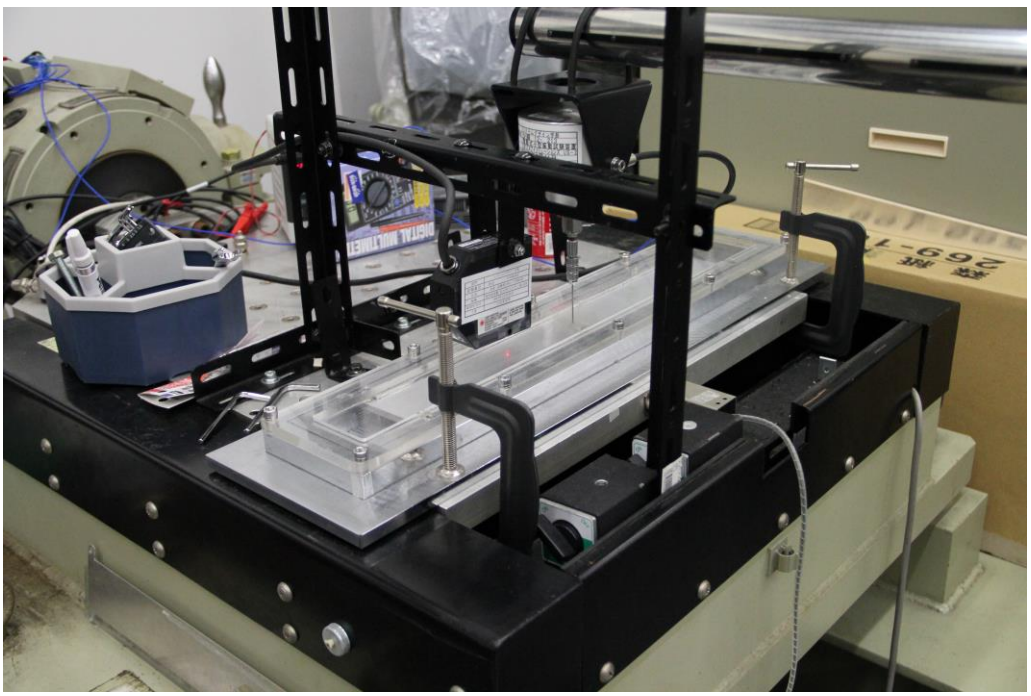

Figure 2.2 Experimental setup

The specimen used in this study is a honeycomb sandwich panel, manufactured by Showa Aircraft industry, Tokyo, Japan. The material used for the face laminates and honeycomb core is aluminum (AL5052). The picture and geometry of the specimen are presented in **Figure 2.3**. The shape of honeycomb core is hexagonal where the cell size is 5 mm and the cell wall thickness is 0.001 mm. The specifications are listed in **Table 2.1**. To perform the boundary condition of fixed ends, the brackets was specifically designed and fabricated to be seamlessly assembled with the specimen. As shown in **Figure 2.3** and **Figure 2.4**, a hole was drilled at each end of both bracket sides in order to securely fix the brackets and the base box with four bolts. As the brackets were fixed with the base box by bolts, they were considered to be the same part with the base box. With this design, the brackets allow the stability for fixing the specimen with fixed ends condition.

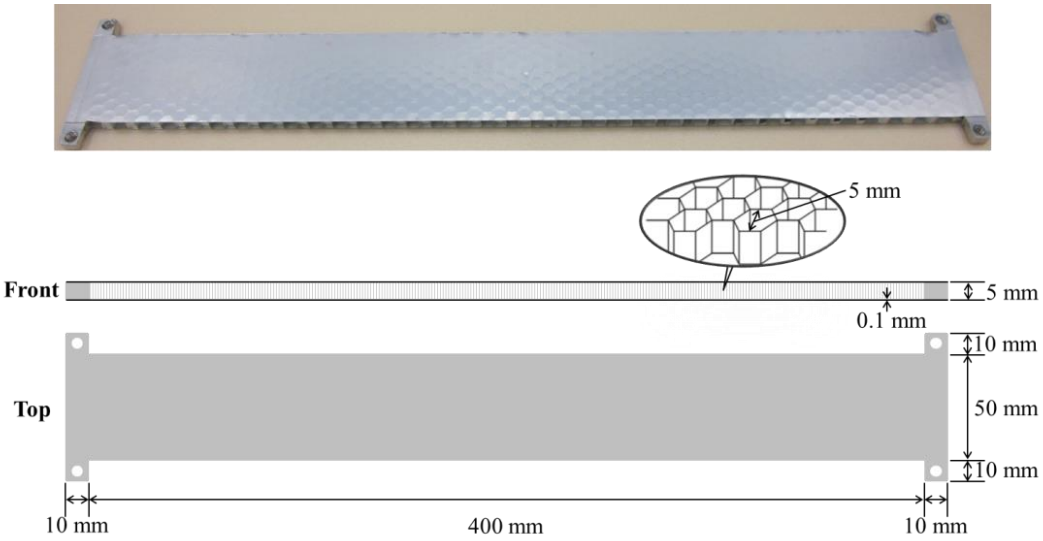

Figure 2.3 Honeycomb sandwich specimen

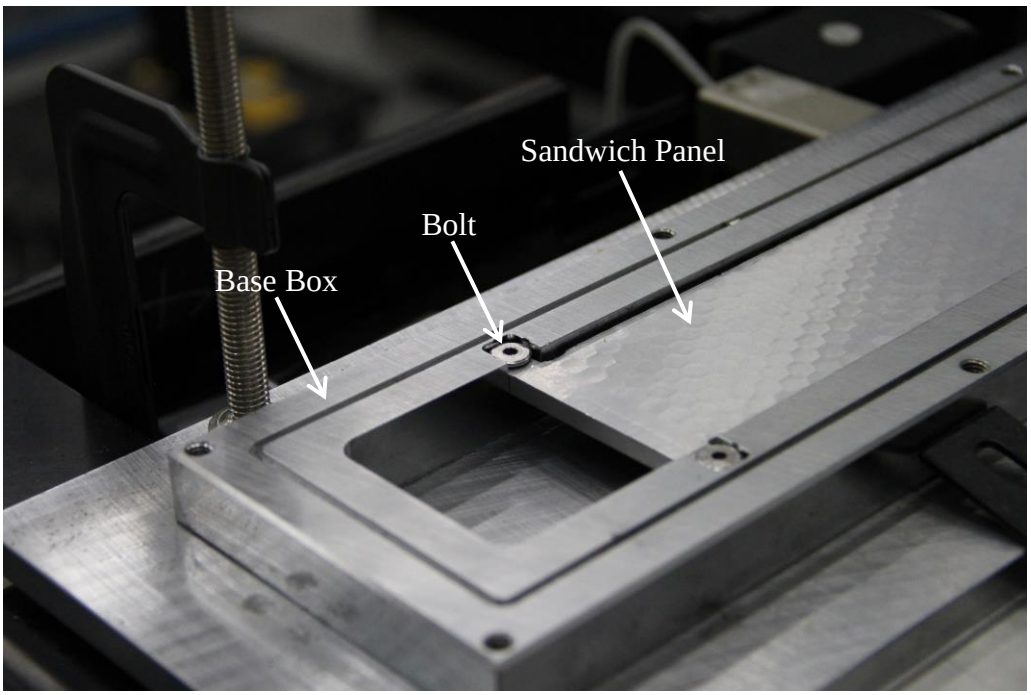

Figure 2.4 Specimen fixed in base box

Table 2.1 Geometrical and material properties of specimen.

Panel length_L (m)	0.4
Panel width_b (mm)	50
Face thickness_t_f (mm)	0.1
Core thickness_t_c (mm)	5.0
Face density_ρ_f (kg/m^3)	2.68×10^3
Core density_ρ_c (kg/m^3)	3.70×10^2
Face Young's modulus_E_f (Pa)	70.0×10^9
Core Young's modulus_E_c (Pa)	24.1×10^7
Core shear modulus_G_c (Pa)	34.5×10^7

Similar to typical modal testing, the specimen was excited by an electromagnetic exciter (A.R. Brown US-2) via a stinger, threaded through the hole drilled on the cover. The effect of stinger stiffness was eliminated by setting the stinger to be vertical and short as much as possible in order to transmit the excitation force only in the axial direction. With this attempt, the stinger stiffness in the axial direction was considered to be very high as compared to the panel bending stiffness. As presented in **Figure 2.5**, the stinger was mounted on the specimen by using a small piece of foil adhesive tape, which insignificantly affects the panel characteristics. The electromagnetic shaker was operated according to the sinusoid signal generated by the FFT analyzer. To identify the natural frequency in a frequency range of interest, the logarithmically swept-sine excitation (frequency range = 20-400 Hz and sweep rate = 0.5 octave/minute) was applied due to its reliability of the high signal-to-noise ratio. With the objective to determine the natural frequency of the first bending mode, the excitation point was determined in the center of the panel, which is its maximum displacement point. The vibratory measuring point was beside the excitation point to manifestly observe the panel displacement. The input excitation force was measured by a force transducer (PCB 352C23) installed on the tip of the exciter. The displacement response of the panel was measured by an optical displacement sensor (KEYENCE LK-3100). Both the input force and output response were transferred to the computer aided FFT analyzer (WCA AD-3661) to extract the modal parameters of the sandwich panel.

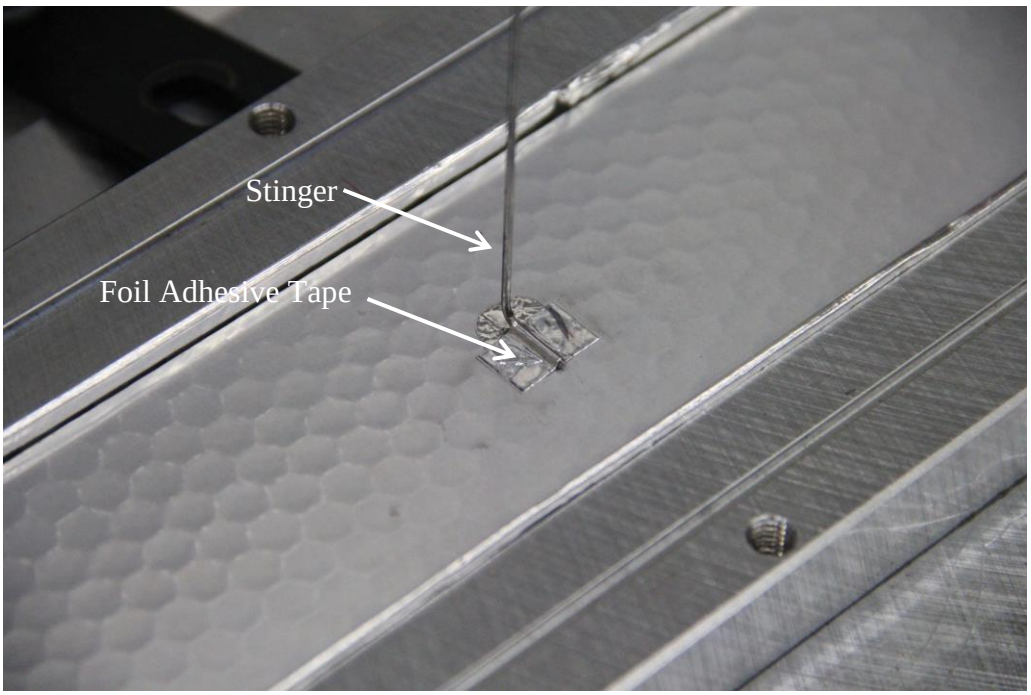

Figure 2.5 Stinger mounted on the specimen

2.3 Test conditions

To investigate the effect of air layer surrounding the sandwich panel, various conditions of air layer were determined as illustrated in **Figure 2.6**. From the front view of the air tight box enveloping the sandwich panel, the SIDE represents the horizontal distance between the panel end and the box's wall. The GAP is the vertical distance between the panel and the box's wall. To study the effect of SIDE, the variation of SIDE was determined for five cases, which are SIDE of 1, 3, 15, 25 and 50 mm. In this testing, the variation of SIDE is executed by using a spacer as shown in **Figure 2.7**. The condition of "without seals" and "with seals" represents the condition of 3- and 2-dimensional air flow, respectively. To evidently demonstrate the effect of SIDE, the factor of 3-dimensional air flow was limited in this study. As presented in **Figure 2.8**, the seal was placed along the longitudinal side of the

sandwich panel. Between the seal and sandwich panel, lubricant oil was applied to eliminate the friction that may occur. The effect of air layer thickness was also investigated by determining GAP of 3, 6, and 10 mm. The variation of GAP is performed by using a spacer as shown in **Figure 2.9**. At each SIDE condition, three different GAP thicknesses were performed thus the overall is 15 conditions. Each condition was performed 3 times to confirm the precision of the results.

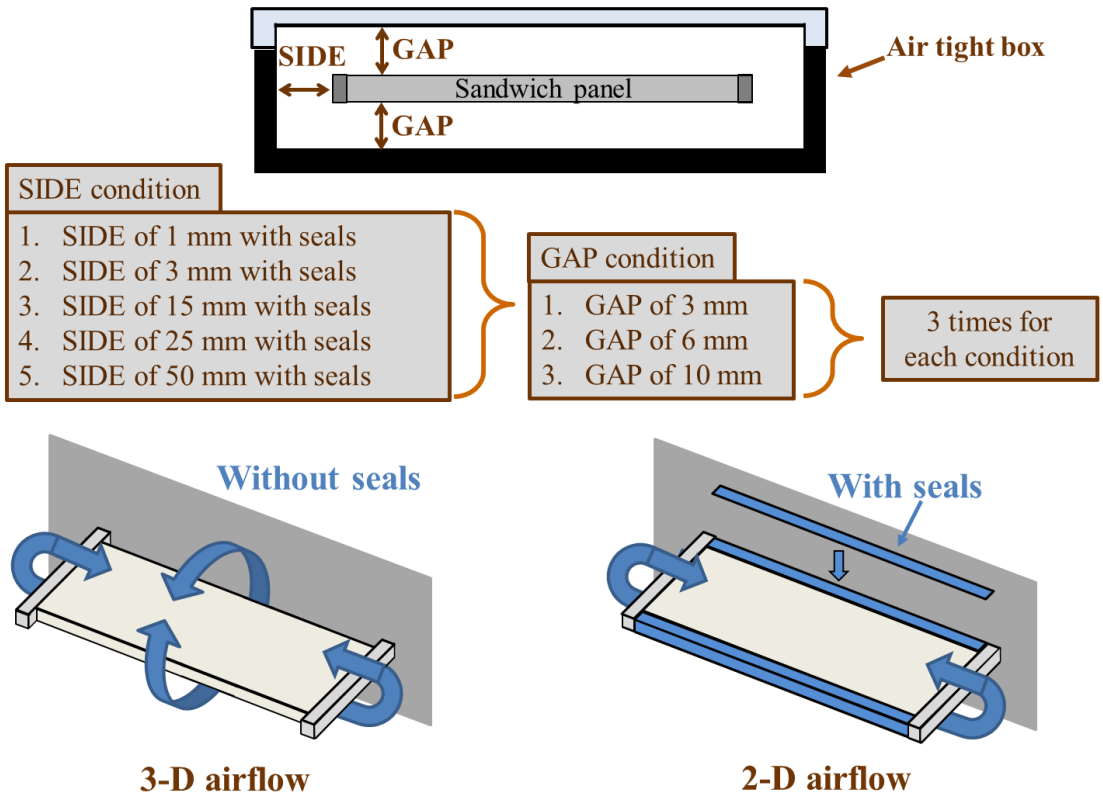

Figure 2.6 Air layers conditions

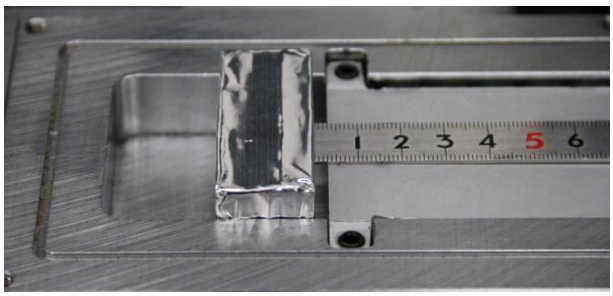

(a)

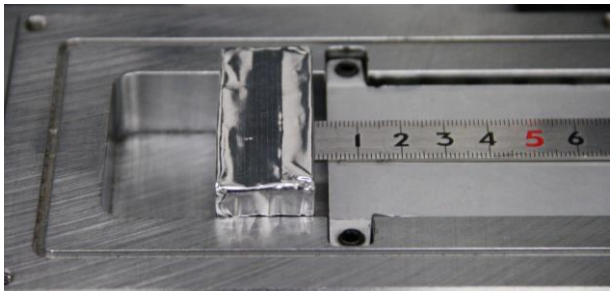

(b)

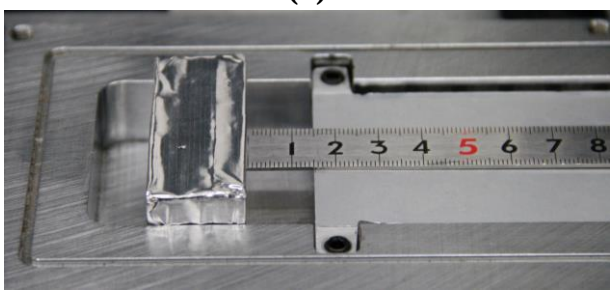

(c)

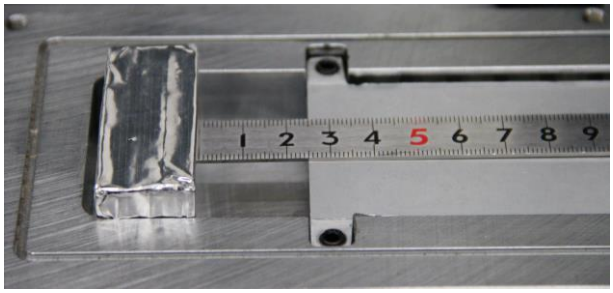

(d)

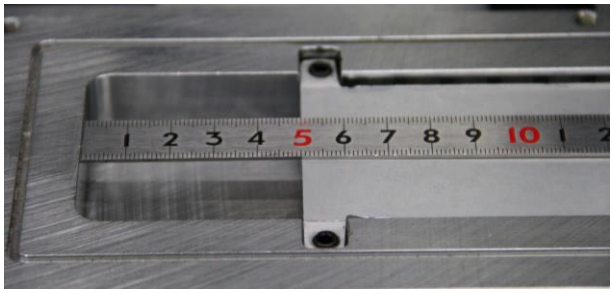

(e)

Figure 2.7 SIDE variation **(a)** SIDE of 1 mm **(b)** SIDE of 3 mm **(c)** SIDE of 15 mm **(d)** SIDE of 25 mm **(e)** SIDE of 50 mm

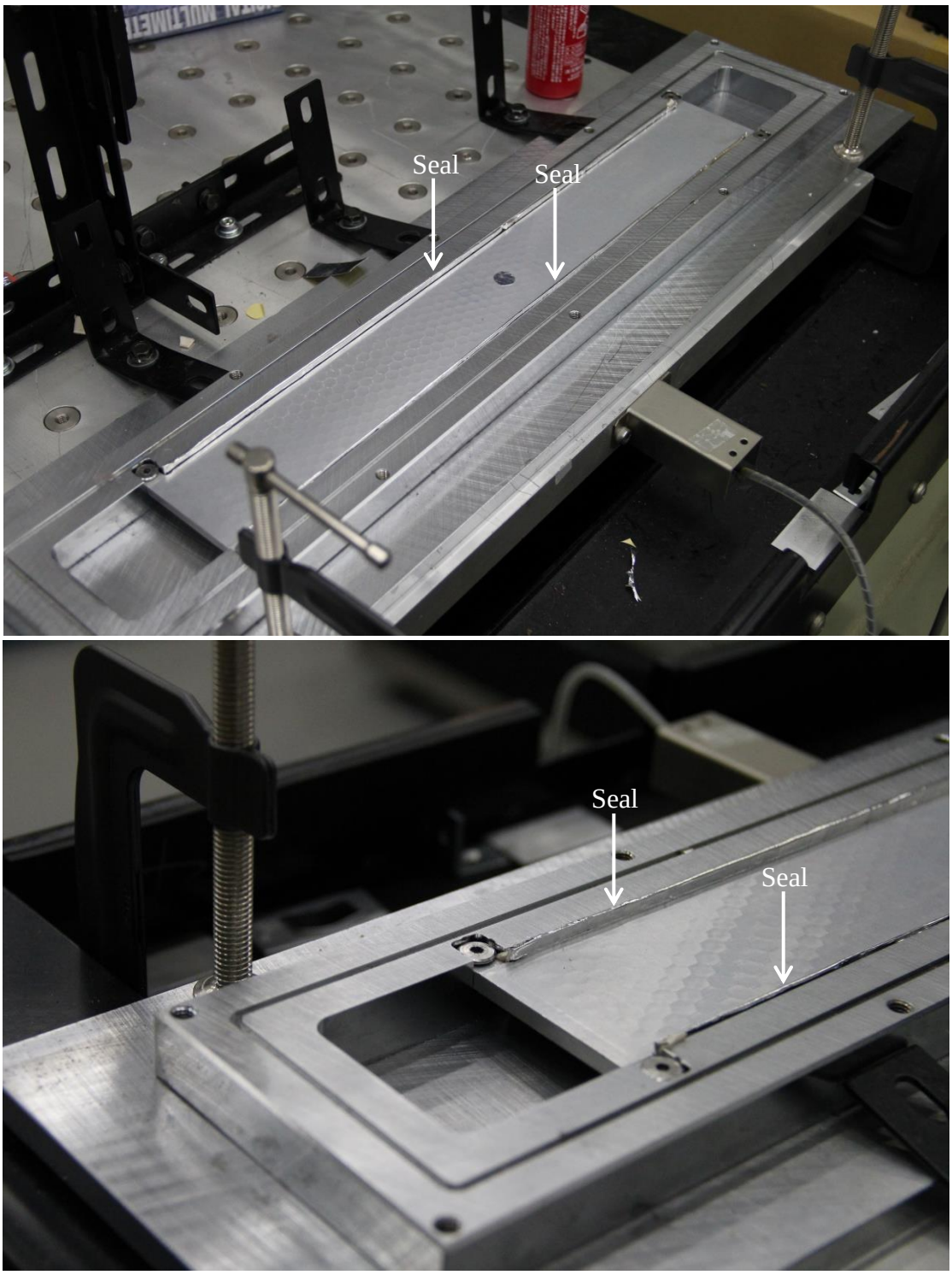

Figure 2.8 Seal installed along the longitudinal side of the sandwich panel

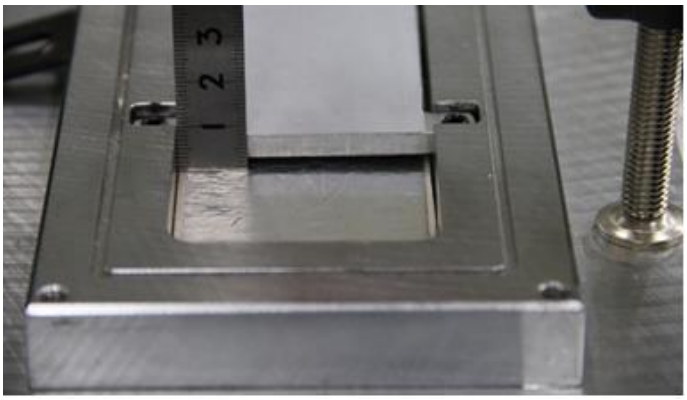

(a)

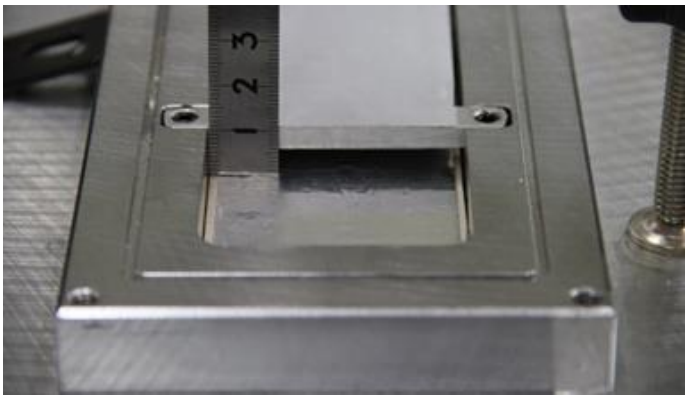

(b)

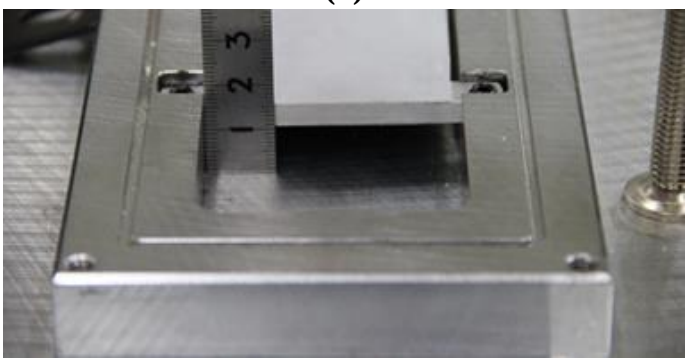

(c)

Figure 2.9 GAP variation **(a)** GAP of 3 mm **(b)** GAP of 6 mm **(c)** GAP of 10 mm

2.4 Results and discussion

The response amplitudes to the excited frequency are presented in **Figure 2.10**, **2.11**, **2.12**, **2.13**, and **2.14** for the SIDE of 1, 3, 15, 25, and 50 mm, respectively. The fundamental natural frequencies of the specimen determined from the response

amplitude, average frequency, and standard deviation are presented in **Table 2.2**, **2.3**, **2.4**, **2.5**, and **2.6** for the SIDE width of 1, 3, 15, 25, and 50 mm. The natural frequencies of each condition show good concurrence and the standard deviation is less than 0.5 Hz, which represents the verification of the obtained results.

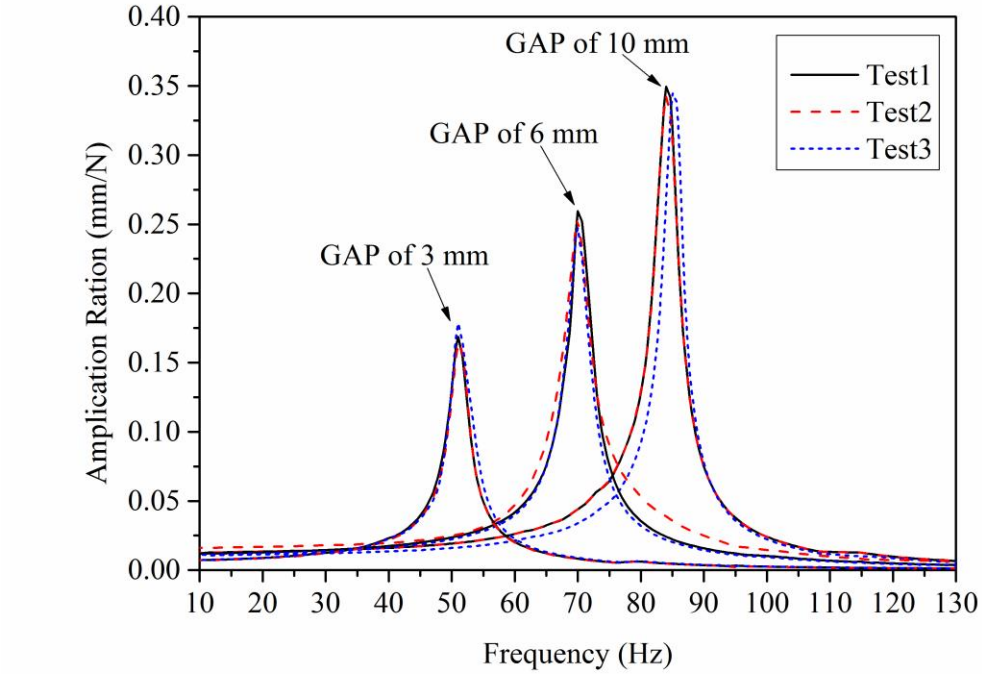

Figure 2.10 Frequency response: SIDE condition of 1 mm with seals

Table 2.2 Natural frequency: SIDE condition of 1 mm with seals.

GAP (mm)	Natural frequency (Hz)				Standard deviation (Hz)
	Test 1	Test 2	Test 3	Average	
3 mm	51.00	51.00	51.00	51.00	0.00
6 mm	70.25	70.00	70.00	70.08	0.14
10 mm	84.00	84.00	84.50	84.17	0.29

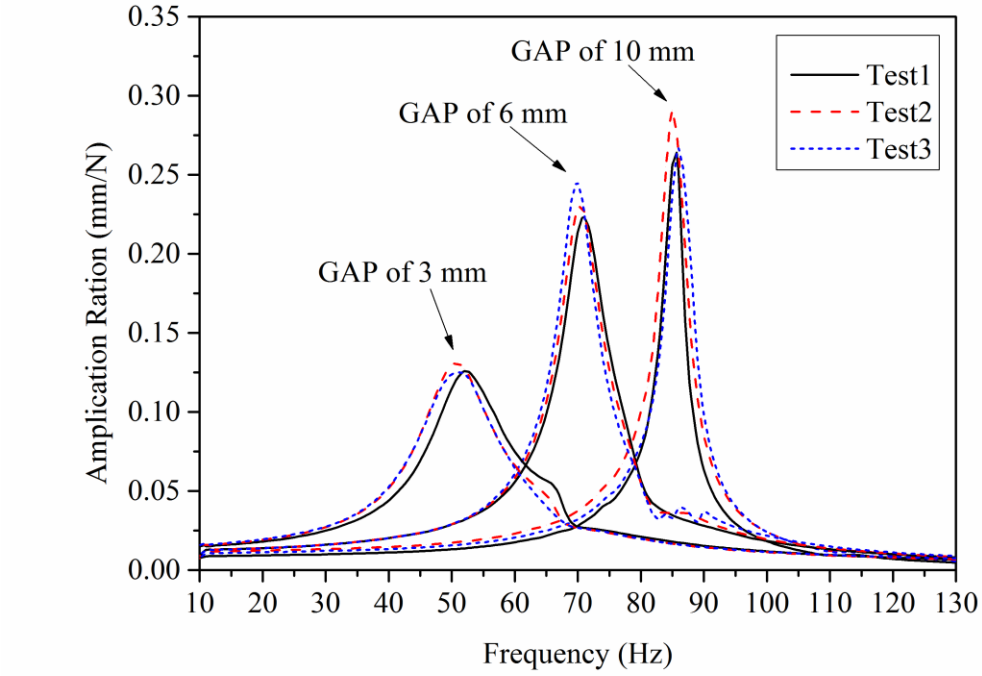

Figure 2.11 Frequency response: SIDE condition of 3 mm with seals

Table 2.3 Natural frequency: SIDE condition of 3 mm with seals.

GAP (mm)	Natural frequency (Hz)				Standard deviation (Hz)
	Test 1	Test 2	Test 3	Average	
3 mm	51.75	51.25	51.50	51.50	0.25
6 mm	71.00	70.75	70.50	70.75	0.25
10 mm	86.50	86.25	86.75	86.50	0.25

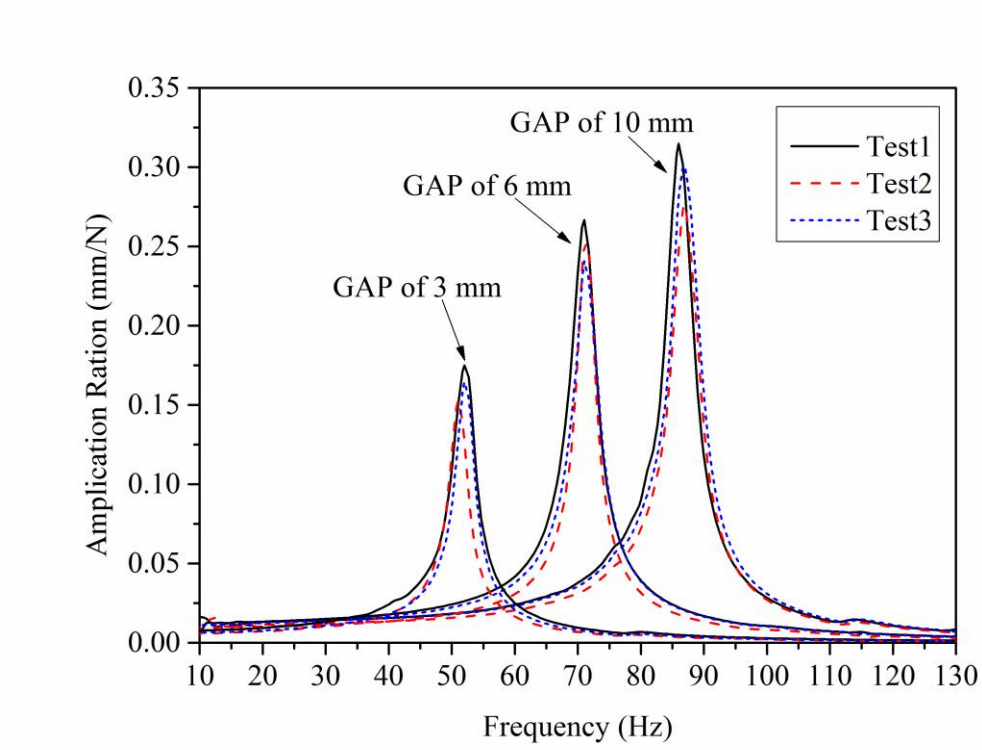

Figure 2.12 Frequency response: SIDE condition of 15 mm with seals

Table 2.4 Natural frequency: SIDE condition of 15 mm with seals.

GAP (mm)	Natural frequency (Hz)				Standard deviation (Hz)
	Test 1	Test 2	Test 3	Average	
3 mm	51.75	51.50	51.75	51.67	0.14
6 mm	70.50	70.75	70.75	70.67	0.14
10 mm	86.75	87.25	87.25	87.08	0.29

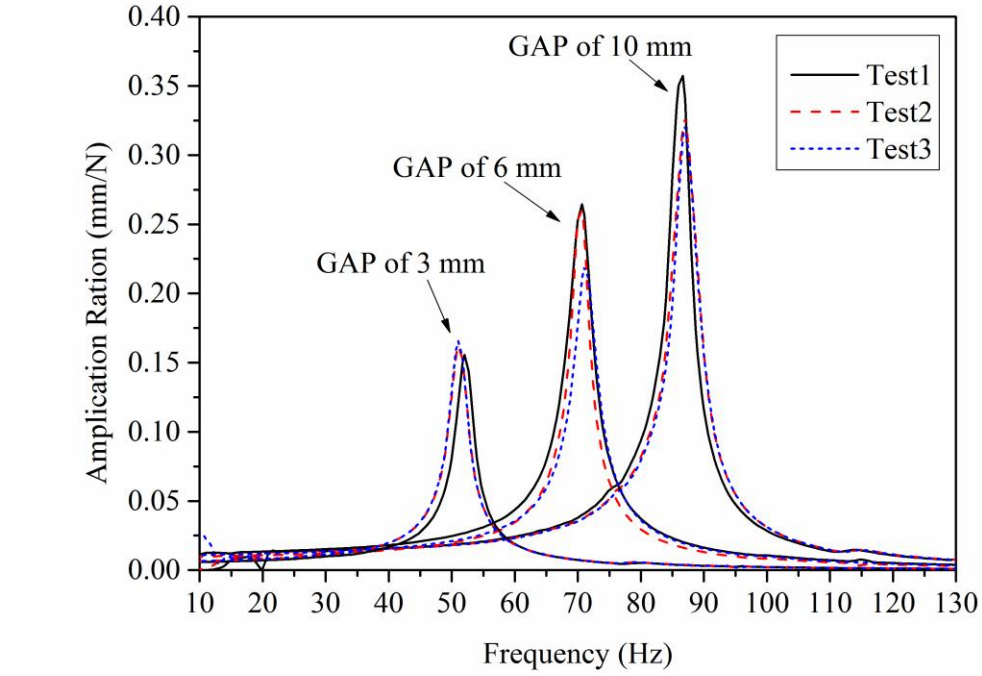

Figure 2.13 Frequency response: SIDE condition of 25 mm with seals

Table 2.5 Natural frequency: SIDE condition of 25 mm with seals.

GAP (mm)	Natural frequency (Hz)				Standard deviation (Hz)
	Test 1	Test 2	Test 3	Average	
3 mm	51.75	51.25	51.25	51.42	0.29
6 mm	70.50	70.50	71.00	70.67	0.29
10 mm	86.75	87.00	87.00	86.92	0.14

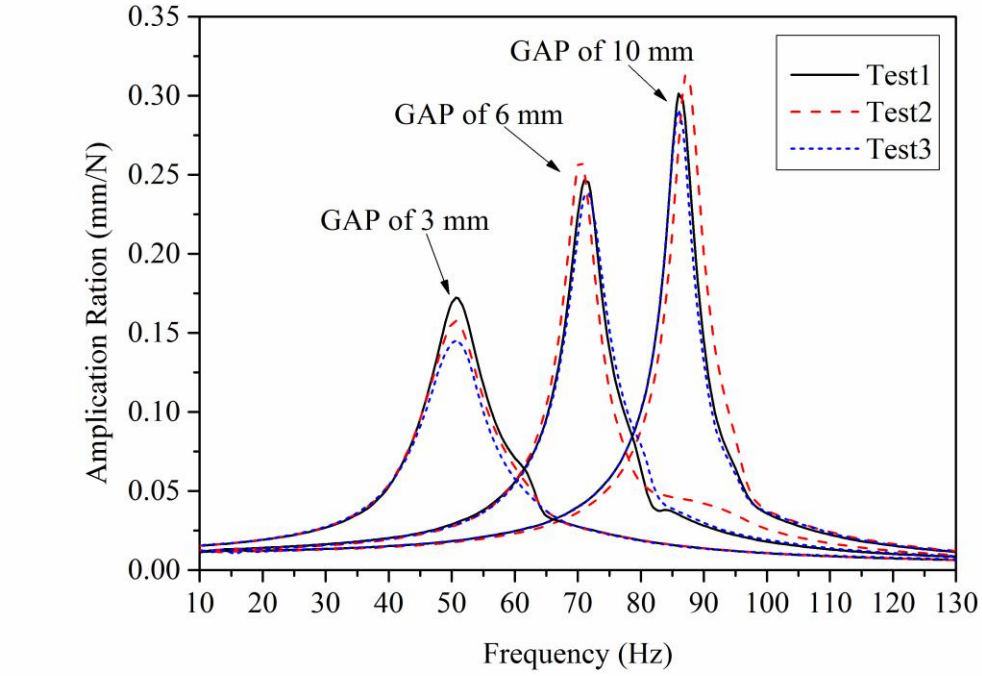

Figure 2.14 Frequency response: SIDE condition of 50 mm with seals

Table 2.6 Natural frequency: SIDE condition of 50 mm with seals.

GAP (mm)	Natural frequency (Hz)				Standard deviation (Hz)
	Test 1	Test 2	Test 3	Average	
3 mm	51.25	51.00	51.25	51.17	0.14
6 mm	70.75	70.50	71.00	70.75	0.25
10 mm	86.50	87.00	86.25	86.58	0.38

By considering the variation of GAP, the results reveal that the natural frequency decreases as the GAP becomes smaller. The reduction of natural frequency is understood that it is due to the added mass effect of ambient air, which is magnified when the air layer becomes thinner. To clarify this assumption, the average frequency of each condition is normalized by the natural frequency neglecting the influence of ambient air. For the sandwich panel used in this study, the fundamental natural frequency without air effect is 247.322 Hz. This frequency was estimated by using the analytical solution presented in equation (2.1). The derivation of this equation can be found in the Reference [39].

$$f^{o} = \frac{\pi}{2} \cdot \frac{2.27}{L^{2}} \cdot \sqrt{\frac{D_{B}}{\rho_{B}}} \tag{2.1}$$

Figure 2.15 presents the alteration of the normalized natural frequency as a function of GAP. At the GAP of 10 mm, the sandwich panel yield the lower natural frequency (by approximately 65%) compared to the natural frequency without air effect. Furthermore, the natural frequency significantly decreases of 73 and 79% while the GAP is decreased to be 6 and 3 mm, respectively. For the influence of SIDE, the results, illustrated in **Figure 2.16**, show that the variation of SIDE does not significantly affect the natural frequency when compared with the variation of GAP. However, when the SIDE is less than 3 mm, the SIDE effect is explicit in the case of GAP of 10 mm but slightly presents in the condition of GAP of 6 and 3 mm. The discussion of the GAP and SIDE effect are further provided in Chapter 4.

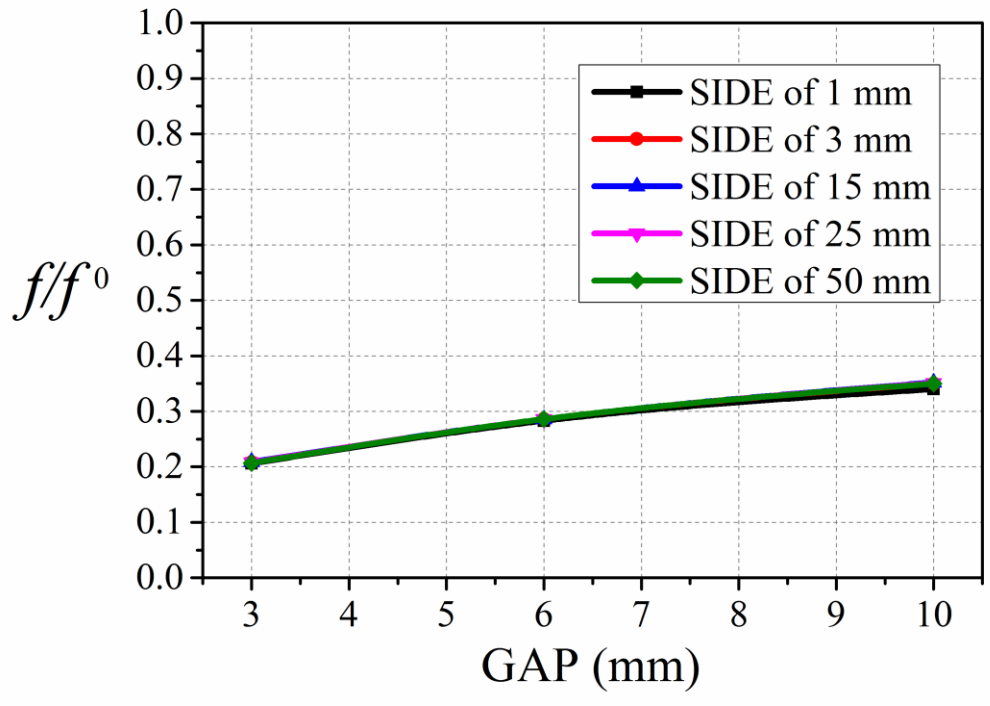

Figure 2.15 Normalized natural frequency as a function of GAP

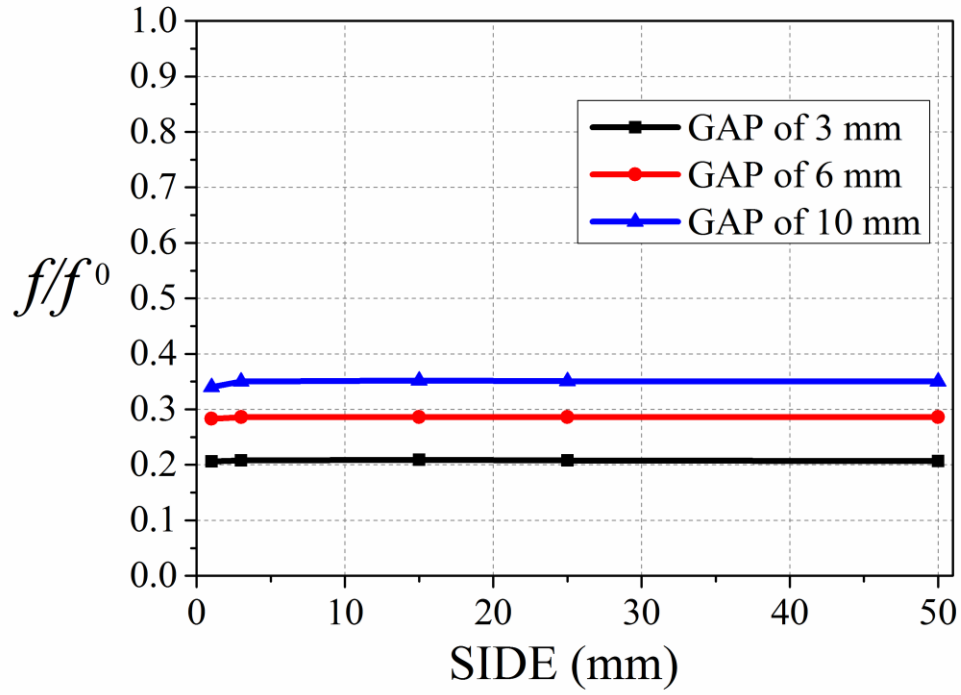

Figure 2.16 Normalized natural frequency as a function of SIDE

2.5 Conclusions

The modal experiments on the sandwich panel coupled with ambient air layer were performed in this chapter. Various conditions of air layer were determined to clearly describe the influence of ambient air layer. The obtained natural frequency of each condition shows good concurrence and the standard deviation is less than 0.5 Hz. Therefore, the precision of the obtained results was verified. The obtained results show that the ambient air layer disturbs the vibration of sandwich panel as an added mass effect resulting in the reduction of natural frequency. In addition, the effect becomes stronger as the GAP becomes thinner. For the condition of GAP of 10, 6, and 3 mm, the influence of air causes the reduction of natural frequency up to 65, 73, and 79%, respectively. However, the variation of SIDE insignificantly alters the natural frequency as compared with the variation of GAP.

Chapter 3
Finite element modelling

3.1 Basic configuration

To verify the experimental results and to conduct parametric studies, the finite element model was formulated on the basis of fluid-structure interaction analysis. The model configuration is a vibrating flexible sandwich panel fully coupled with ambient air surrounded by rigid walls. As sketched in **Figure 3.1**, while the sandwich panel vibrates, the air flow interacts with the motion of the panel. Here, Ω_1, Ω_2, G, and W denote the panel domain, air domain, coupled interface between Ω_1 and Ω_2, and rigid wall boundary, respectively. The flexible panel is vertically placed along the X-Y plane and is considered to possess identical properties throughout the plane. Thus, the 2-dimensional model is adopted to obtain accurate results in a reasonable calculation time. The thickness of air layers can be varied from thin to thick and the thickness of sandwich panel is taken into account. Although, in this study, the analysis of 2-dimensional problem was applied to demonstrate the potential capability of the model, the formulation can be applied for 3-dimensional problem for further study.

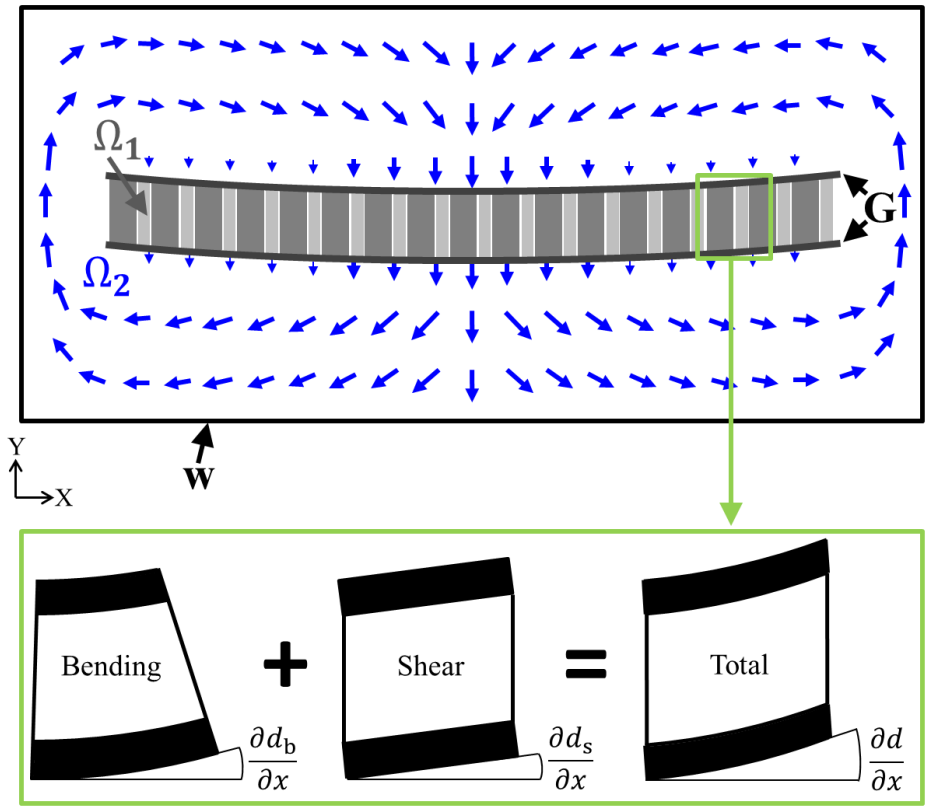

Figure 3.1 Sketch of a vibrating sandwich panel coupled with ambient air

For the panel domain (Ω_1), the flexural vibration of the sandwich panel was described by the governing equation formulated based on the sandwich theory and the following assumption: The sandwich panel is a kind of a lightweight thick core sandwiched between two thin face laminates. The face laminates were considered to be identical in geometrical and physical properties. The core was assumed to be very weak in X-direction but in Y-direction to be so stiff that the lateral deflection of two laminates are identic in the frequency range of interest. The lateral deflection of the sandwich panel is composed of the pure bending and the core shear deformation as illustrated in **Figure 3.1**. The rotary inertia of the sandwich panel was neglected. The governing equation for the sandwich panel is derived as follows:

$$\rho_B\left(G_c b t_c \frac{\partial^2 d}{\partial t^2} - (D_B + 2D_f)\frac{\partial^4 d}{\partial x^2 \partial t^2}\right) + D_B\left(G_c b t_c \frac{\partial^4 d}{\partial x^4} - 2D_f \frac{\partial^6 d}{\partial x^6}\right) + (D_B + 2D_f)\frac{\partial^2 q}{\partial x^2} - G_c b t_c q = 0 \tag{3.1}$$

$$\rho_B = b\left(2\rho_f t_f + \rho_c t_c\right) \tag{3.2}$$

$$D_B = b\left(\frac{1}{6}E_f t_f^3 + \frac{1}{2}E_f t_f (t_f + t_c)^2 + \frac{1}{12}E_c t_c^3\right),\ D_f = \frac{1}{12}bE_f t_f^3 \tag{3.3}$$

Here, ρ_B, D_B, b, d, q, and t denote the sandwich panel mass per unit length, flexural rigidity, width, lateral displacement, lateral force per unit length, and time. D_f is the flexural rigidity of single face laminate. ρ_c, t_c, E_c, and G_c are the core density, thickness, Young's modulus, and effective shear stiffness. D_f, ρ_f, t_f, and E_f are the face sheet flexural rigidity, density, thickness, and Young's modulus. The derivation of equation (3.1) can be found in References [23,24,39]

For the motion of the air domain (Ω_1), the assumption of viscous incompressible flow was employed because the viscous effect is important for thin air layer condition and the compressibility is neglected due to the slow flow application. However, the calculation of viscous incompressible equation requires great amount of computational resources [40-42]. To solve this problem, the penalty function method was applied for the formulation of the Navier-Stokes equations system, used for governing the dynamic behaviour of the air. The Navier-Stokes momentum equation derived for this study is present in equation (3.4) in which the convective acceleration term is cancelled since the spatial effect is so small due to the excellent stiffness characteristic of sandwich structure and the assumption that the vibration amplitude of sandwich panel is very small as compared with the air layer thickness. Moreover, the

verification for neglecting the convective acceleration term is given in Appendix E.

$$\rho_A \frac{\partial \boldsymbol{u}}{\partial t} + \nabla p - \mu \nabla^2 \boldsymbol{u} = 0 \tag{3.4}$$

The continuity equation with the modification by penalty function formulation is

$$\nabla \cdot \boldsymbol{u} = -\varepsilon_p p \tag{3.5}$$

and the constitutive equation for the stoke flow is as follow:

$$\sigma_{ij} = -p\delta_{ij} + \mu\left(\frac{\partial u_i}{\partial x_j} + \frac{\partial u_j}{\partial x_i}\right) \tag{3.6}$$

Here, ρ_A, $\boldsymbol{u}$, p, μ, and ε_p denote the air density, velocity vector, pressure, viscosity coefficient, and penalty parameter, respectively. σ_{ij} and δ_{ij} are the stress tensor of the air and the Kronecker delta.

The coupling interaction between the sandwich panel and air region was determined by considering the continuity of stress and velocity vector through the air-panel interface (G). The relation between air and panel stress vector is hold as follows:

$$\boldsymbol{\sigma}_B \cdot \boldsymbol{n} = \boldsymbol{\sigma}_A \cdot \boldsymbol{n} \tag{3.7}$$

Here, $\boldsymbol{\sigma}_B$ and $\boldsymbol{\sigma}_A$ denote the stress tensor of the panel and air, respectively and $\boldsymbol{n}$ is the normal unit vector on the coupled boundary surface, which is expressed as

$$\boldsymbol{n} = \boldsymbol{n}_A = -\boldsymbol{n}_B \tag{3.8}$$

Here, $\boldsymbol{n}_A$ denotes the normal unit vector outward from the air region and $\boldsymbol{n}_B$ is the normal unit vector outward from the panel region.

The continuity of velocity vector across the interface is concluded as below:

$$u = 0$$

$$v = \frac{\partial d}{\partial t} \tag{3.9}$$

3.2 Formulation of finite element and eigenvalue equations

The governing equations discussed above were written in the weak-form representations and then were discretized into a set of discrete matrix equations based on the methods of Galerkin weighted residual and finite element. To formulate the governing equations in the variational integrals, i.e., the weak-form representations, an appropriated weighting function is required for each equation.

Based on the Galerkin formulation, the shape function for the related element was used as the weighting function for each governing equation. The shape function is the function used to interpolate the physical solution of every node within a finite element. $\lfloor N_d \rfloor$, $\lfloor N_u \rfloor$, and $\lfloor N_p \rfloor$ symbolize the shape function matrix for the panel lateral displacement, the air velocity, and the air pressure, which can be concluded as follows:

$$d = \lfloor N_d \rfloor \{d^e\}$$

$$\boldsymbol{u} = \lfloor N_u \rfloor \{\boldsymbol{u}^e\}$$

$$p = \lfloor N_p \rfloor \{p^e\} \tag{3.10}$$

Here, $\{d^e\}$, $\{\boldsymbol{u}^e\}$, and $\{p^e\}$ represent the matrix of the nodal panel lateral displacement, the nodal air velocity vector, and the nodal air pressure for each finite element. The superscript 'e' is the indicator referred to the order of each finite element.

For the governing equation of the sandwich panel (3.1), the shape function for the panel displacement was applied as a weighting function. The derivation was done in the following succession as shown in equation (3.11). The panel lateral displacement d was determined to be expressed as a function proportional to $e^{\lambda t}$, in which λ is the complex conjugate quantity associated with the natural frequency of the

system. The discretized equation of the derived weak-form representation has been defined lastly in equation (3.11).

$$\begin{aligned}
&\int_{\Omega_1^e}\lfloor N_d \rfloor^T \left(\begin{array}{l} \rho_B\left(G_c b t_c \frac{\partial^2 d}{\partial t^2} - (D_B + 2D_f)\frac{\partial^4 d}{\partial x^2 \partial t^2} \right) \\ + D_B\left(G_c b t_c \frac{\partial^4 d}{\partial x^4} - 2D_f \frac{\partial^6 d}{\partial x^6} \right) + (D_B + 2D_f)\frac{\partial^2\left(\nabla \cdot \sigma_{B_{ij}}\right)}{\partial x^2} - G_c b t_c \left(\nabla \cdot \sigma_{B_{ij}}\right) \end{array} \right) d\Omega_1^e \\
&= \lambda^2 \rho_B \left(G_c b t_c \int_{\Omega_1^e} \lfloor N_d \rfloor^T \cdot \lfloor N_d \rfloor d\Omega_1^e - (D_B + 2D_f)\int_{\Omega_1^e} \left\lfloor \frac{\partial N_d}{\partial x} \right\rfloor^T \cdot \left\lfloor \frac{\partial N_d}{\partial x} \right\rfloor d\Omega_1^e \right) \cdot \{d^e\} \\
&\quad + D_B \left(G_c b t_c \int_{\Omega_1^e} \left\lfloor \frac{\partial^2 N_d}{\partial x^2} \right\rfloor^T \cdot \left\lfloor \frac{\partial^2 N_d}{\partial x^2} \right\rfloor d\Omega_1^e - 2D_f \int_{\Omega_1^e} \left\lfloor \frac{\partial^3 N_d}{\partial x^3} \right\rfloor^T \cdot \left\lfloor \frac{\partial^3 N_d}{\partial x^3} \right\rfloor d\Omega_1^e \right) \cdot \{d^e\} \\
&\quad - (D_B + 2D_f) \left(\frac{1}{\varepsilon_p} \int_{G^e} \left\lfloor \frac{\partial^2 N_d}{\partial x^2} \right\rfloor^T \cdot \left\lfloor \frac{\partial N_u}{\partial x} \quad \frac{\partial N_u}{\partial y} \right\rfloor dG^e - 2\mu \int_{G^e} \left\lfloor \frac{\partial^2 N_d}{\partial x^2} \right\rfloor^T \cdot \left\lfloor 0 \quad \frac{\partial N_u}{\partial y} \right\rfloor dG^e \right) \cdot \{\boldsymbol{u}^e\} \\
&\quad + G_c b t_c \left(\frac{1}{\varepsilon_p} \int_{G^e} \lfloor N_d \rfloor^T \cdot \left\lfloor \frac{\partial N_u}{\partial x} \quad \frac{\partial N_u}{\partial y} \right\rfloor dG^e - 2\mu \int_{G^e} \lfloor N_d \rfloor^T \cdot \left\lfloor 0 \quad \frac{\partial N_u}{\partial y} \right\rfloor dG^e \right) \cdot \{\boldsymbol{u}^e\} \\
&= \lambda^2 \left[M_B^e\right] \cdot \{d^e\} + \left[K_B^e\right] \cdot \{d^e\} + \left[G_B^e\right] \cdot \{\boldsymbol{u}^e\}
\end{aligned} \tag{3.11}$$

Here, $\left[M_B^e\right]$ is the element mass matrix of the sandwich panel:

$$\left[M_B^e\right] = \rho_B \left(G_c b t_c \int_{\Omega_1^e} \lfloor N_d \rfloor^T \cdot \lfloor N_d \rfloor d\Omega_1^e - (D_B + 2D_f)\int_{\Omega_1^e} \left\lfloor \frac{\partial N_d}{\partial x} \right\rfloor^T \cdot \left\lfloor \frac{\partial N_d}{\partial x} \right\rfloor d\Omega_1^e \right) \tag{3.12}$$

$\left[K_B^e\right]$ is the element stiffness matrix of the sandwich panel:

$$\left[K_B^e\right] = D_B \left(G_c b t_c \int_{\Omega_1^e} \left\lfloor \frac{\partial^2 N_d}{\partial x^2} \right\rfloor^T \cdot \left\lfloor \frac{\partial^2 N_d}{\partial x^2} \right\rfloor d\Omega_1^e - 2D_f \int_{\Omega_1^e} \left\lfloor \frac{\partial^3 N_d}{\partial x^3} \right\rfloor^T \cdot \left\lfloor \frac{\partial^3 N_d}{\partial x^3} \right\rfloor d\Omega_1^e \right) \tag{3.13}$$

$\left[G_B^e\right]$ is the element coupling interface matrix of the sandwich panel:

$$\begin{aligned}
\left[G_B^e\right] &= G_c b t_c \left(\frac{1}{\varepsilon_p} \int_{G^e} \lfloor N_d \rfloor^T \cdot \left\lfloor \frac{\partial N_u}{\partial x} \quad \frac{\partial N_u}{\partial y} \right\rfloor dG^e - 2\mu \int_{G^e} \lfloor N_d \rfloor^T \cdot \left\lfloor 0 \quad \frac{\partial N_u}{\partial y} \right\rfloor dG^e \right) \\
&\quad - (D_B + 2D_f) \left(\frac{1}{\varepsilon_p} \int_{G^e} \left\lfloor \frac{\partial^2 N_d}{\partial x^2} \right\rfloor^T \cdot \left\lfloor \frac{\partial N_u}{\partial x} \quad \frac{\partial N_u}{\partial y} \right\rfloor dG^e - 2\mu \int_{G^e} \left\lfloor \frac{\partial^2 N_d}{\partial x^2} \right\rfloor^T \cdot \left\lfloor 0 \quad \frac{\partial N_u}{\partial y} \right\rfloor dG^e \right)
\end{aligned} \tag{3.14}$$

In case of the governing equation of the air (3.4), the shape function for the air velocity was used as a weighting function. The derived weak-form representations and the discretized equations for the air governing equation are presented in equation (3.15). The air velocity vector $\boldsymbol{u}$ was also defined as a function proportional to $e^{\lambda t}$. For the continuity equation (3.5), the shape function for the air pressure was selected as a weighting function. The weak-form representations and the discretized equations for the continuity equation were derived as illustrated in equation (3.16).

$$
\begin{aligned}
&\int_{\Omega_2^e} \lfloor N_u \rfloor^T \left(\rho_A \frac{\partial \boldsymbol{u}}{\partial t} + \nabla p - \mu \nabla^2 \boldsymbol{u} \right) d\Omega_2^e \\
&= \lambda \rho_A \int_{\Omega_2^e} \lfloor N_u \rfloor^T \cdot \boldsymbol{u} d\Omega_A^e - \int_{\Omega_A^e} p \nabla \cdot \lfloor N_u \rfloor^T d\Omega_2^e \\
&\quad + \mu \int_{\Omega_2^e} \nabla \lfloor N_u \rfloor^T \cdot \left(u_{i,j} + u_{j,i} \right) d\Omega_2^e \\
&\quad - \int_{S_A^e = G^e} \left(\lfloor N_u \rfloor_n^T \cdot \sigma_{A_n} + \lfloor N_u \rfloor_\tau^T \cdot \sigma_{A_\tau} \right) dS_A^e \\
&= \lambda \rho_A \int_{\Omega_2^e} \lfloor N_u \rfloor^T \cdot \lfloor N_u \rfloor d\Omega_2^e \cdot \{\boldsymbol{u}^e\} - \int_{\Omega_2^e} \lfloor N_p \rfloor^T \cdot \begin{bmatrix} \frac{\partial N_u}{\partial x} & \frac{\partial N_u}{\partial y} \end{bmatrix} d\Omega_2^e \cdot \{p^e\} \\
&\quad + \mu \int_{\Omega_2^e} \nabla \lfloor N_u \rfloor^T \cdot \left(\lfloor N_u \rfloor_{i,j} + \lfloor N_u \rfloor_{j,i} \right) d\Omega_2^e \cdot \{\boldsymbol{u}^e\} \\
&\quad - \frac{1}{\varepsilon_p} \int_{G^e} \lfloor 0 \quad N_u \rfloor^T \cdot \begin{bmatrix} \frac{\partial N_u}{\partial x} & \frac{\partial N_u}{\partial y} \end{bmatrix} dG^e \cdot \{\boldsymbol{u}^e\} \\
&\quad - 2\mu \int_{G^e} \lfloor 0 \quad N_u \rfloor^T \cdot \begin{bmatrix} 0 & \frac{\partial N_u}{\partial y} \end{bmatrix} dG^e \cdot \{\boldsymbol{u}^e\} \\
&\quad - \mu \int_{G^e} \lfloor N_u \quad 0 \rfloor^T \cdot \begin{bmatrix} \frac{\partial N_u}{\partial y} & \frac{\partial N_u}{\partial x} \end{bmatrix} dG^e \cdot \{\boldsymbol{u}^e\} \\
&= \lambda \left[M_A^e \right] \cdot \{\boldsymbol{u}^e\} - \varepsilon_p \left[H^e \right]^T \cdot \{p^e\} + \left[K_A^e \right] \cdot \{\boldsymbol{u}^e\} - \left[G_A^e \right] \cdot \{\boldsymbol{u}^e\}
\end{aligned}
\tag{3.15}
$$

$$
\begin{aligned}
&\int_{\Omega_2^e} \lfloor N_p \rfloor^T \left(p + \frac{1}{\varepsilon_p} (\nabla \cdot \boldsymbol{u}) \right) d\Omega_2^e \\
&= \int_{\Omega_2^e} \lfloor N_p \rfloor^T \cdot \lfloor N_p \rfloor d\Omega_2^e \cdot \{p^e\} + \frac{1}{\varepsilon_p} \int_{\Omega_2^e} \lfloor N_p \rfloor^T \cdot \begin{bmatrix} \frac{\partial N_u}{\partial x} & \frac{\partial N_u}{\partial y} \end{bmatrix} d\Omega_2^e \cdot \{\boldsymbol{u}^e\} \\
&= \left[P^e \right] \cdot \{p^e\} + \left[H^e \right] \cdot \{\boldsymbol{u}^e\}
\end{aligned}
\tag{3.16}
$$

Here, $\left[M_A^e\right]$ is the element mass matrix of the air:

$$\left[M_A^e\right]=\rho_A\int_{\Omega_2^e}\left\lfloor N_u\right\rfloor^T\cdot\left\lfloor N_u\right\rfloor d\Omega_2^e \tag{3.17}$$

$\left[K_A^e\right]$ is the element stiffness matrix of the air:

$$\left[K_A^e\right]=\mu\int_{\Omega_2^e}\nabla\left\lfloor N_u\right\rfloor^T\cdot\left(\left\lfloor N_u\right\rfloor_{i,j}+\left\lfloor N_u\right\rfloor_{j,i}\right)d\Omega_2^e \tag{3.18}$$

$\left[G_A^e\right]$ is the element coupling interface matrix of the air:

$$\begin{aligned}\left[G_A^e\right]=&\frac{1}{\varepsilon_p}\int_{G^e}\left\lfloor 0 \quad N_u\right\rfloor^T\cdot\begin{bmatrix}\frac{\partial N_u}{\partial x} & \frac{\partial N_u}{\partial y}\end{bmatrix}dG^e\\&+2\mu\int_{G^e}\left\lfloor 0 \quad N_u\right\rfloor^T\cdot\begin{bmatrix}0 & \frac{\partial N_u}{\partial y}\end{bmatrix}dG^e\\&+\mu\int_{G^e}\left\lfloor N_u \quad 0\right\rfloor^T\cdot\begin{bmatrix}\frac{\partial N_u}{\partial y} & \frac{\partial N_u}{\partial x}\end{bmatrix}dG^e\end{aligned} \tag{3.19}$$

$\left[P^e\right]$ is the element pressure matrix of the air:

$$\left[P^e\right]=\int_{\Omega_2^e}\left\lfloor N_p\right\rfloor^T\cdot\left\lfloor N_p\right\rfloor d\Omega_2^e \tag{3.20}$$

$\left[H^e\right]$ is the element penalty matrix of the air:

$$\left[H^e\right]=\frac{1}{\varepsilon_p}\int_{\Omega_2^e}\left\lfloor N_p\right\rfloor^T\cdot\begin{bmatrix}\frac{\partial N_u}{\partial x} & \frac{\partial N_u}{\partial y}\end{bmatrix}d\Omega_2^e \tag{3.21}$$

After the discrete matrix equations of the panel and air were derived, each of the discrete matrix equation was then derived to be coupled each other to describe the dynamic interaction between the sandwich panel and air. Due to the explanation of the Galerkin method, the summation of all finite elements is equal to zero thus the discrete matrix equations can be determined as in equation (3.22)-(3.24).

$$\begin{aligned}&\sum_e\left(\lambda^2\left[M_B^e\right]\cdot\left\{d^e\right\}+\left[K_B^e\right]\cdot\left\{d^e\right\}+\left[G_B^e\right]\cdot\left\{\boldsymbol{u}^e\right\}\right)\\&=\lambda^2\left[M_B\right]\cdot\left\{d\right\}+\left[K_B\right]\cdot\left\{d\right\}+\left[G_B\right]\cdot\left\{\boldsymbol{u}\right\}=0\end{aligned} \tag{3.22}$$

$$\sum_e \left(\lambda\left[M_A^e\right]\cdot\left\{\boldsymbol{u}^e\right\}-\varepsilon_p\left[H^e\right]^T\cdot\left\{p^e\right\}+\left[K_A^e\right]\cdot\left\{\boldsymbol{u}^e\right\}-\left[G_A^e\right]\cdot\left\{\boldsymbol{u}^e\right\}\right)$$
$$=\lambda\left[M_A\right]\cdot\left\{\boldsymbol{u}\right\}-\varepsilon_p\left[H\right]^T\cdot\left\{p\right\}+\left[K_A\right]\cdot\left\{\boldsymbol{u}\right\}-\left[G_A\right]\cdot\left\{\boldsymbol{u}\right\}=0 \quad (3.23)$$

$$\sum_e \left(\left[P^e\right]\cdot\left\{p^e\right\}+\left[H^e\right]\cdot\left\{\boldsymbol{u}^e\right\}\right)$$
$$=\left[P\right]\cdot\left\{p\right\}+\left[H\right]\cdot\left\{\boldsymbol{u}\right\}=0 \quad (3.24)$$

Based on the monolithic approach and eigenvalue problem, the coupled discrete matrix equation derived according to the continuity through the interface is presented in equation (3.25), in which $[M]$, $[C]$, $[K]$, and $\{\boldsymbol{w}\}$ are the system mass matrix, damping matrix, stiffness matrix, and velocity vector matrix. The combination of each matrix is presented in equation (3.26)-(3.29). The variable w was determined to combine the matrix of nodal panel lateral displacement and that of nodal air velocity vector into one matrix. The coupled discrete matrix equation was derived to be mathematically identical to the general eigenvalue problem. The solution of this equation is eigenvalues and eigenvectors, which represent the natural frequencies of the sandwich panel and the corresponding air velocity vectors and time derivative of panel displacement. The nodal air pressure was calculated from the nodal air velocity vector using equation (3.30).

$$\left(\lambda^2\left[M\right]+\lambda\left[C\right]+\left[K\right]\right)\cdot\left\{\boldsymbol{w}\right\}=0 \quad (3.25)$$

$$\left[M\right]=\left[M_A\right]+\left[M_B\right] \quad (3.26)$$

$$\left[C\right]=\left[K_A\right]+\varepsilon_p\left[H\right]^T\left[P\right]^{-1}\left[H\right]+\left[G_B\right]-\left[G_A\right] \quad (3.27)$$

$$\left[K\right]=\left[K_B\right] \quad (3.28)$$

$$\boldsymbol{w}=\begin{cases}\boldsymbol{u} & \text{in air}\\ u=\lambda d & \text{on interface}\\ \lambda d & \text{in beam}\end{cases} \quad (3.29)$$

$$\{p\} = -[P]^{-1} \cdot [H] \cdot \{\boldsymbol{u}\} \tag{3.30}$$

3.3 Implementation of finite element and eigenvalue equations

In this study, the finite element formulation presented above was implemented in an in-house program operating on a Fortran 90 environment. Gauss-Legendre quadrature was employed for performing the numerical integration. The coupled discrete matrix equation (3.25) was expressed as presented in Equation (3.31) and was solved by using a double-QR iteration procedure on the basis of the stabilized elementary similarity transformations to an upper Hessenberg Form (UHF) [43-46].

$$\begin{bmatrix} [0] & [1] \\ -[M]^{-1}[K] & -[M]^{-1}[C] \end{bmatrix} \begin{Bmatrix} \boldsymbol{w} \\ \lambda \boldsymbol{w} \end{Bmatrix} = \lambda \begin{Bmatrix} \boldsymbol{w} \\ \lambda \boldsymbol{w} \end{Bmatrix} \tag{3.31}$$

The types of elements for discretizing the air and the panel domain were selected based on the following discussion. For the motion of air domain governed by the Navier-Stokes equations, only first order partial derivatives exist on the variational formulation. In this case, only linear functions are adequate for interpolation of the air motion. However, the formulation of this study is also based on the penalty function method. The effective set of finite elements should be selected for the air domain. The effective sets of finite elements and the corresponding integration scheme recommended for the penalty formulation were introduced in [41], which suggested that the most effective type of elements is the Lagrange isoparametric elements but any triangular elements and serendipity quadrilateral elements are not recommended due to their unsatisfied results. Besides, when using the penalty function method, it is necessary to calculate the inverse of air pressure matrix $[P]$ as formulated $[P]^{-1}$ in

Equation (3.27). In this case, if the pressure approximation, which is discontinuous across the element boundaries is employed the bandwidth of $[P]$ is the same with the bandwidth of $[P]^{-1}$. On the contrary, the utilization of pressure approximation continuous between adjacent elements leads to the increase of the bandwidth of $[P]^{-1}$ and thus the error in calculation. The explained aspect has been investigated in Appendix D. According to the above explanation and simplicity for implementation to the in-house analysis codes, the combination of quadrilateral elements, called Crouzeix-Raviart (Q_2-P_{-1}) element was selected for the interpolation of the air velocity and pressure. The designation of Q_2 indicates a quadratic (2^{nd} order) polynomial interpolation for each velocity component and that of P indicate a complete polynomial for the pressure interpolation while the negative subscript denotes the discontinuous function between adjacent elements. The Q_2-P_{-1} element was also confirmed the best accurate, optimal, and robust element for viscous incompressible flow computation by various literatures [47-54]. The Q_2-P_{-1} element is illustrated in **Figure 3.2**, in which the velocity vectors were approximated using 9-node biquadratic quadrilateral elements while the pressure field was approximated linearly (1 node at the centre with two derivatives).

The shape functions for Q_2-P_{-1} element are presented in local coordinates ξ and η as follows:

For velocity (9 nodal points)

$$\lfloor N_u(\xi,\eta)\rfloor = \lfloor N_{u1}(\xi,\eta) \;\; N_{u2}(\xi,\eta) \;\; N_{u3}(\xi,\eta) \;\; N_{u4}(\xi,\eta) \;\; N_{u5}(\xi,\eta) \;\; N_{u6}(\xi,\eta) \;\; N_{u7}(\xi,\eta) \;\; N_{u8}(\xi,\eta) \;\; N_{u9}(\xi,\eta)\rfloor$$

$$N_{u1}(\xi,\eta)=\frac{1}{4}(1-\xi)(1-\eta)\xi\eta$$

$$N_{u2}(\xi,\eta)=-\frac{1}{4}(1+\xi)(1-\eta)\xi\eta$$

$$N_{u3}(\xi,\eta)=\frac{1}{4}(1+\xi)(1+\eta)\xi\eta$$

$$N_{u4}(\xi,\eta)=-\frac{1}{4}(1-\xi)(1+\eta)\xi\eta$$

$$N_{u5}(\xi,\eta)=-\frac{1}{2}(1-\xi)(1+\xi)(1-\eta)\eta$$

$$N_{u6}(\xi,\eta)=\frac{1}{2}(1+\xi)(1-\eta)(1+\eta)\xi$$

$$N_{u7}(\xi,\eta)=\frac{1}{2}(1-\xi)(1+\xi)(1+\eta)\eta$$

$$N_{u8}(\xi,\eta)=-\frac{1}{2}(1-\xi)(1-\eta)(1+\eta)\xi$$

$$N_{u9}(\xi,\eta)=(1-\xi)(1+\xi)(1-\eta)(1+\eta) \tag{3.32}$$

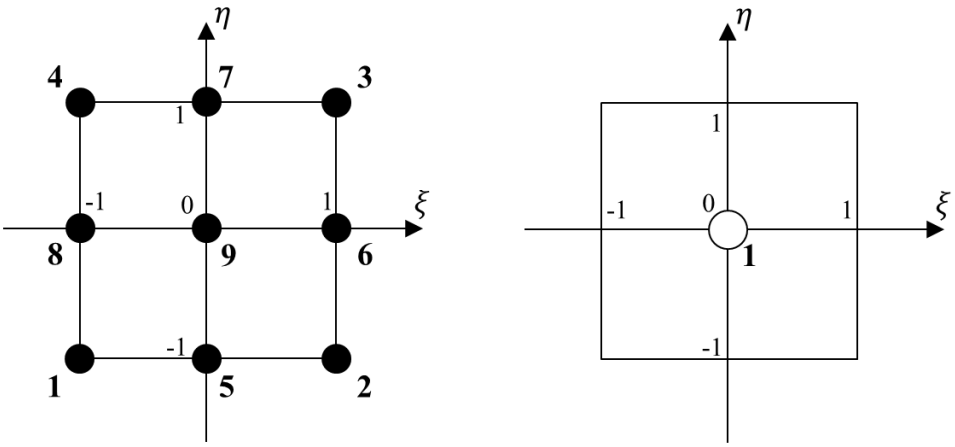

Velocity: biquadratic
(9 nodal points)

Pressure: discontinuous linear
(1 nodal point, 2 derivatives)

Figure 3.2 Q_2-P_{-1} element

For pressure (1 nodal point, 2 derivatives)

$$\lfloor N_p(\xi,\eta)\rfloor=\lfloor N_{p1}(\xi,\eta) \quad N_{p2}(\xi,\eta) \quad N_{p3}(\xi,\eta)\rfloor$$

$$N_{p1}(\xi,\eta)=1$$

$$N_{p2}(\xi,\eta)=\xi$$

$$N_{p3}(\xi,\eta)=\eta \tag{3.33}$$

For the approximation of lateral displacement of the panel, the two-node bending element with four degree of freedom as presented in **Figure 3.3** was employed. d_1 and d_2 represent the lateral displacement at the node 1 and 2 of the element. $\frac{\partial d_1}{dx}$ and $\frac{\partial d_2}{dx}$ are the rotation at each node. l is the length of element. The shape functions of the two-node bending element are derived based on the cubic interpolation function, which satisfies the governing equation of the panel domain. Furthermore, the cubic interpolation function is able to provide the continuity of lateral displacement and slope at sharing nodes between continuous elements. The shape function derivation and accuracy investigation for this element type were offered in [55].

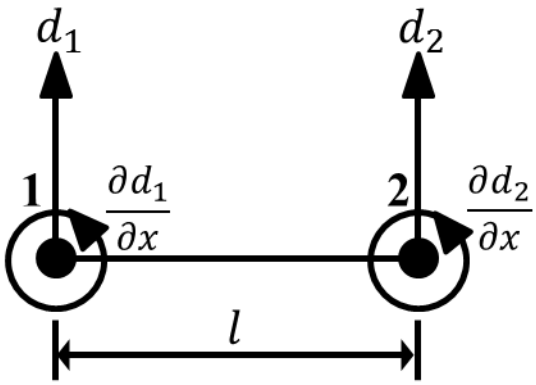

Figure 3.3 2-node bending element

The shape functions for the two-node bending element are presented in local coordinates as follows:

$$\lfloor N_d(\xi)\rfloor=\lfloor N_{d1}(\xi) \quad N'_{d1}(\xi) \quad N_{d2}(\xi) \quad N'_{d2}(\xi)\rfloor$$

$$N_{d1}(\xi)=1-\frac{3}{4}(\xi+1)^2+\frac{1}{4}(\xi+1)^3$$

$$N'_{d1}(\xi)=\frac{l}{2}(\xi+1)-\frac{l}{2}(\xi+1)^2+\frac{l}{8}(\xi+1)^3$$

$$N_{d2}(\xi)=\frac{3}{4}(\xi+1)^2-\frac{1}{4}(\xi+1)^3$$

$$N'_{d2}(\xi)=-\frac{l}{2}(\xi+1)^2+\frac{l}{8}(\xi+1)^3 \tag{3.34}$$

The proposed feature of this study is to include the thickness of sandwich panel into the mesh model. The finite element mesh model including the panel thickness is presented in **Figure 3.4.** However, the finite element mesh models excluding the panel thickness as shown in **Figure 3.5** was also used to compare the obtained results and clarify the influence of this improvement. The thickness of sandwich panel was included by separating the upper and lower air-panel interface. The boundary conditions of air velocity nodes on the upper and lower interface were set to be identical to the time derivative of the displacement of corresponding panel nodes. This concept is coherent with the assumption of the sandwich model that the core is so stiff in transverse direction that the lateral motions of two faces are synchronous.

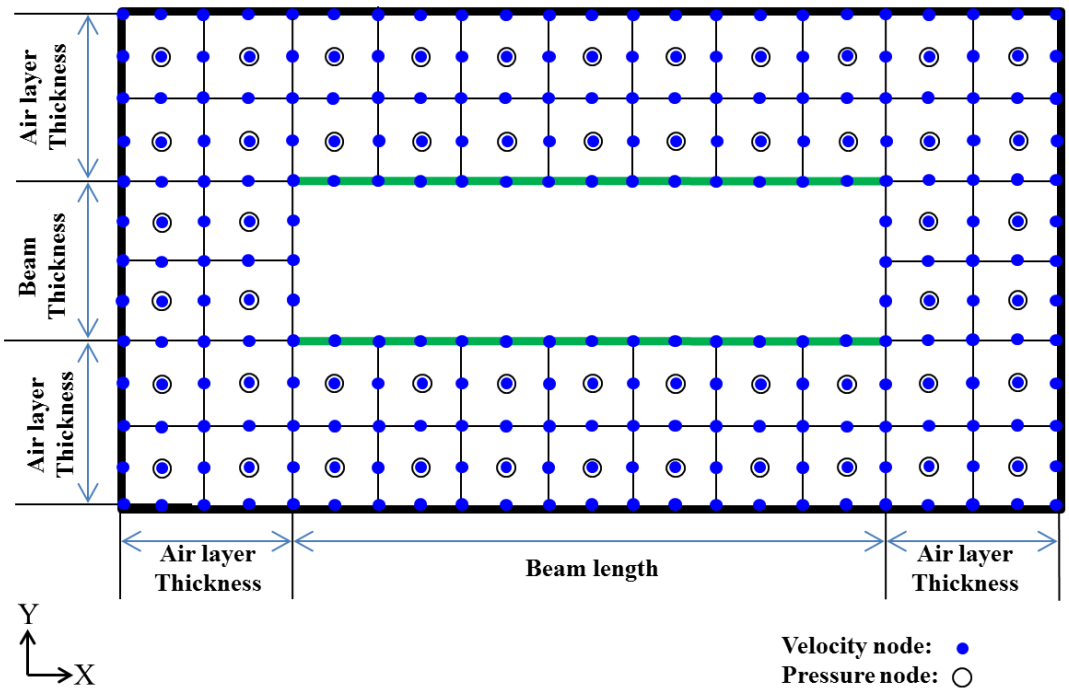

Figure 3.4 Finite element mesh model including panel thickness

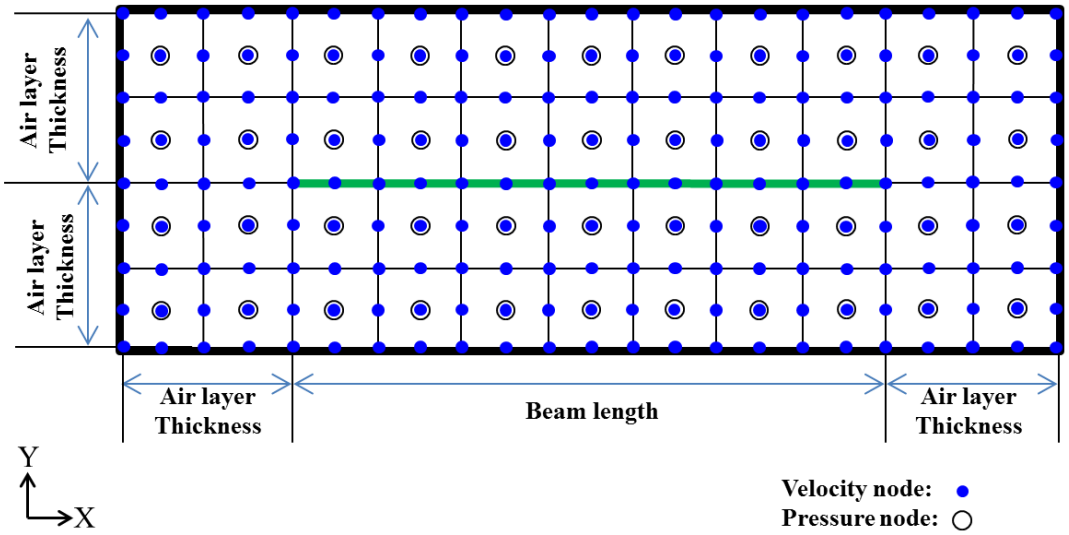

Figure 3.5 Finite element mesh model excluding panel thickness

Chapter 4
Parametric studies and discussions

4.1 Verification of finite element model

The validation of the formulation was examined by investigating the convergence of finite element results and comparing the obtained results with analytical solutions and experimental results of other researches. In addition, the finite element results are also compared with the experimental results presented in Chapter 2. In this study, the mesh convergence study was performed to determine the optimum number of elements. The mesh convergence plot for the natural frequency versus the number of air element is illustrated in **Figure 4.1**, while the convergence test on the panel elements refinement is clarified in the next section, which also compares the finite element results with analytical solution. In the analysis, the air and panel region were discretized into 168 and 30 elements, respectively and the total number of DOFs is 1561. The physical properties of the air were based on the normal temperature and pressure (20 °C, 1 atm), where air mass density (ρ_A) = 1.205 kg/m^3, viscous coefficient (μ) = 1.809 × 10^{-5} Pa·s, and speed of sound (c)= 343.43 m/s. To assure the versatility of the present formulation, three sandwich panels (A, B, and C) with different geometrical and material properties were employed for this study. The geometrical and material properties of Sandwich A and B were adopted from various literatures [23,39] while those of Sandwich C was adopted from the specimen used in Chapter 2.

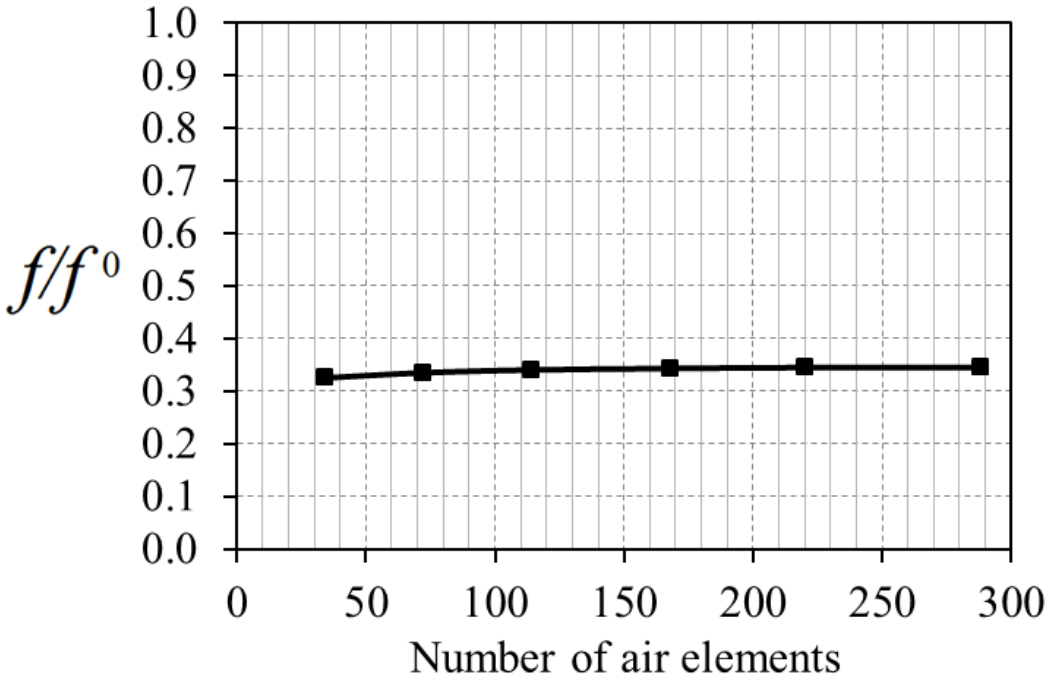

Figure 4.1 Mesh convergence plot of natural frequency versus number of air elements

Table 4.1 Geometrical and material properties

Sandwich panel	A	B	C
Panel length_L (m)	1.2	1.2	0.4
Panel width_b (mm)	1.0	1.0	50
Face thickness_t_f (mm)	0.5	1.0	0.1
Core thickness_t_c (mm)	10	10	5.0
Face density_ρ_f (kg/m^3)	1.26×10^3	2.77×10^3	2.68×10^3
Core density_ρ_c (kg/m^3)	1.38×10^2	0.6×10^2	0.37×10^2
Face Young's modulus_E_f (Pa)	32.0×10^9	70.0×10^9	70.0×10^9
Core Young's modulus_E_c (Pa)	13.0×10^7	13.0×10^7	24.1×10^7
Core shear modulus_G_c (Pa)	13.6×10^7	45.0×10^6	34.5×10^7

In this part, the first eight natural frequencies of sandwich panel A, B, and C, calculated by using the present finite element analysis are compared with those calculated by using the Euler-Bernoulli and Sandwich approximation. The geometrical and material properties of sandwich panel A, B, and C are presented in **Table 4.1**. The boundary condition of the panel A and B is simply support and that of the panel C is fixed ends. In this comparison, the effect of ambient air was not considered. The effect of ambient air was disregarded from the finite element analysis by setting the air boundary to be the condition of infinite vacuum air domain. In this setting, the rigid walls were removed and the parameters of the air viscosity coefficient and mass density were inputted with 5-digit smaller than the value of standard condition. The analytical solutions based on the classical Euler-Bernoulli and Sandwich theory are clarified in equation (4.1) and (4.2), respectively. The derivation and analytical solutions of sandwich panel under fixed ends condition can be found in the reference [39].

$$f_{EB} = \frac{\pi}{2} \cdot \left(\frac{n}{L}\right)^2 \cdot \sqrt{\frac{D_B}{\rho_B}} \quad \text{for simply supported}$$

$$f_{EB} = \frac{\pi}{2} \cdot \left(\frac{0.5+n}{L}\right)^2 \cdot \sqrt{\frac{D_B}{\rho_B}} \quad \text{for fixed ends} \tag{4.1}$$

$$f_{SW} = \frac{\pi}{2} \cdot \left(\frac{n}{L}\right)^2 \cdot \sqrt{\frac{D_B\left(2D_f\pi^2n^2 + G_c t_c L^2\right)}{\rho_B\left(\left(D_B + 2D_f\right)\pi^2n^2 + G_c t_c L^2\right)}} \quad \text{for simply supported} \tag{4.2}$$

Here, n and L denote the vibrational mode order and sandwich panel length.

The comparisons of the first eight natural frequencies calculated by finite element, Euler-Bernoulli, and Sandwich approximation are presented in **Table 4.2**, **4.3**, and **4.4**

for sandwich panel A, B, and C, respectively. In addition, the number of panel elements (N) was varied to investigate the convergence of the results. The natural frequencies obtained from finite element model tend to converge to those calculated by using Sandwich approximation and show more agreement with those calculated using Sandwich approximation than those estimated using Euler-Bernoulli solution. The natural frequencies of Euler-Bernoulli solution are slightly higher than those of finite element model and Sandwich approximation because the assumption of Euler-Bernoulli approximation neglects the shear deformation effect by considering the shear modulus to be infinity, leading to the overestimated bending stiffness and natural frequency. The deviation from the Euler-Bernoulli solution increases as the mode order steps up. For the panel B having the lower shear modulus than the panel A and C, the deviation of natural frequencies can be seen obviously. The deviation indicates the necessity of taking the shear deformation effect into the calculation of natural frequency especially for a sandwich structure with weak core.

As previously explained, the obtained finite element results were compared with the experimental results of other researches [23,34] to verify the finite element model. The first three natural frequencies of three sandwich panels are compared in **Table 4.5**. The natural frequencies are presented in normalized form (f/f^0), where f is the natural frequency under normal pressure and f^0 is the natural frequency in vacuum condition. In this comparison, the boundary condition of finite element model was modified by removing the rigid wall surrounding the ambient air and the ambient air thickness is set to be 1000 mm. For the vacuum condition, the air viscosity coefficient and mass density were inputted with 5-digit smaller than the value of standard condition.

Table 4.2 Estimated natural frequency for Sandwich panel A without air effect

Vibrational mode's order	Sandwich A natural frequency (Hz)					
	Finite element				Analytical Euler-Bernoulli	Analytical Sandwich
	N=10	N=20	N=30	N=40		
1	19.921	19.905	19.903	19.902	19.946	19.902
2	79.158	79.098	79.089	79.083	79.784	79.083
3	176.191	176.058	176.038	176.023	179.513	176.024
4	308.643	308.409	308.374	308.349	319.135	308.351
5	473.489	473.130	473.076	473.037	498.648	473.040
6	667.293	666.787	666.711	666.657	718.053	666.661
7	866.442	885.770	885.669	885.597	977.349	885.602
8	1127.344	1126.489	1126.361	1126.269	1276.538	1126.275

Table 4.3 Estimated natural frequency for Sandwich panel B without air effect

Vibrational mode's order	Sandwich B natural frequency (Hz)					
	Finite element				Analytical Euler-Bernoulli	Analytical Sandwich
	N=10	N=20	N=30	N=40		
1	27.826	27.810	27.804	27.803	28.688	27.803
2	102.371	102.313	102.292	102.287	114.751	102.288
3	205.495	205.378	205.336	205.326	258.190	205.328
4	322.266	322.266	322.017	322.000	459.005	322.003
5	444.053	444.053	443.963	443.941	717.195	443.945
6	567.803	567.479	567.363	567.336	1032.761	567.340
7	691.263	690.868	690.728	690.694	1405.702	690.700
8	814.225	813.760	813.594	813.555	1836.019	813.562

Table 4.4 Estimated natural frequency for Sandwich panel C without air effect

Vibrational mode's order	Sandwich C natural frequency (Hz)					
	Finite element				Analytical Euler-Bernoulli	Analytical Sandwich
	N=10	N=20	N=30	N=40		
1	274.339	247.323	247.322	247.321	248.226	247.322
2	682.653	682.611	682.608	682.605	689.516	682.606
3	1325.373	1325.290	1325.285	1325.280	1351.451	1325.282
4	2163.990	2163.855	2163.846	2163.837	2234.032	2163.840
5	3184.363	3184.163	3184.151	3184.137	3337.257	3184.142
6	4370.540	4370.266	4370.248	4370.230	4661.128	4370.237
7	5705.584	5705.228	5705.204	5705.180	6205.643	5705.188
8	7172.319	7171.871	7171.842	7171.812	7970.804	7171.822

The agreement between the obtained finite element results and the experimental results of other researches is satisfied. The results show that the ambient air affects the vibration of sandwich panel as an added mass effect resulting in the reduction of natural frequency. As compared with the natural frequency in vacuum condition, the natural frequency decreases of about 10, 4, and 3% for vibrational mode 1, 2, and 3, respectively. The results also show that the effect of ambient air increases when the panel mass becomes lighter.

Table 4.5 Comparison with experimental of other researches

Panel	Mass/area (kg/mm^2)	f/f^0 (FEM)			f/f^0 [23,34] (Experiment of other researches)		
		Mode1	Mode2	Mode3	Mode1	Mode2	Mode3
SW1	4.66×10^{-6}	0.90	0.95	0.98	0.94	0.98	0.99
SW2	4.10×10^{-6}	0.89	0.94	0.97	0.92	0.96	0.97
SW3	2.60×10^{-6}	0.83	0.92	0.93	0.86	n/a	n/a

4.2 Influence of shear deformation

The influence of shear deformation in sandwich core was further investigated in this part. The variation of the core shear modulus was conducted to illustrate the characteristic of this effect while the values of other parameters were still equivalent as listed in **Table 4.1**. **Figure 4.2-4.4** show the alteration of the first three natural frequencies through the adjustment of core shear modulus of sandwich panel A, B, and C, respectively. The abscissa of **Figure 4.2-4.4** is the shear modulus (G_c). The ordinate is f/f^0, where f is the natural frequency obtained by including shear deformation effect and f^0 is the natural frequency that neglects this effect. The results of sandwich panel A, B, and C show similar tendency. While the core shear modulus weakens, the effect of shear deformation presents as the sharp decrease of natural frequencies. The effect is more significant in the higher vibration mode. On the other hand, as the shear modulus strengthens up to a value, which is 10 times for sandwich panel A and C, and 100 times for sandwich panel B, the shear deformation has the minor effect on their natural frequencies.

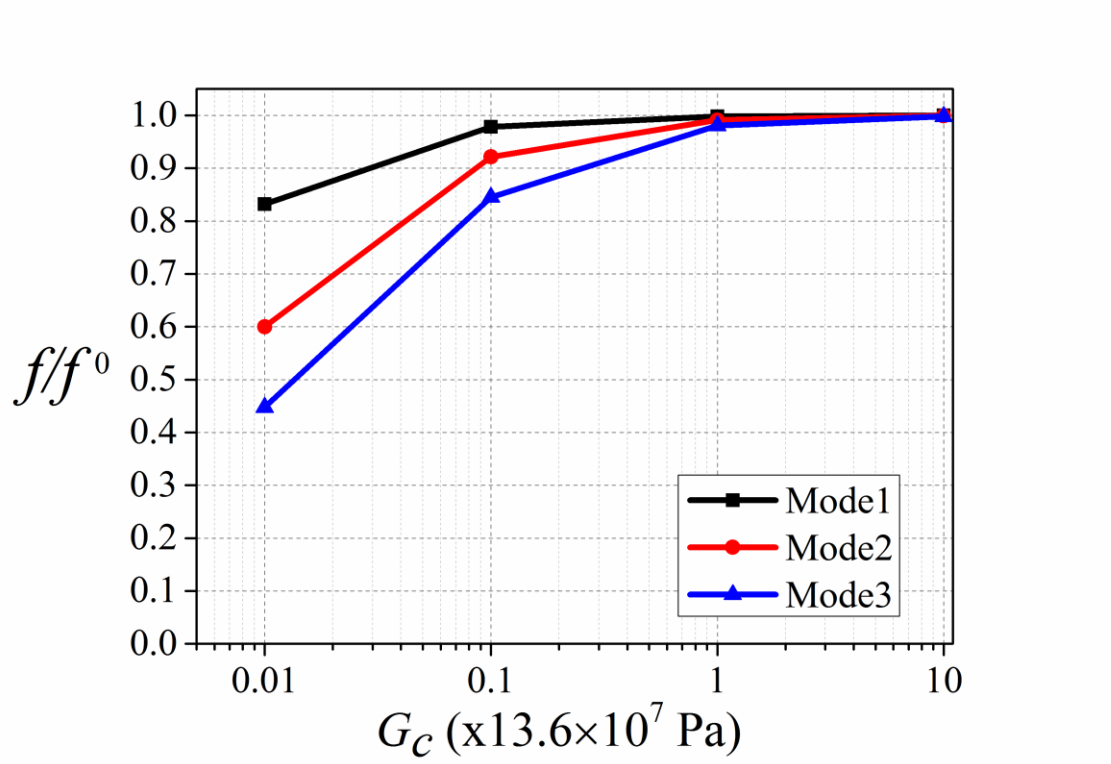

Figure 4.2 Influence of shear deformation on natural frequencies as a function of core shear modulus: Sandwich panel A

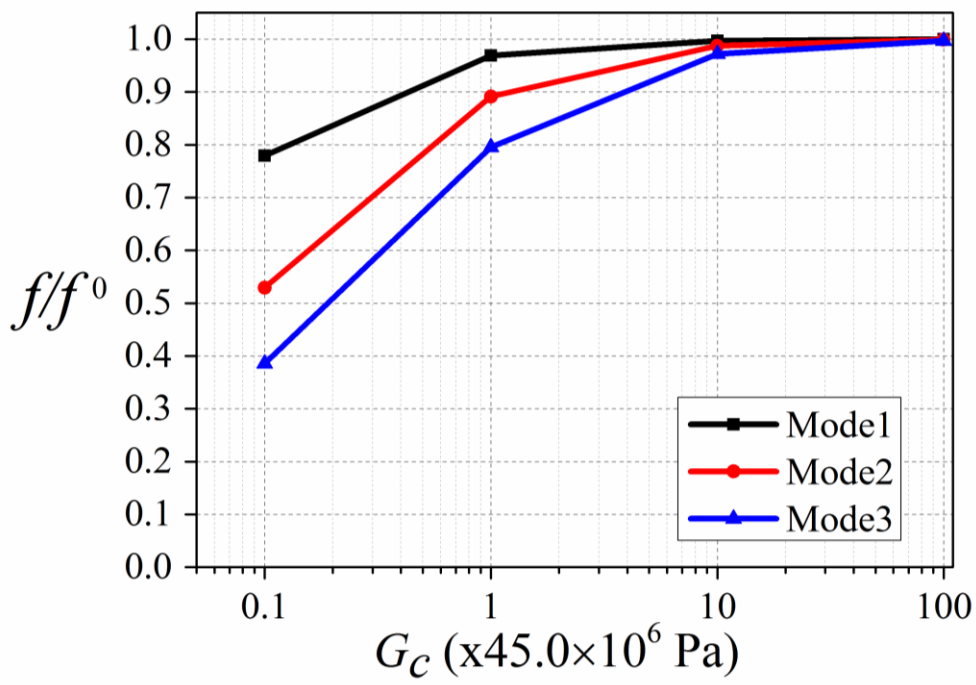

Figure 4.3 Influence of shear deformation on natural frequencies as a function of core shear modulus: Sandwich panel B

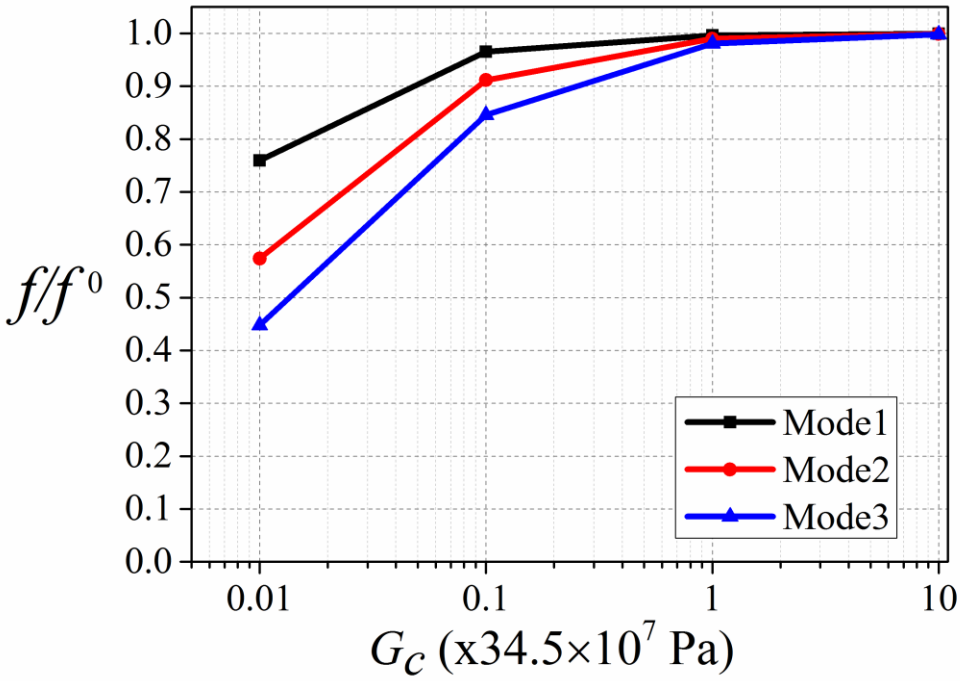

Figure 4.4 Influence of shear deformation on natural frequencies as a function of core shear modulus: Sandwich panel C

Generally, the shear deformation effect obviously presents in the case of thick panel. In the high frequency region, the bending stiffness of a sandwich panel is completely determined by the bending stiffness of the laminates [39]. Thus, in this section, the shear deformation effect on the first three natural frequencies was investigated by varying the core and face sheets thickness. **Figure 4.5-4.7** present the variation of the first three natural frequencies as the core thickness of the sandwich structure changes. **Figure 4.8-4.10** illustrate the change of natural frequencies through the variation of face thickness. The abscissa of **Figure 4.5-4.7** is the core thickness (t_c) and that of **Figure 4.8-4.10** is face thickness (t_f). The ordinate of **Figure 4.5-4.10** is identical to that of **Figure 4.2-4.4**. From the **Figure 4.5-4.10**, when the core and face sheets thickness increases, the natural frequencies tend to decline according to the increase

of shear deformation effect. As same tendency as shown in **Figure 4.2-4.4**, the effect of shear deformation is magnified as the vibration mode order increases. The results in this part conclude the importance of considering the shear deformation effect for studying the bending vibration of sandwich panels.

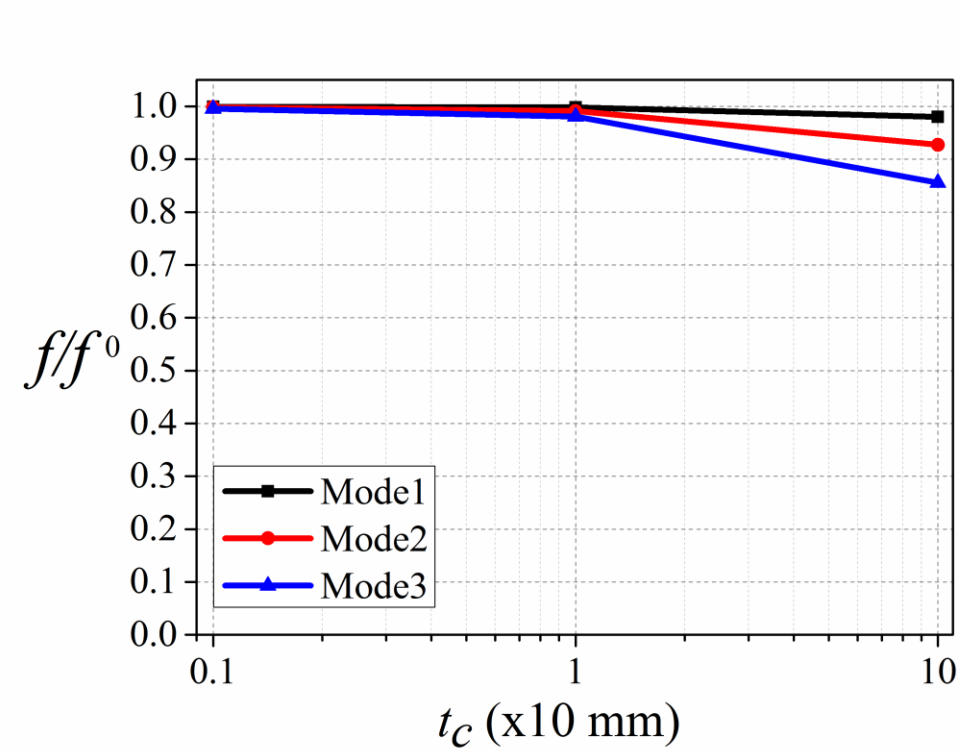

Figure 4.5 Influence of shear deformation on natural frequencies as a function of core thickness: Sandwich panel A

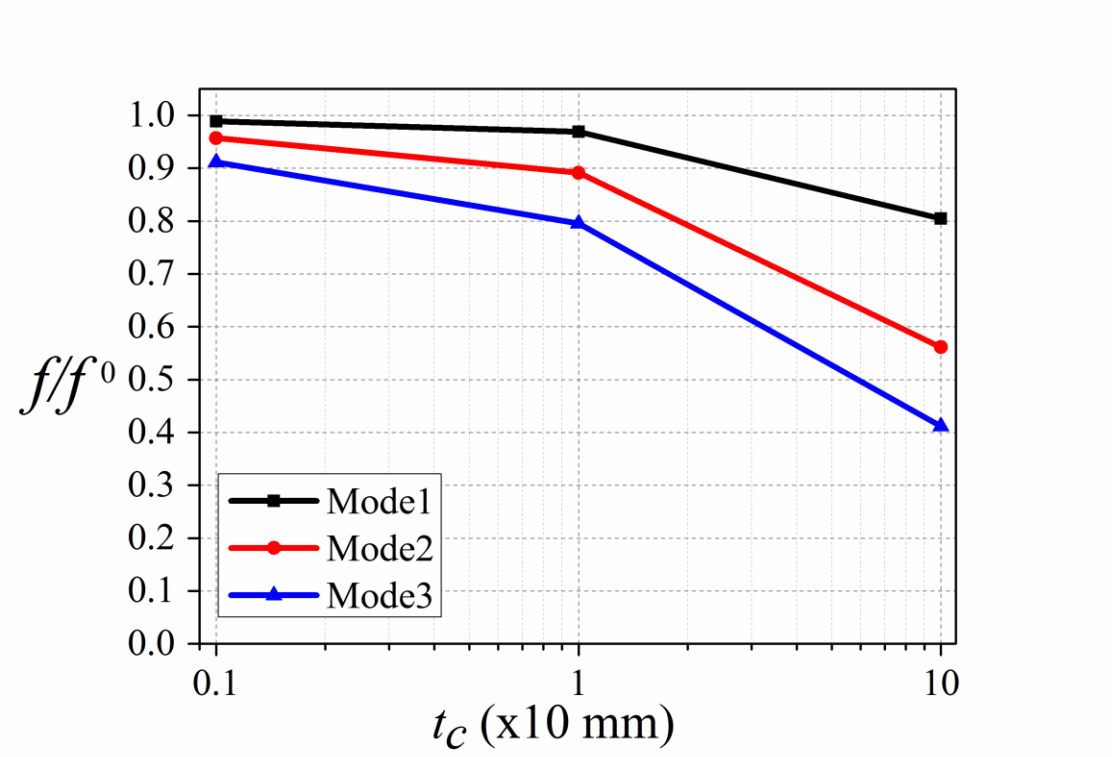

Figure 4.6 Influence of shear deformation on natural frequencies as a function of core thickness: Sandwich panel B

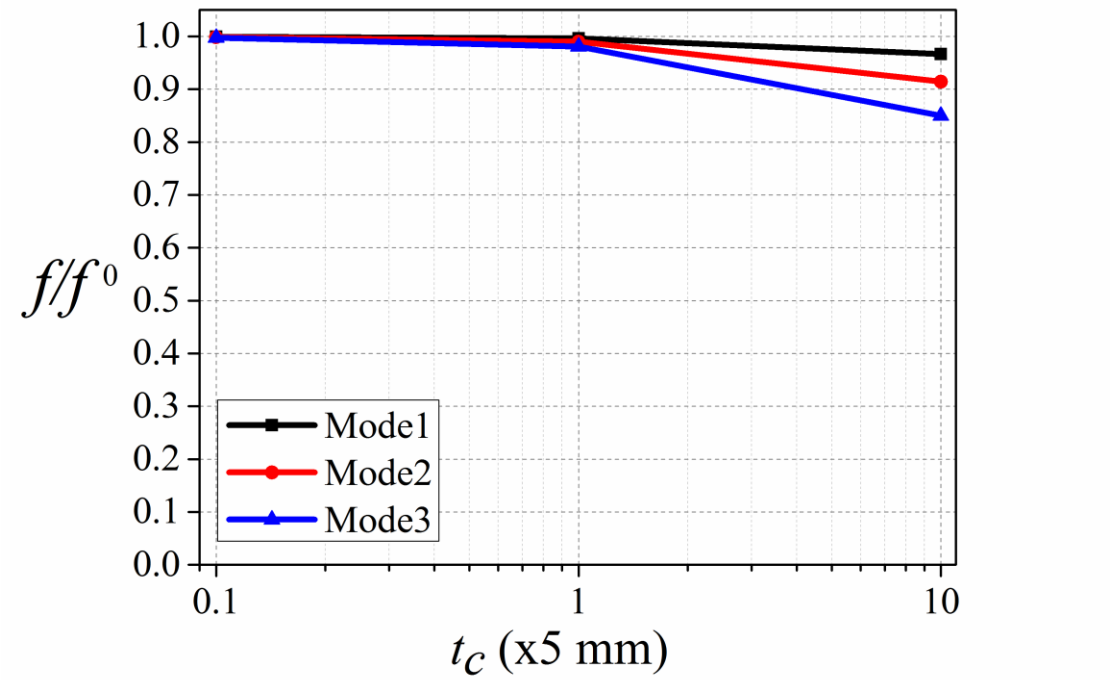

Figure 4.7 Influence of shear deformation on natural frequencies as a function of core thickness: Sandwich panel C

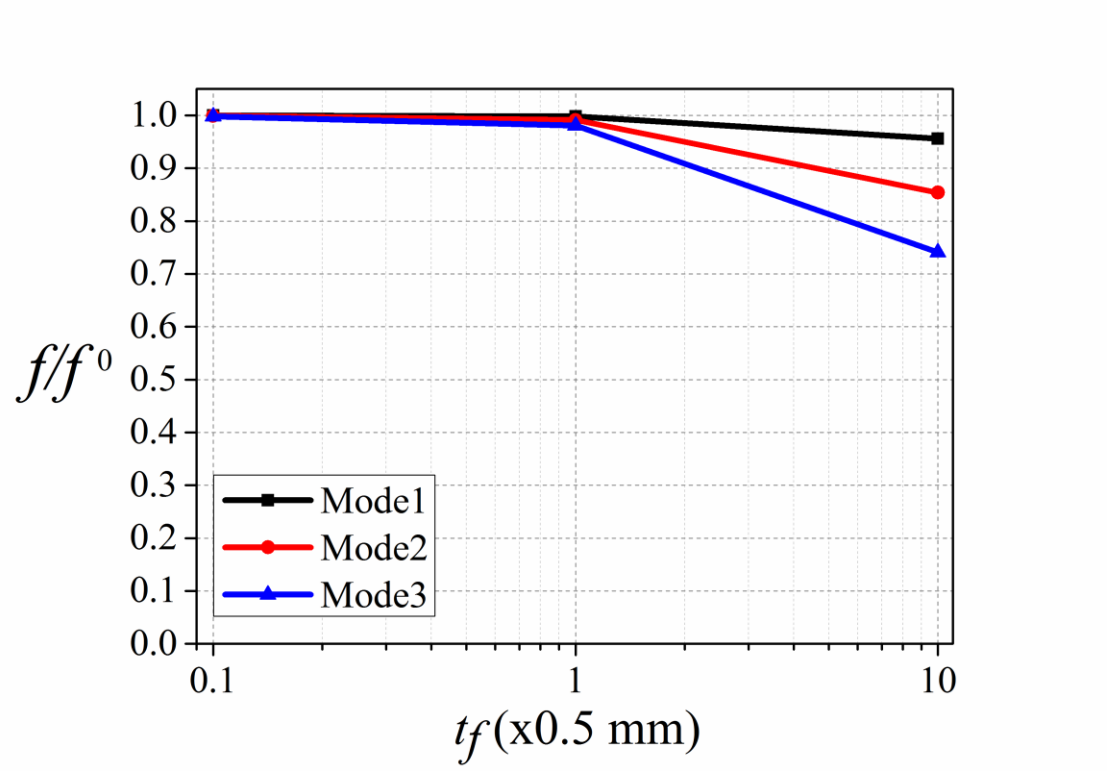

Figure 4.8 Influence of shear deformation on natural frequencies as a function of face sheet thickness: Sandwich panel A

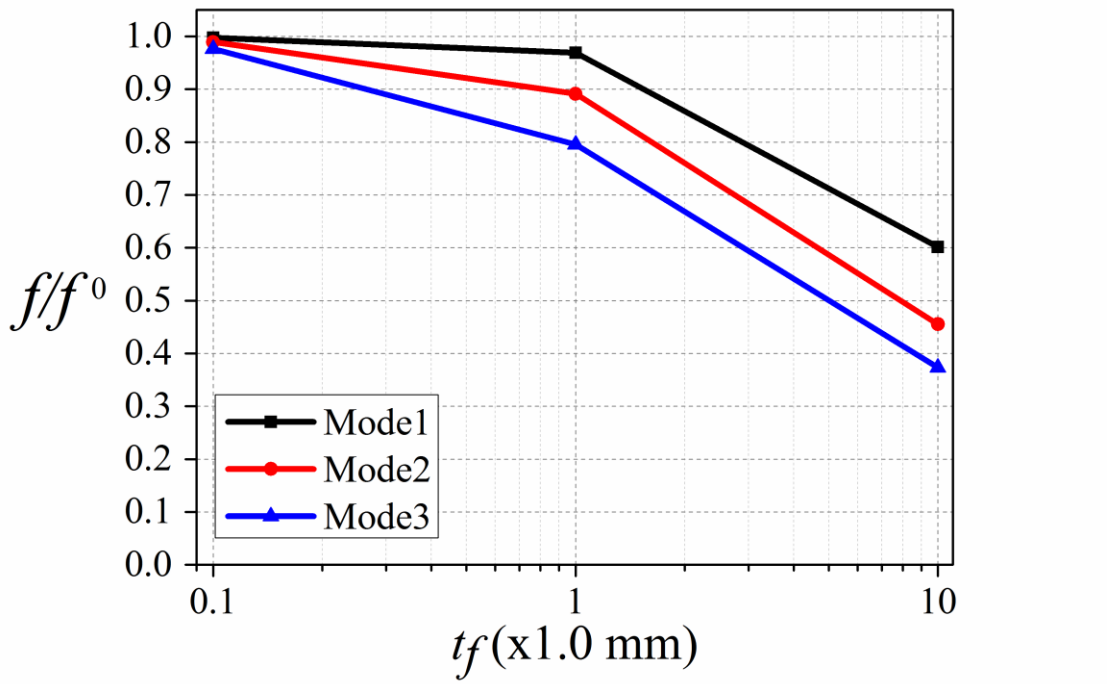

Figure 4.9 Influence of shear deformation on natural frequencies as a function of face sheet thickness: Sandwich panel B

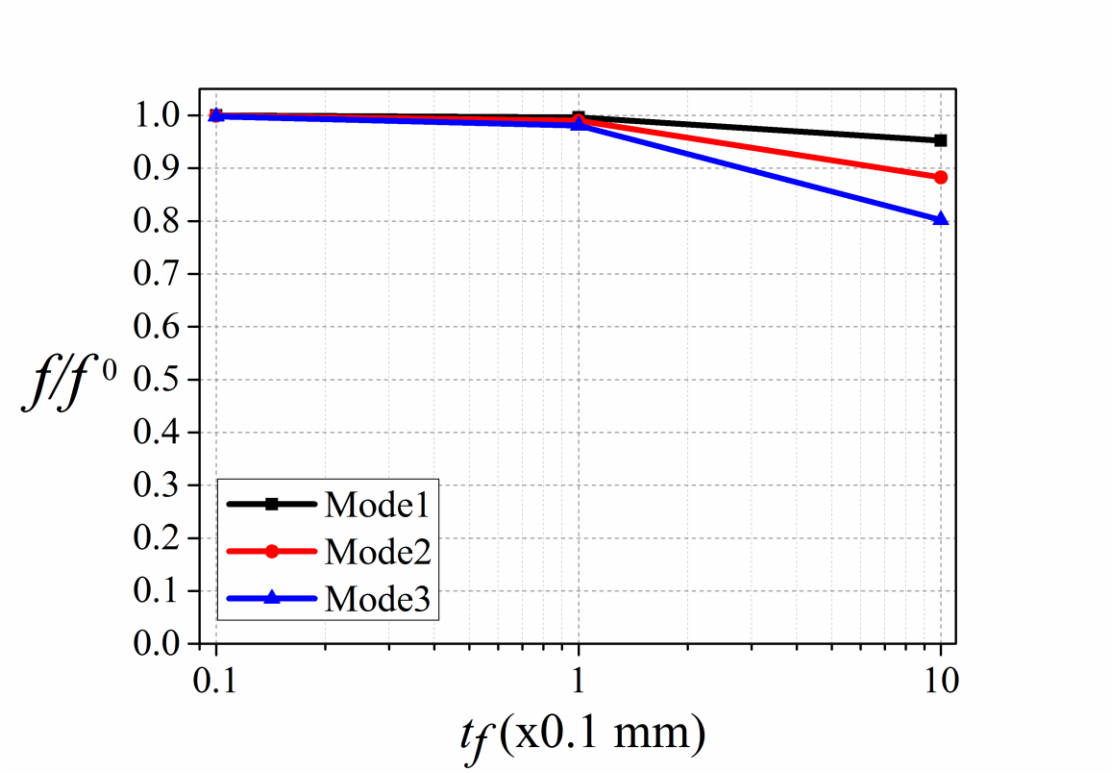

Figure 4.10 Influence of shear deformation on natural frequencies as a function of face sheet thickness: Sandwich panel C

4.3 Influence of GAP

In the section, the natural frequency of the first vibrational mode is investigated as the GAP is changed between 1 to 40 mm. In addition, to verify the experimental results, the conditions of SIDE are determined to be 1, 3, 15, 25, and 50 mm according to the experimental condition. The natural frequency variations for the SIDE condition of 1, 3, 15, 25, and 50 mm are illustrated in **Figure 4.11-4.15**, respectively. The ordinate of **Figure 4.11-4.15** is the normalized frequency f/f^{0}, where f is the natural frequency obtained by including the effect of ambient air and f^{0} is the natural frequency neglecting this effect. For the specimen used in this study, the fundamental natural frequency without air effect is 247.321 Hz. This frequency was

estimated by using the numerical simulation where the boundary condition of the model was adapted by removing the rigid surface around the panel and setting the air density and viscous coefficient to be 5 times smaller than those of the standard condition. The adapted boundary condition represents the condition of infinite vacuum air domain. The abscissa of **Figure 4.11-4.15** is the GAP/*L*, where *L* is panel length. The blue background graph provides the magnified comparison between finite element and experimental results. The finite element and experimental results show good agreement. The frequency variations of all SIDE conditions are in same tendency that the natural frequencies tend to decrease more sharply as the GAP becomes thinner.

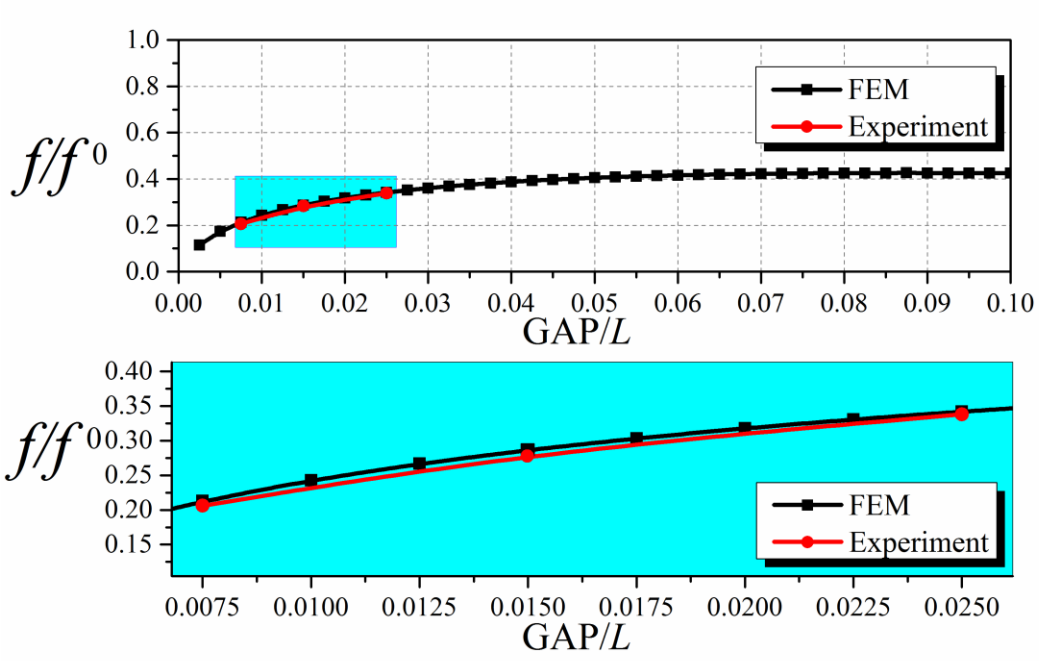

Figure 4.11 Influence of GAP: SIDE of 1 mm

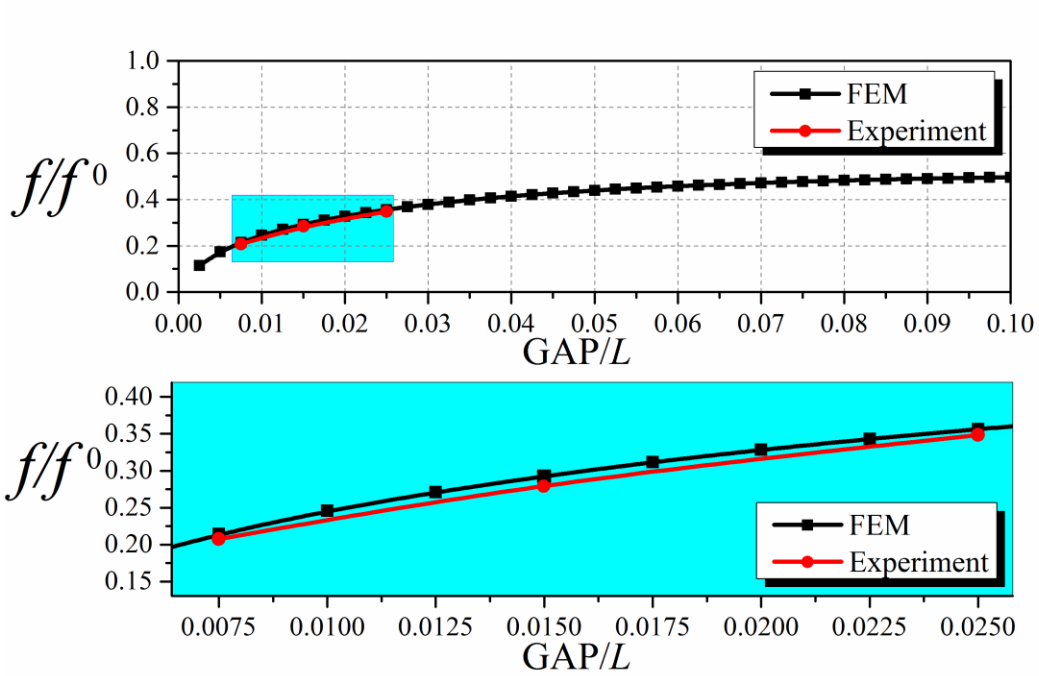

Figure 4.12 Influence of GAP: SIDE of 3 mm

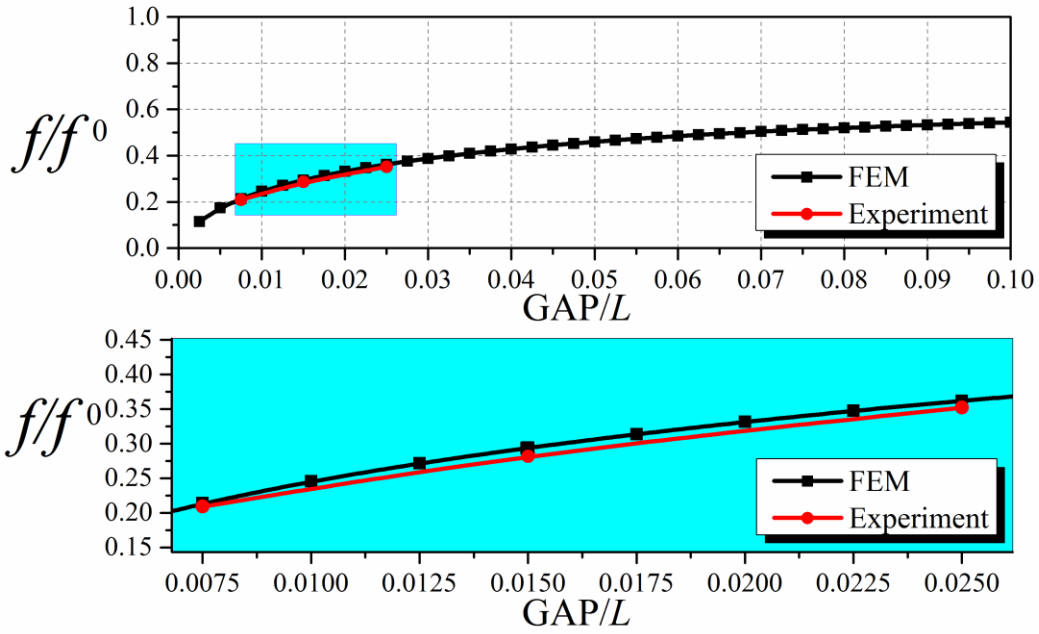

Figure 4.13 Influence of GAP: SIDE of 15 mm

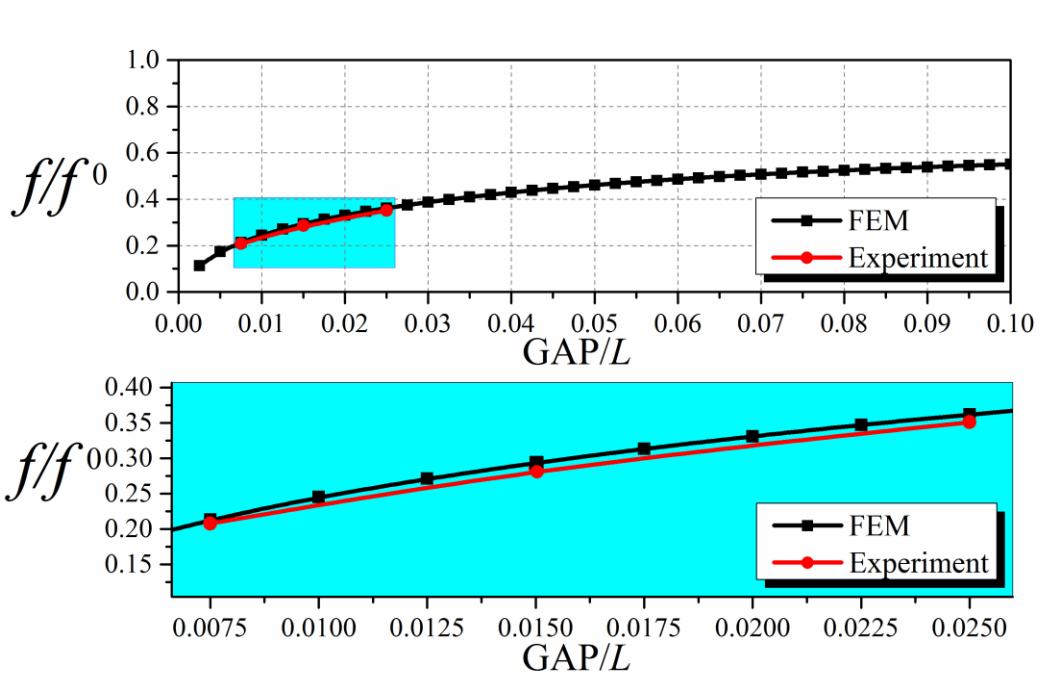

Figure 4.14 Influence of GAP: SIDE of 25 mm

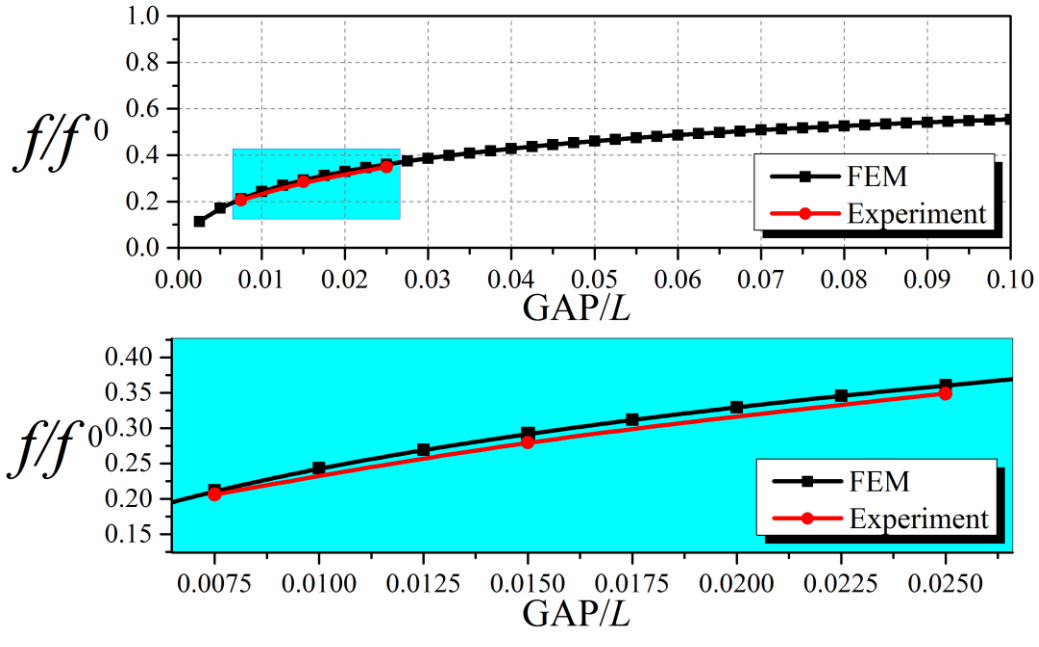

Figure 4.15 Influence of GAP: SIDE of 50 mm

The decrease of natural frequency due to the decrease of GAP can be explained by the effect of Fluid-Structure Interaction (FSI) and air mass added to sandwich panel. As shown in **Figure 4.16(a)**, the bending vibration of the panel causes the oscillatory air flow between the upper and lower cavity while the air flow disturbs the panel as an added mass effect. Because the density of sandwich structure and air is comparable, the added air mass can significantly modify the dynamic behaviour of the sandwich structure. As the GAP becomes smaller, the oscillatory air flow improves resulting in the increase of added mass effect and the decreases of natural frequency. The results of this study are in contrast with the results of the literature [27], where the natural frequency increases with decreasing air layer thickness. The contrast in the results is because of their different air condition and resulting effect, as comparatively illustrated in **Figure 4.16**. In the condition of the literature [27], the deformation of the panel causes a volume change in the cavity and then a pressure disturbance on the panel. The pressure disturbance affects the panel as an added stiffness effect, which shifts the panel natural frequency up.

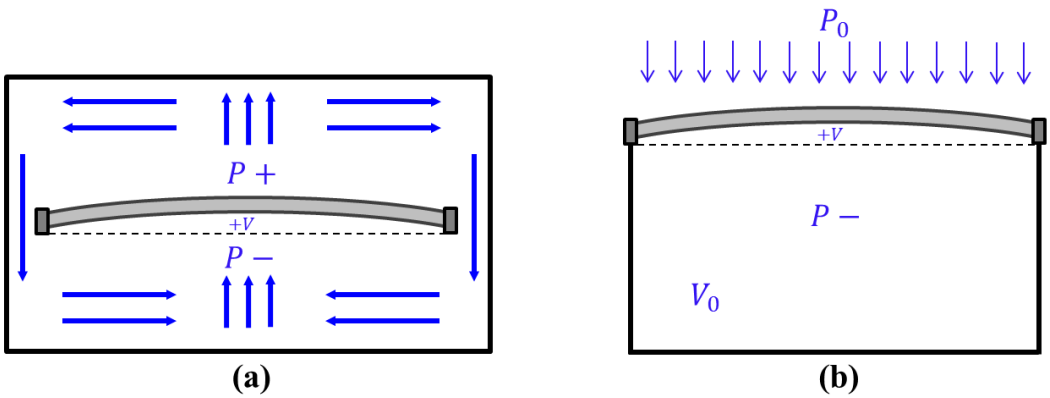

Figure 4.16 Air-panel coupling mechanism of **(a)** present model and **(b)** reference [27] model

4.4 Influence of SIDE

The influence of SIDE is studied by varying the SIDE width to be 1, 3, 5, 15, 25, and 50 mm, whereas the varying of GAP and other parameters are the same as those in section 4.3. **Figure 4.17** shows the variation of natural frequency of different SIDE width. Its ordinate and abscissa are identical to those of **Figure 4.11**-**4.15**. The effect of SIDE increases as the SIDE width decreases. However, the effect of SIDE is insignificant when the GAP becomes smaller because it is dominated by the GAP effect. As GAP/*L* is less than 0.015, SIDE variations do not affect the natural frequencies. On the contrary, the influence of SIDE prominently appears, especially for the case of narrow SIDE. The effect of SIDE leads to the reduction of natural frequency as the SIDE width becomes narrower. The reason of this phenomenon is similar to that of GAP effect explained in the previous section. The decrease of SIDE induces the pressure difference between the upper and lower cavity as shown in **Figure 4.16(a)**. The increase of pressure difference leads to the improvement of the oscillatory air flow between the upper and lower cavity and then the intensification of added air mass effect. Thus, the natural frequency decreases according to the decrease of SIDE.

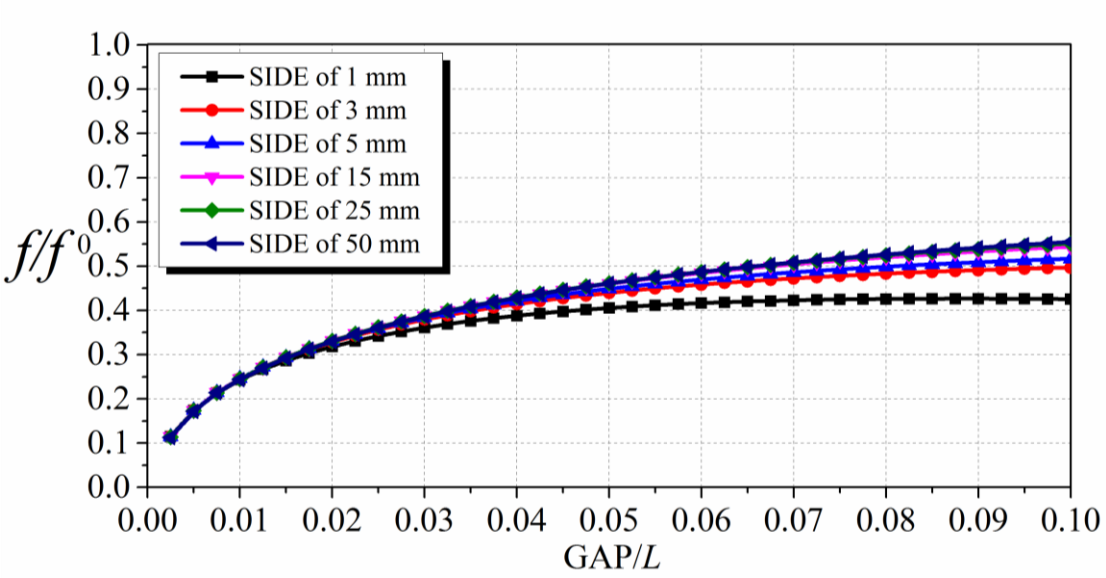

Figure 4.17 Influence of SIDE

4.5 Influence of panel length

The influence of air on the natural frequency of three panels with different lengths is investigated. The condition of panel length of 400 mm and SIDE of 50 mm is selected as the baseline for this comparison. The other panel length is set to be the half and the twice of the baseline (1/2 *L* and 2 *L*). In **Figure 4.18**, the relation between the GAP/*L* and the normalized frequency f/f^{0} is plotted for three panel spans. The frequency of each panel is normalized by its f^{0} corresponding to its length. Perceptibly, the effect of air on the natural frequency becomes stronger when the length is extended. This result can be simply explained that the increase of panel length leads to the longer air layer and thus the increment of added air mass effect, which results the decrease of natural frequency.

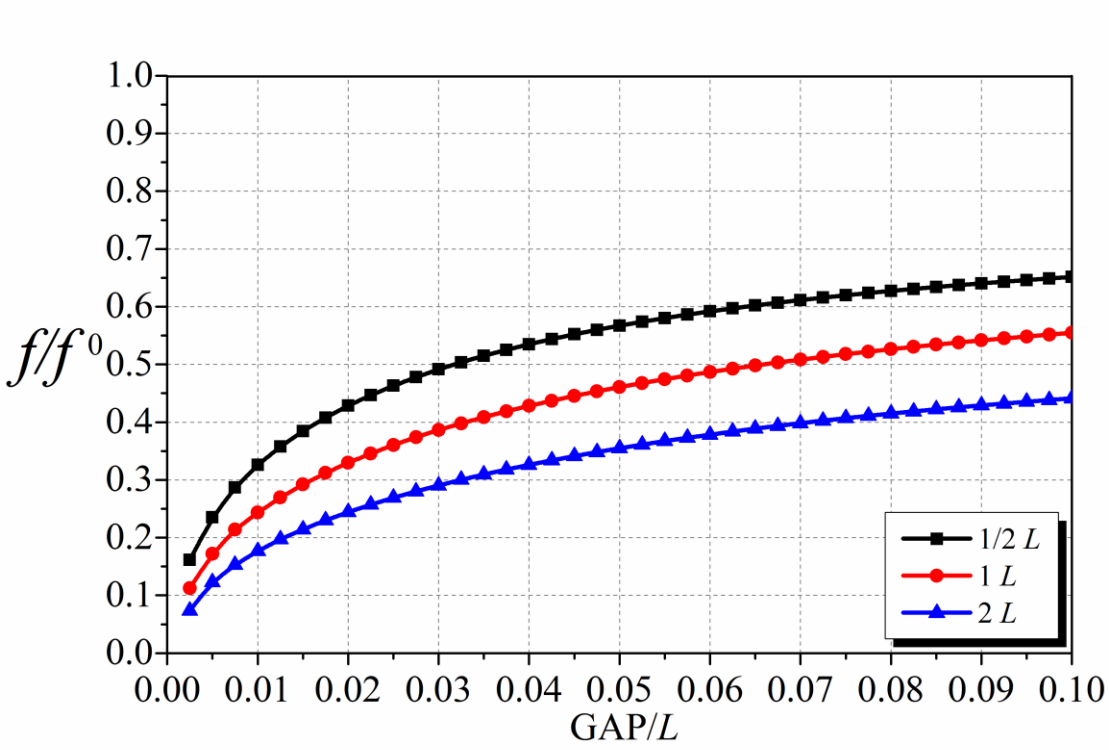

Figure 4.18 Influence of panel length

4.6 Influence of panel bending stiffness

The influence of air effect on the natural frequency of three different panels with different bending stiffness is investigated as shown in **Figure 4.19**. The ordinate and abscissa of **Figure 4.19** are identical to those of **Figure 4.11-4.15**. The simulation result of **Figure 4.15** is used as the baseline. The bending stiffness of the panel is varied to be 10 times smaller and larger than that of the baseline whereas the other parameters are identical to those of the baseline. The comparison in **Figure 4.19** shows that the frequencies of three different panels are quite identical except for the extremely small GAP/*L* region, which reveals only small difference. In the very small GAP/*L* region, the air effect becomes little stronger as the bending stiffness is reduced. The stronger effect can be explained that the structures with lower stiffness

are easier disturbed by the added mass effect than those with higher stiffness and the added mass effect is magnified in thin GAP range.

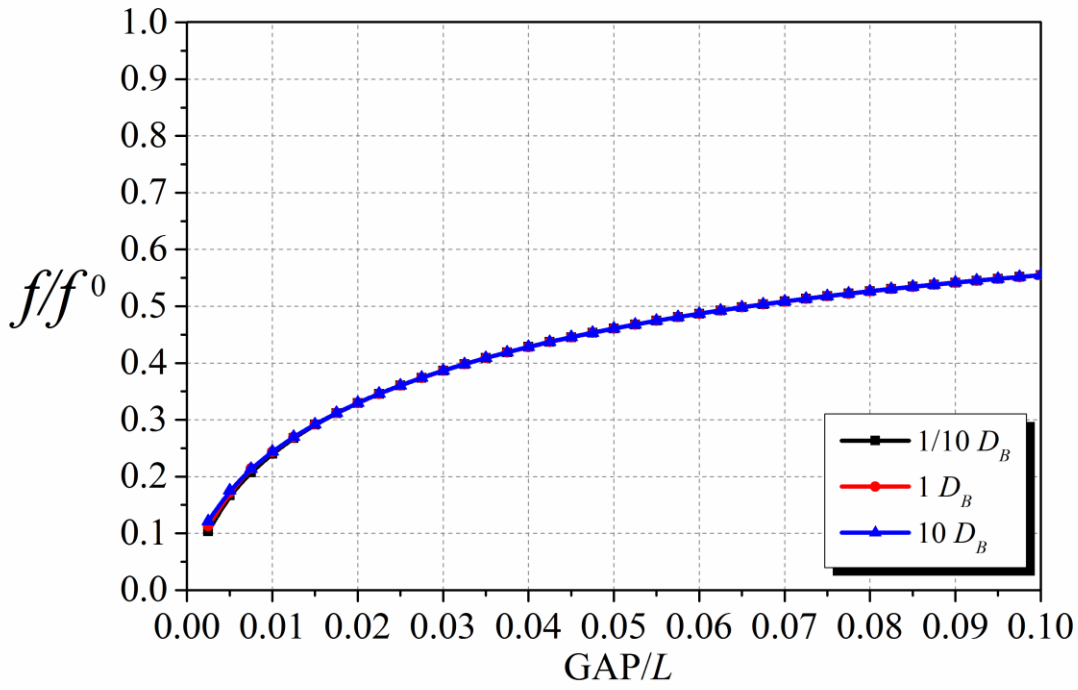

Figure 4.19 Influence of panel bending stiffness

4.7 Influence of panel mass

The difference of the air effect on different structural mass densities is presented in **Figure 4.20**. The simulation result of **Figure 4.11** is used as the baseline. The ordinate and abscissa of **Figure 4.20** are also identical to those of **Figure 4.11-4.15**. The mass density is varied between 10 times smaller and larger than that of the baseline. The alteration of structural mass substantially modifies the effect of ambient air layers. As the structural mass density is minimized, the natural frequency decreases manifestly because the added air mass effect becomes more prominent. The results in this section show good agreement with those of the reference [28] which

revealed the importance of added air mass effect on the vibrational response of light weight structures. The comparison in this section evidently proves that the air effect on structural vibration should not be neglected, especially for the case of light weight structure.

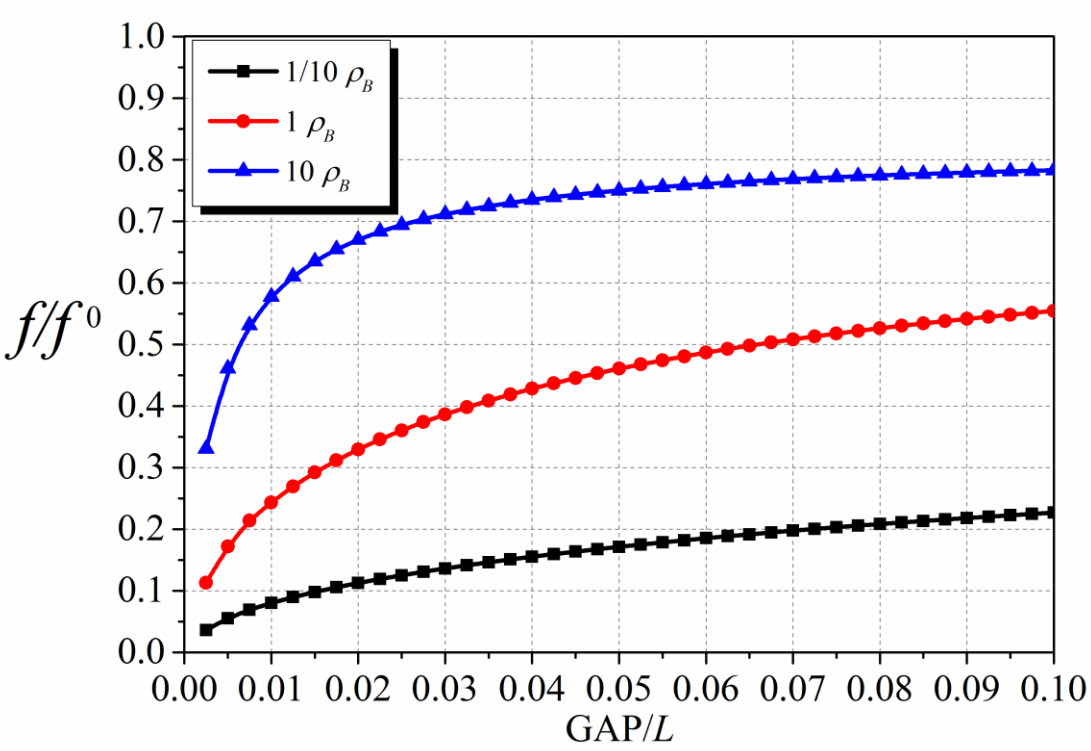

Figure 4.20 Influence of panel mass

4.8 Influence of vibration mode

In this section, the influence of ambient air on the first three natural frequencies is investigated by simultaneously varying the GAP and SIDE, which are commonly called the air layer thickness (t_a). The frequency variation of sandwich panel A, B, and C is shown in **Figure 4.21**, **4.22**, and **4.23**, respectively. The ordinate of **Figure 4.21-4.23** is f/f^0 as identical as that of **Figure 4.11-4.15**. The abscissa is the air layer thickness normalized by the core thickness (t_a/t_c). The frequency changes

of three panels are in same tendency. The frequencies decrease while the air layer thickness becomes thinner and the frequencies tends to decrease more sharply when t_a/t_c is less than one.

By considering the vibrational mode order, the effect of ambient air (added mass) decreases as the mode order or frequency increases, the results are in agreement with the discussion of Reference [39] that explained that the added mass effect is decreasing for increasing frequencies up to the critical frequency. To further substantiate these results, the characteristics of air flow velocity vector and pressure distribution are shown in **Figure 4.24**, **4.25**, and **4.26** for 1st mode, 2nd mode, and 3rd mode, respectively. For the reason that both sides are symmetry, only the half left is presented to identify their details. These characteristics are in the condition of air layer with 20 mm thickness. For each vibrational mode, the vector plots were normalized by the maximum absolute value of the time derivation of the panel displacement. The pressure distributions of each mode were also normalized by their own maximum value. The results show that the size of air velocity vector of the 1st mode (**Figure 4.24)** is larger than that of the 2nd mode (**Figure 4.25)**, which is larger than that of the 3rd mode (**Figure 4.26)**. In other words, the larger size of air flow vector occurs in the lower mode. The larger size of air velocity vector, which represents the intense air flow, indicates the stronger added mass effect. These results provide the explanation why the air effect is stronger in the lower mode.

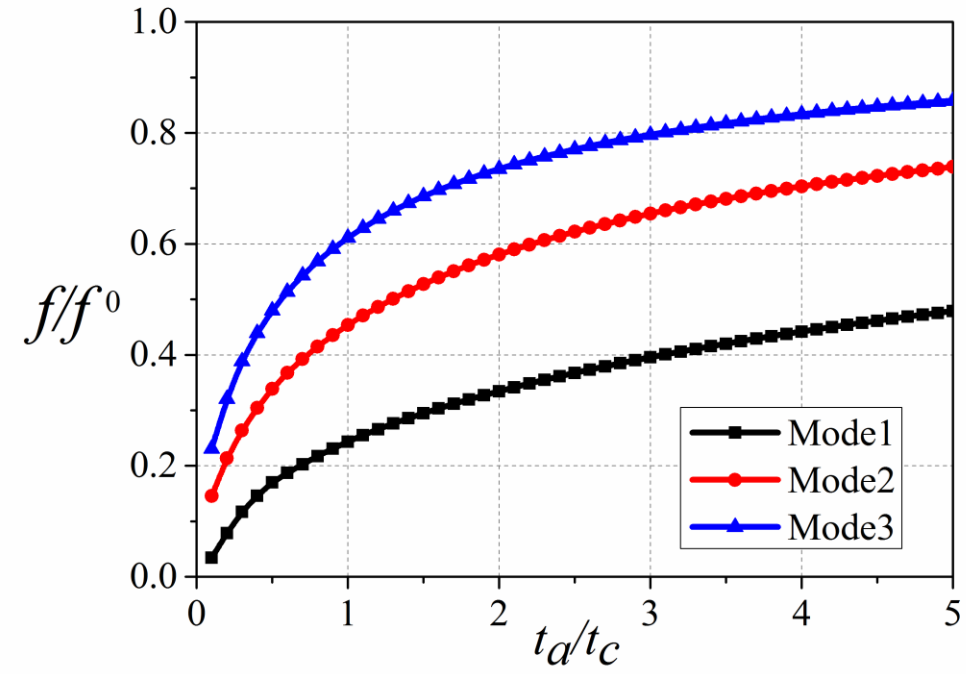

Figure 4.21 Influence of vibration mode: Sandwich panel A

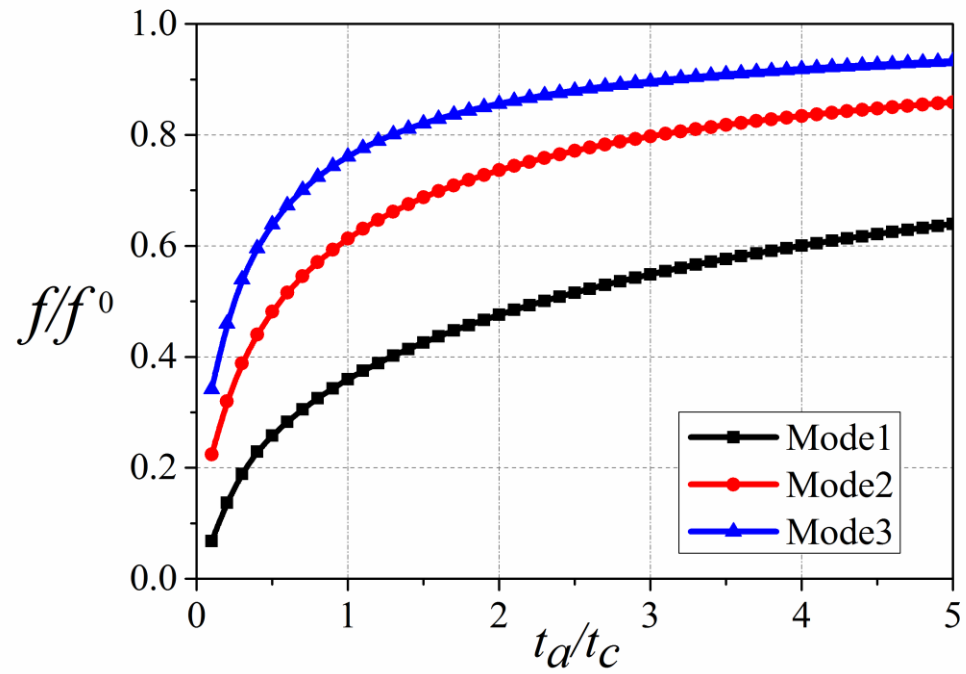

Figure 4.22 Influence of vibration mode: Sandwich panel B

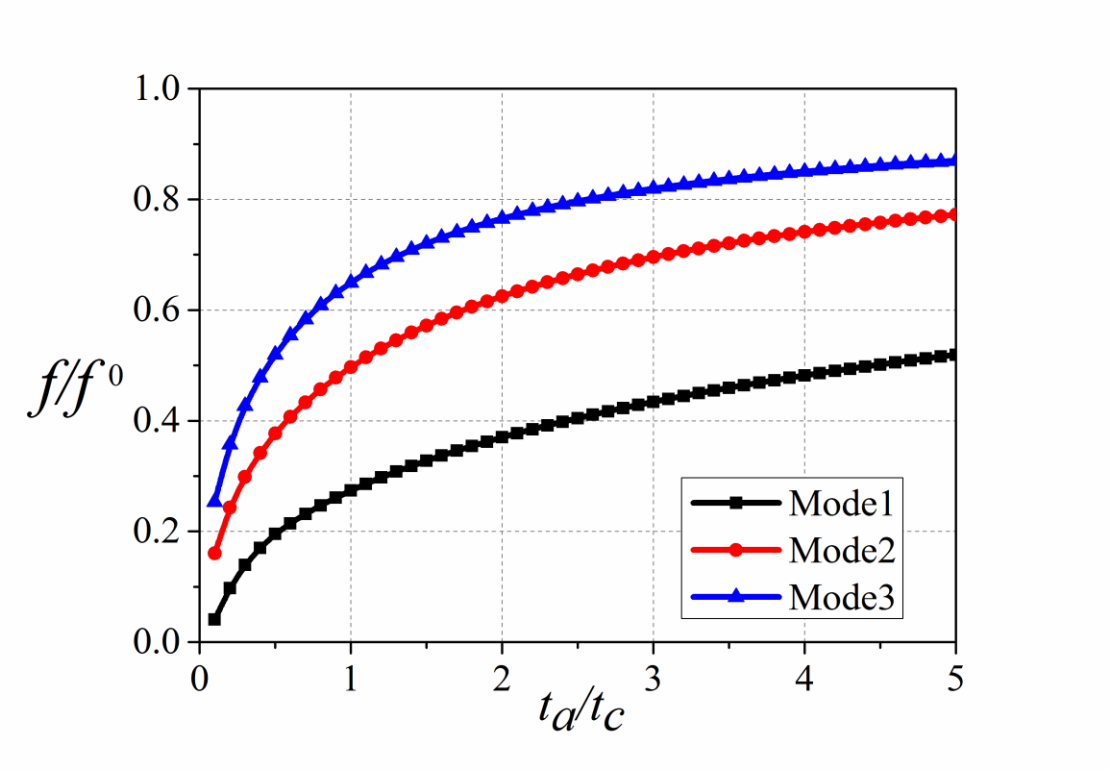

Figure 4.23 Influence of vibration mode: Sandwich panel C

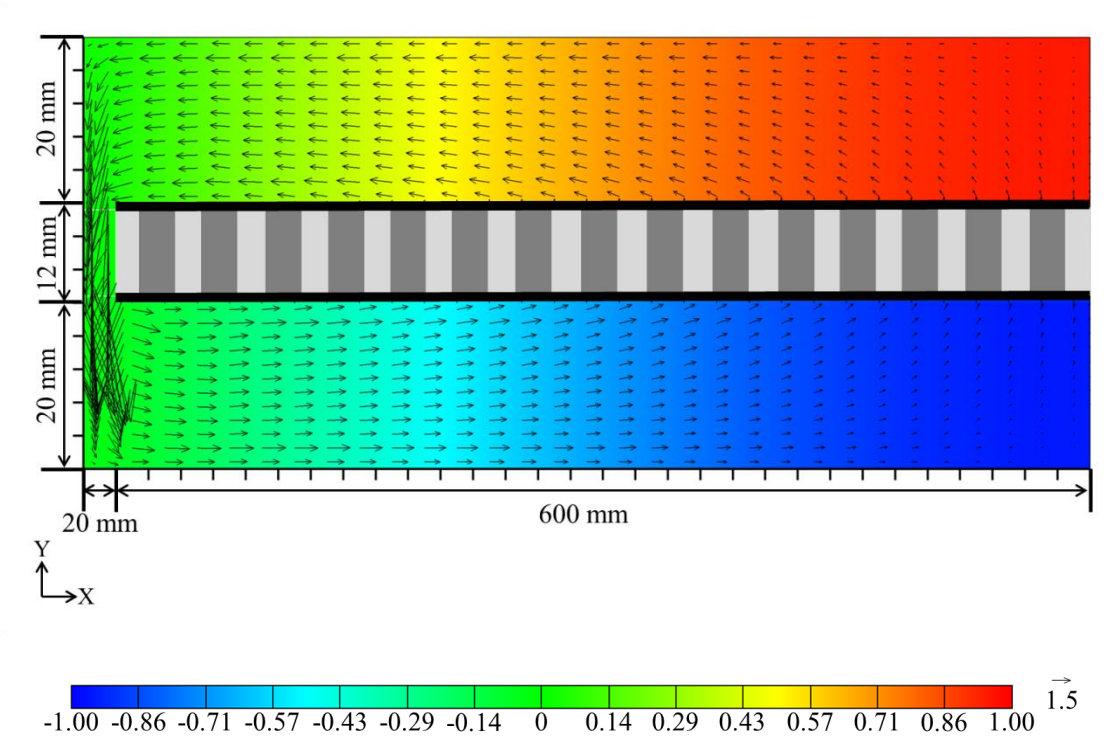

Figure 4.24 Air flow velocity vector and pressure distribution: Mode1

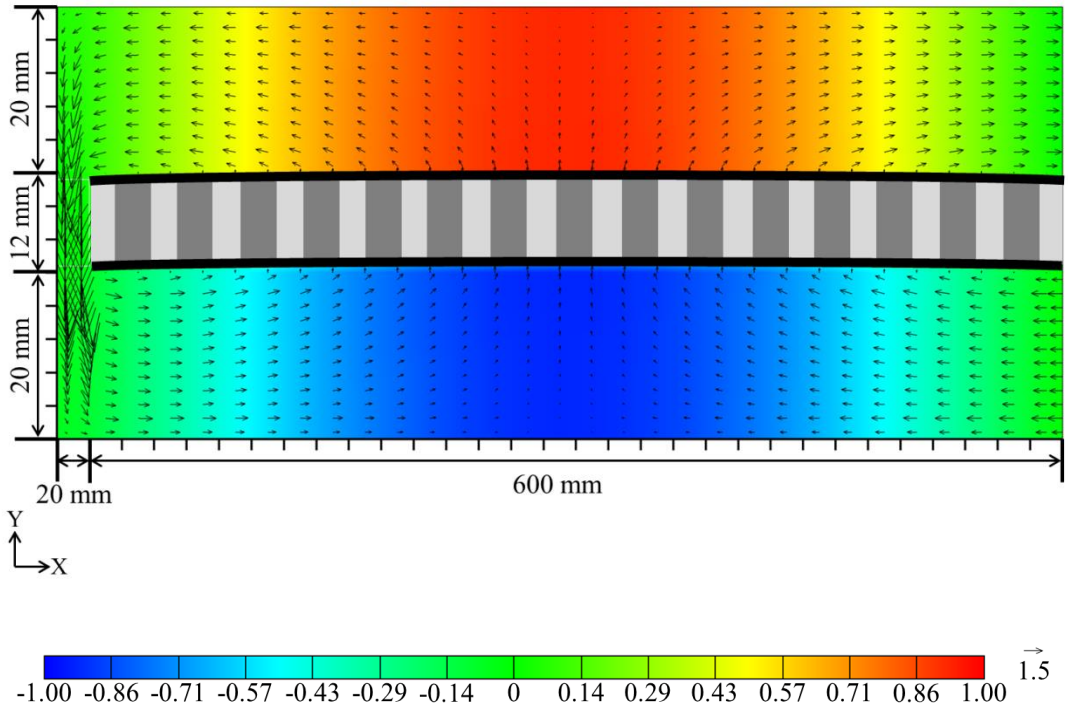

Figure 4.25 Air flow velocity vector and pressure distribution: Mode2

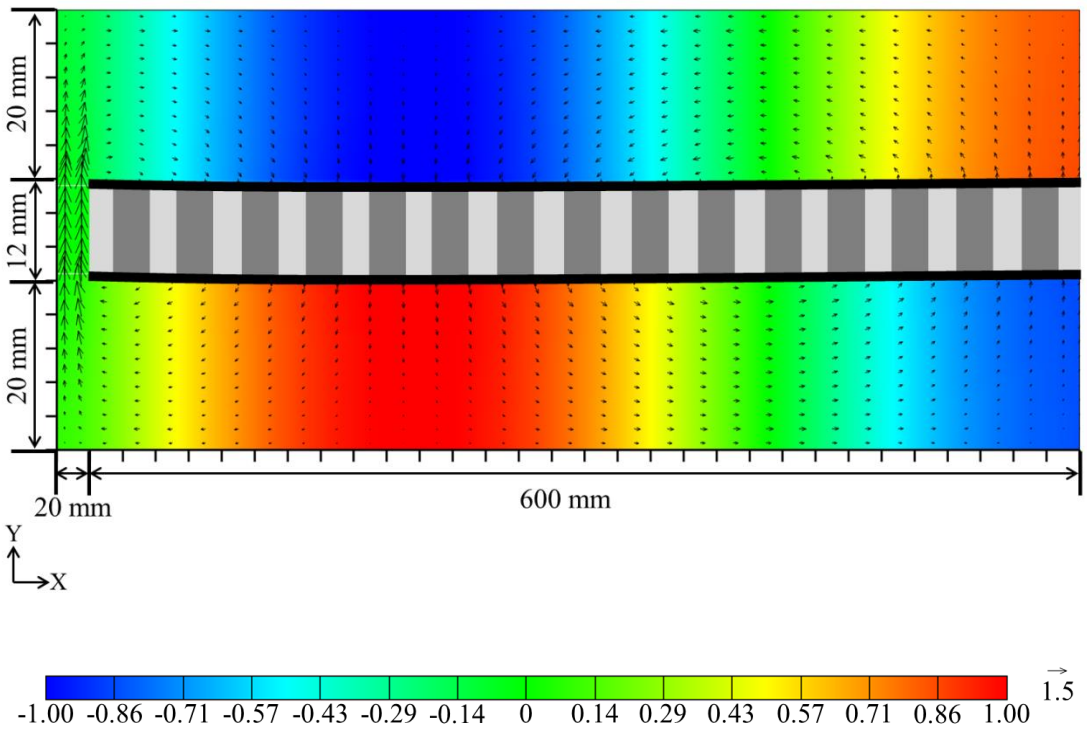

Figure 4.26 Air flow velocity vector and pressure distribution: Mode3

4.9 Influence of air viscosity

To clarify the influence of air viscosity, the first three natural frequencies obtained from the condition of considering and neglecting the air viscosity are compared as presented in **Figure 4.27**, **4.28**, and **4.29** for sandwich panel A, B, and C, respectively. For the condition of considering air viscosity (Standard μ), the air viscosity coefficient based on the normal temperature and pressure is employed. For the condition of neglecting air viscosity (10^{-5} μ), the viscosity coefficient is set to be 5-digit smaller than the standard value. The ordinate of **Figure 4.27-4.29** is identical to that of **Figure 4.11-4.15**. The abscissa is the air layer thickness (t_a). The comparison of natural frequencies neglecting and considering the air viscosity shows that the air viscosity effect is manifest in the case of thin air layer and the lower vibration mode. The results in **Figure 4.27-4.29** show good agreement with the results and suggestion of the Reference [27] that the viscous effect should be regarded for the condition of thin layer and low frequency.

To further explain these results, the characteristics of air flow velocity vector and pressure distribution are shown in **Figure 4.30**, **4.31**, and **4.32** for the air layer thickness of 1, 10, and 100 mm, respectively. In these characteristics, the panel vibrates in the fundamental mode and deforms upward. For the reason that both sides are symmetry, only the half left is presented. At the center of the panel, the flow vectors are directed vertically. Then they tend to change to horizontal direction and become larger when they approach the panel end. For the air layer thickness of 1 mm, the flow vectors appear as poiseuille flow as shown in **Figure 4.30(a)** due to the dominance of viscous effect**.** However, the viscous effect lessens when the air layer

thickness becomes larger. As presented in **Figure 4.31(a)** and **4.32(a)**, when the air layer thickness is 10 and 100 mm, the ratio of boundary layer occupying the air layer decreases as compared with the flow velocity profile of layer thickness of 1 mm shown in **Figure 4.30(a)**. In the case that the air viscosity coefficient is varied to be 5-digit smaller than the standard value, the air viscous effect also lessens as presented in **Figure 4.30(b)** and **4.31(b)** in which the boundary layer occupying the air layer is smaller than that of the standard condition. The comparison between **Figure 4.32(a)** and **4.32(b)** indicates that the viscous effect is very small in the case of thick air layer. As illustrated in **Figure 4.32,** the flow velocity profile and pressure magnitude of standard viscosity coefficient condition are quite identical to those of 5-digit smaller viscosity coefficient condition. By considering the pressure magnitude of each condition, the pressure magnitude in air layer increases when the air layer thickness decreases and/or the viscous effect increases. When the air layer thickness becomes thinner, the pressure magnitude of standard μ condition becomes higher than that of 10^{-5} μ condition. The difference of pressure magnitude increases corresponding to the difference of natural frequency shown in **Figure 4.27(b)**.

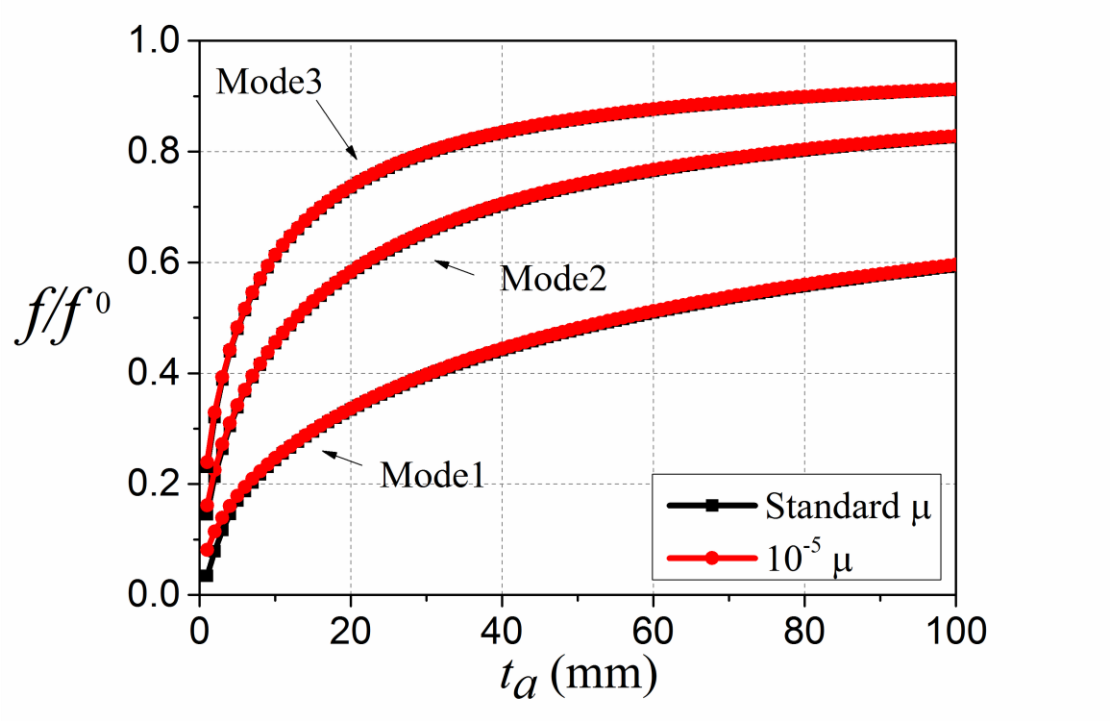

(a)

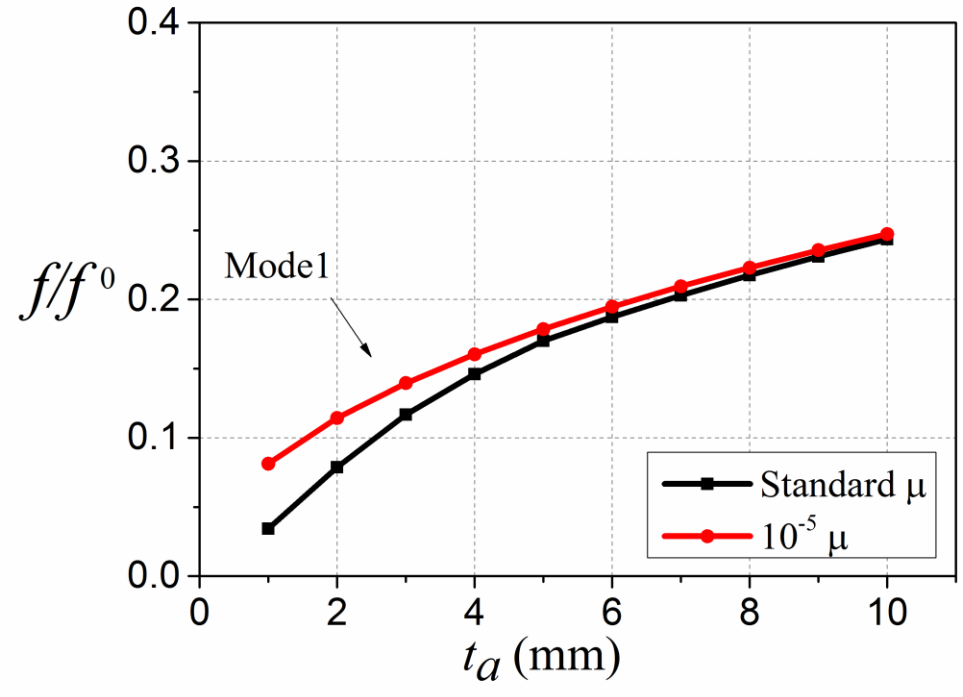

(b)

Figure 4.27 Influence of air viscosity: Sandwich panel A
(a) thick air layer **(b)** thin air layer

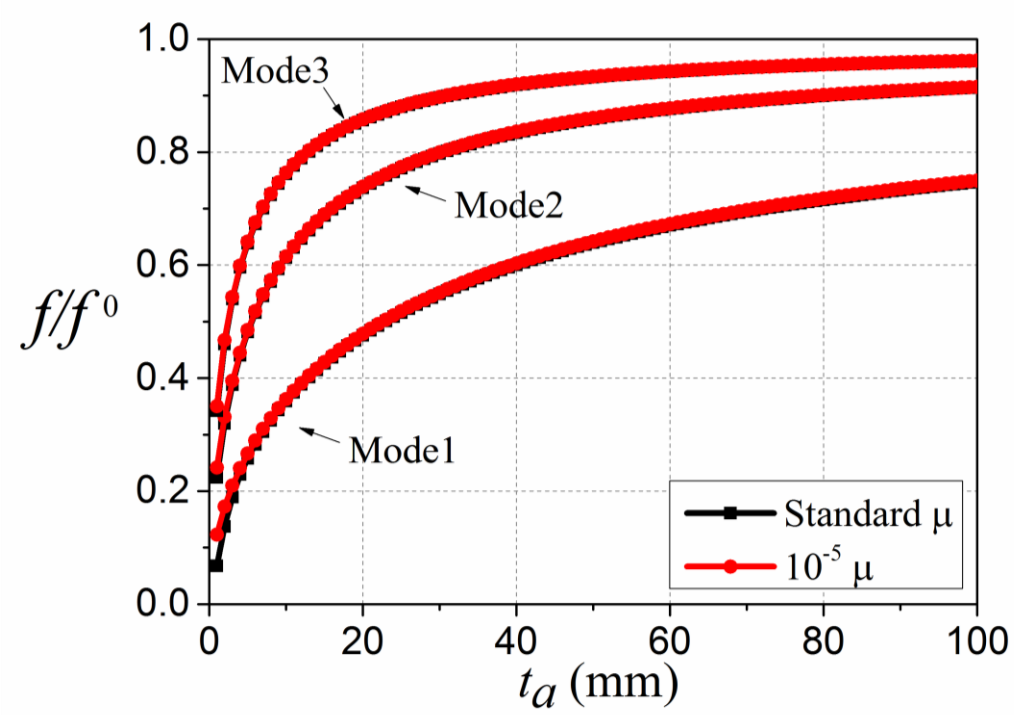

(a)

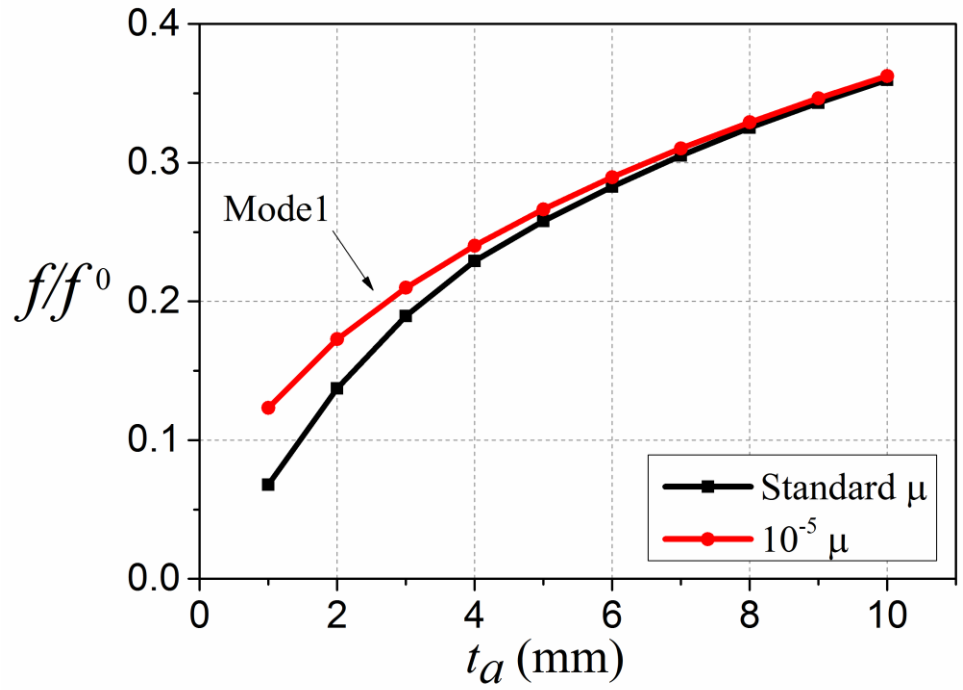

(b)

Figure 4.28 Influence of air viscosity: Sandwich panel B
(a) thick air layer **(b)** thin air layer

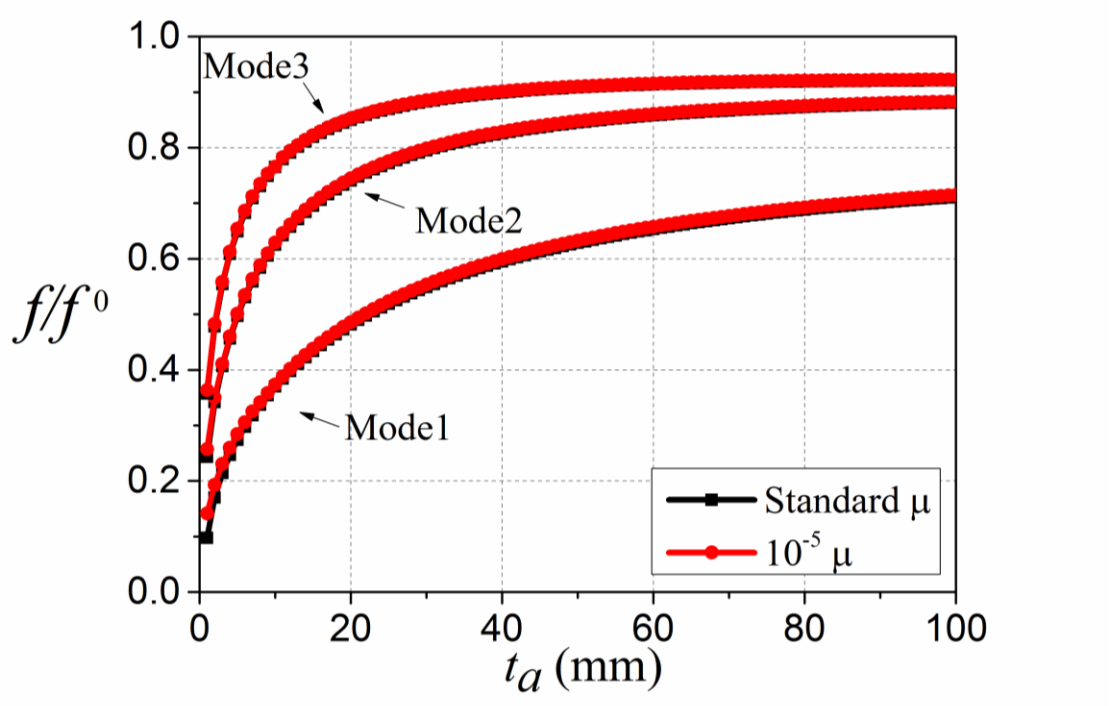

(a)

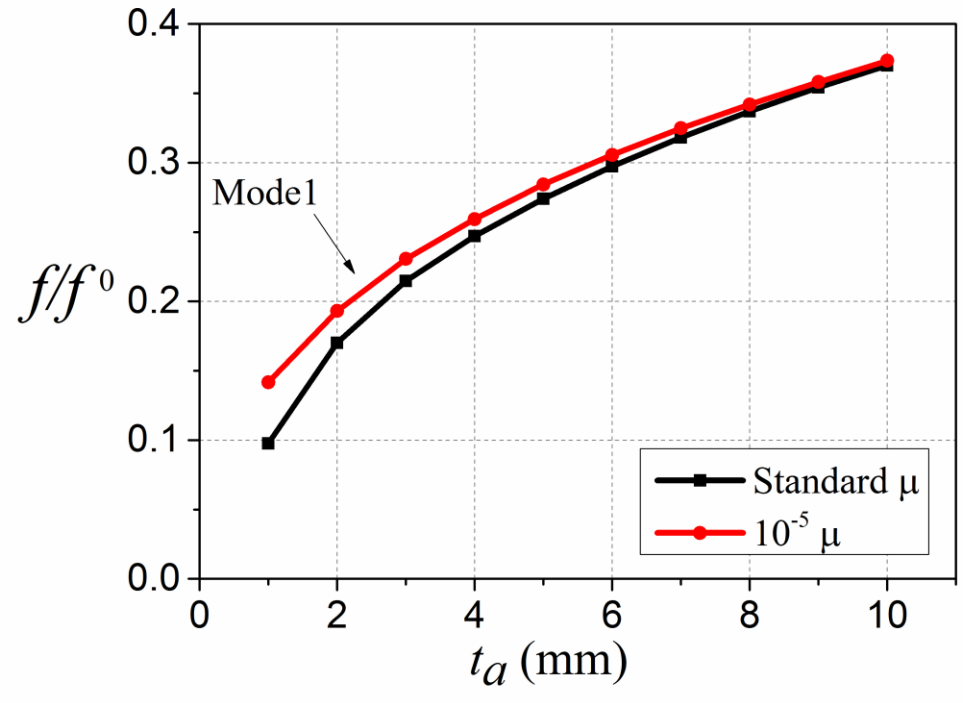

(b)

Figure 4.29 Influence of air viscosity: Sandwich panel C
(a) thick air layer **(b)** thin air layer

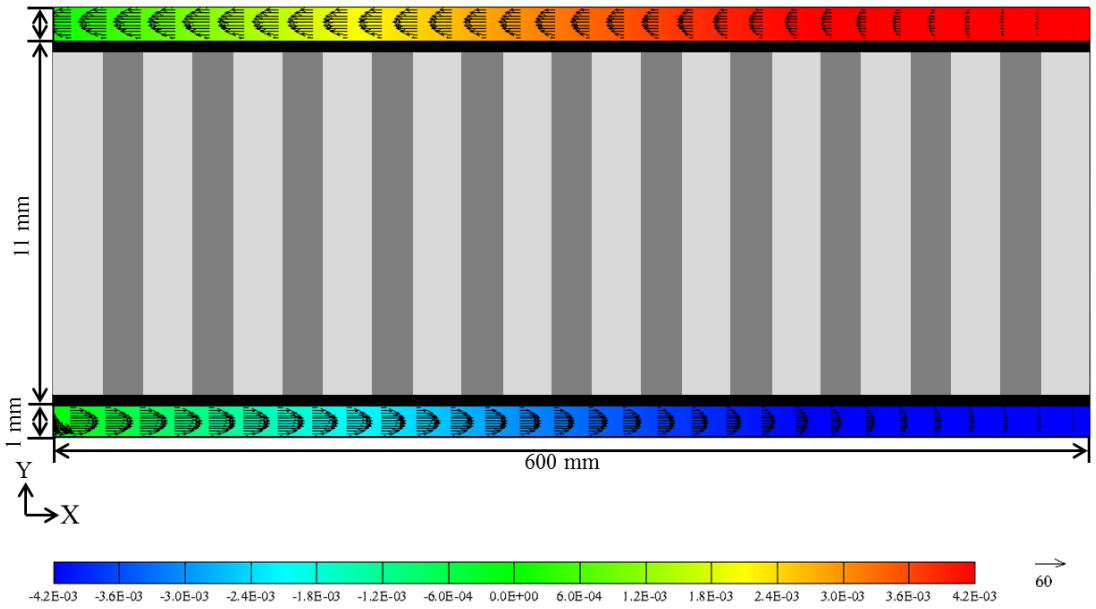

(a)

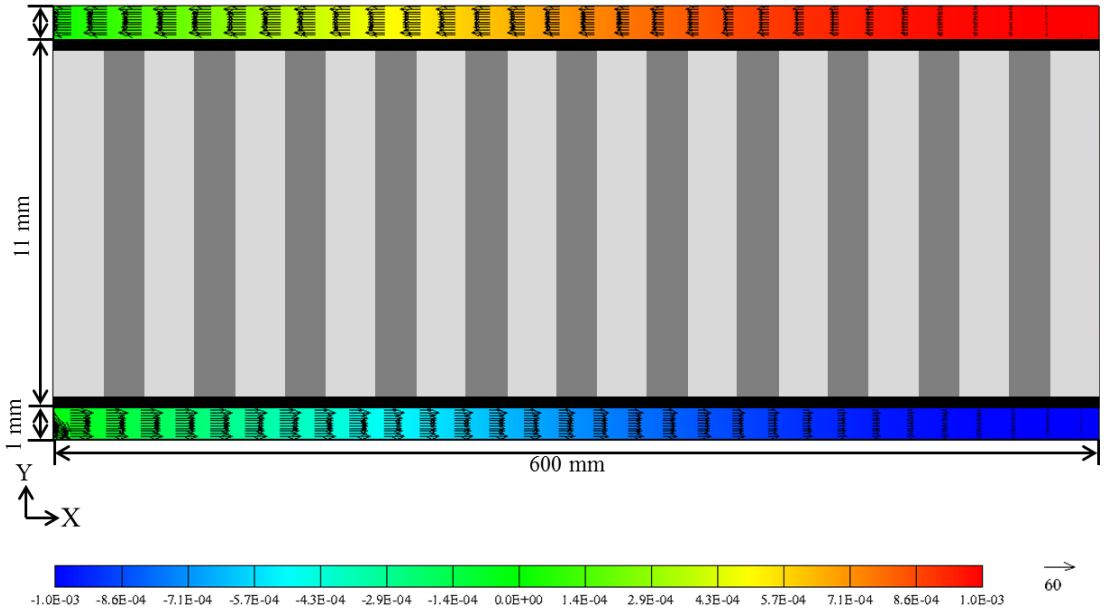

(b)

Figure 4.30 Air flow velocity vector and pressure distribution: air layer thickness of 1 mm **(a)** Standard μ **(b)** 10^{-5} μ

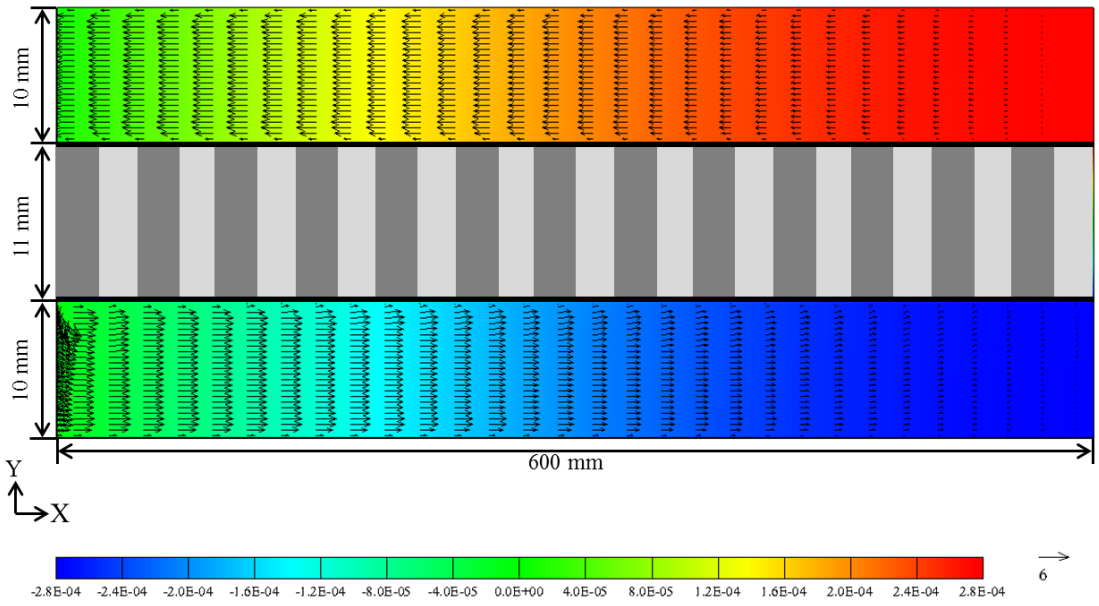

(a)

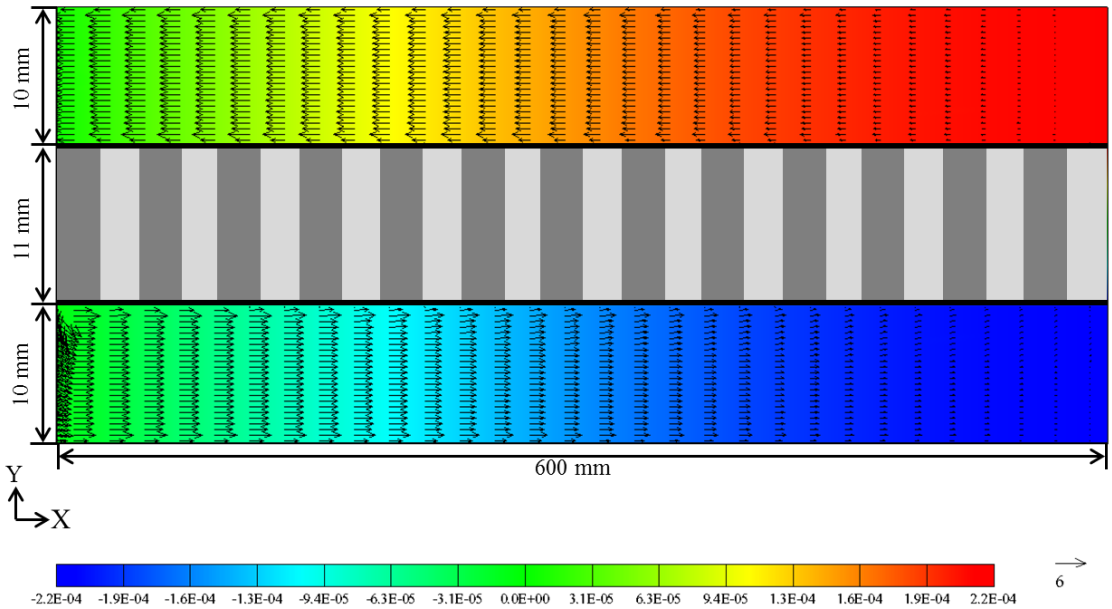

(b)

Figure 4.31 Air flow velocity vector and pressure distribution: air layer thickness of 10 mm **(a)** Standard μ **(b)** 10^{-5} μ

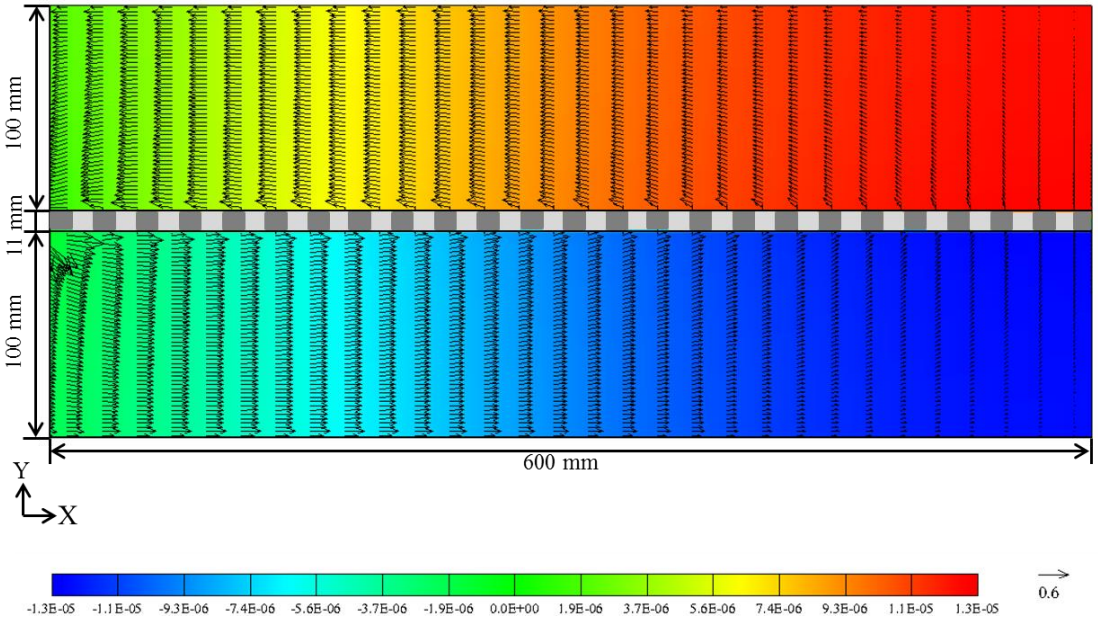

(a)

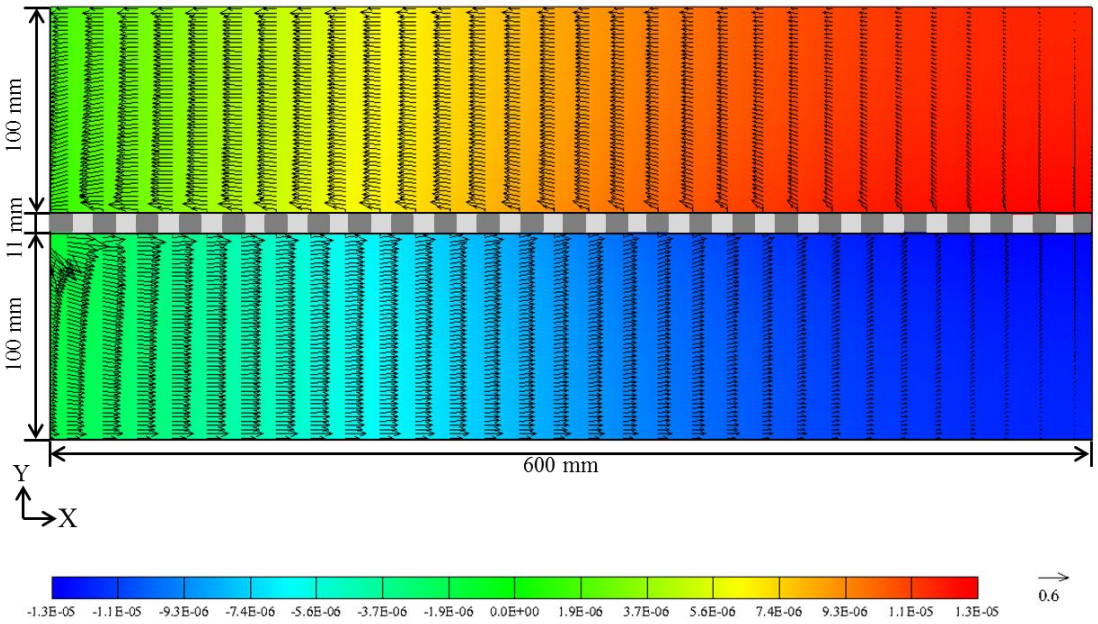

(b)

Figure 4.32 Air flow velocity vector and pressure distribution: air layer thickness of 100 mm **(a)** Standard μ **(b)** 10^{-5} μ

4.10 Influence of air density

To further proof the added mass effect on the decrease of natural frequency, the parametric study on the air density was conducted by varying the air density to be smaller than the standard value 1, 2, and 5-digit. The 1st mode natural frequency of sandwich panel A, B, and C is shown in **Figure 4.33**, **4.34**, and **4.35**, respectively. The ordinate and abscissa are still identical to those of **Figure 4.21-4.23**. The frequency variations of three sandwich panels are in same tendency. The results show that while the air density decreases, the frequency tends to shift up due to the diminution of added mass effect. As explained in the previous section, the oscillatory air flow affects the panel as an added mass resulting in the reduction of natural frequency. In the case that the density of air and sandwich panel is not much different, the added mass effect plays an important role affecting the dynamic behavior of the panel. On the contrary, the added mass effect has little effect. For instance, in the condition of 10^{-5} ρ_A, the normalized frequency is almost 1.0 meaning that there is small difference between the natural frequency including air effect and the natural frequency excluding air effect. The explanation of the added mass effect on the reduction of natural frequency was also verified by the results of this section.

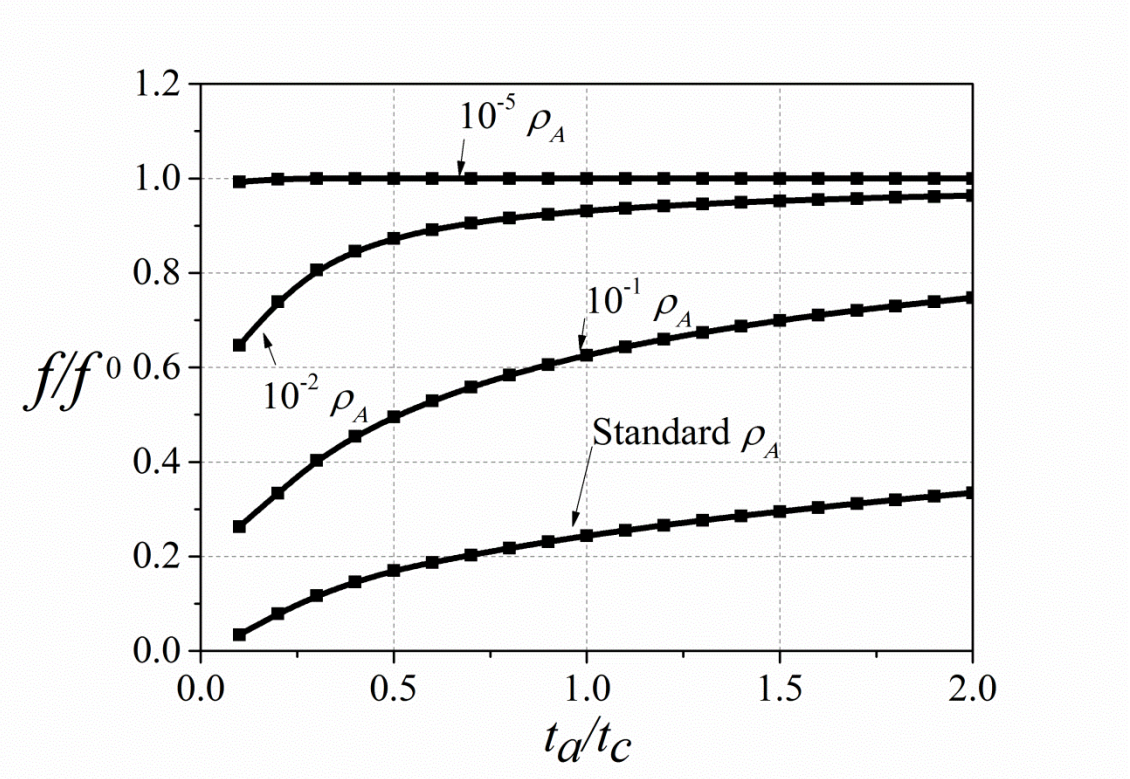

Figure 4.33 Influence of air density: Sandwich panel A

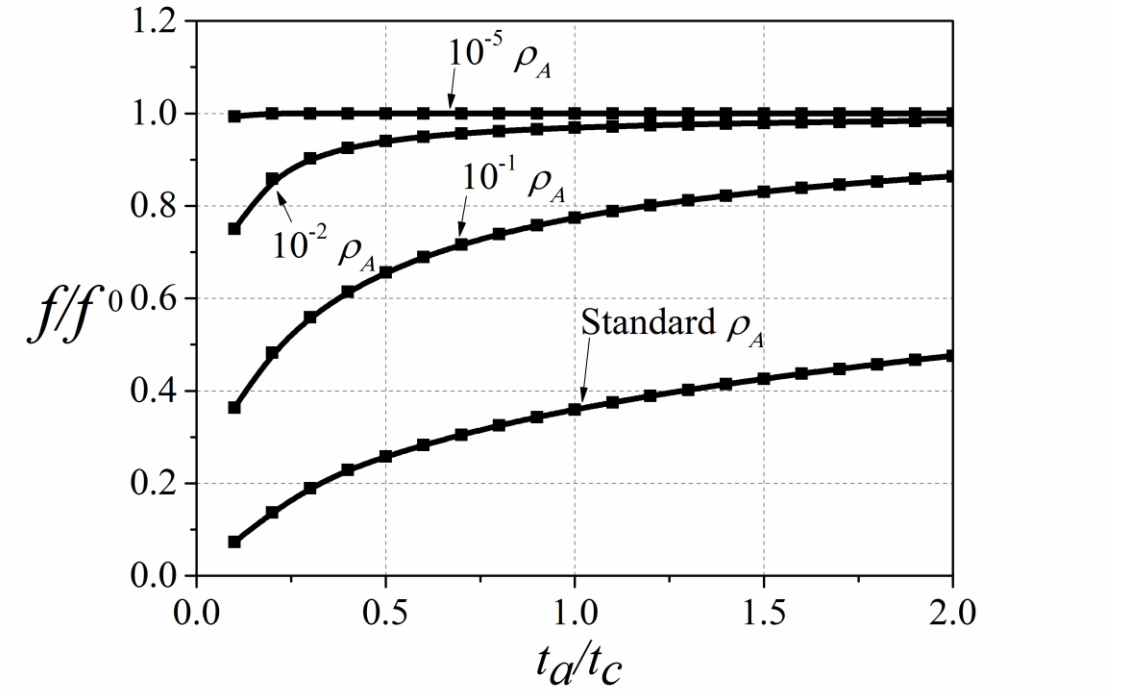

Figure 4.34 Influence of air density: Sandwich panel B

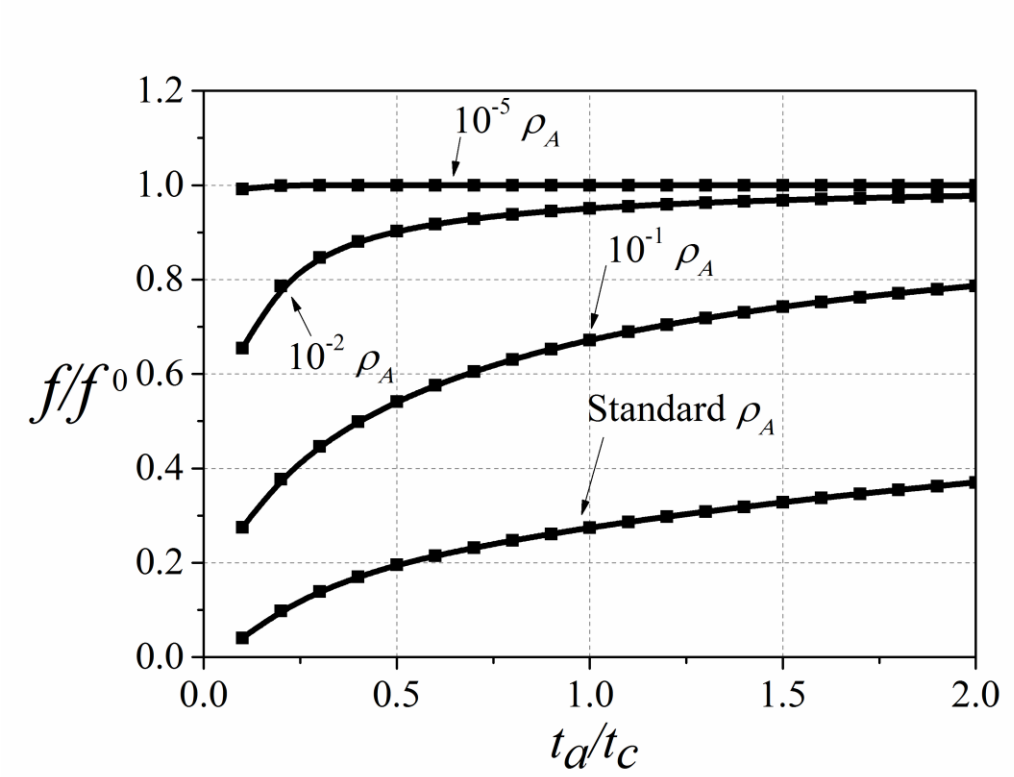

Figure 4.35 Influence of air density: Sandwich panel C

4.11 Influence of air-panel thickness

In the finite element analysis of a vibrating panel surrounded by thin air layers, the thickness of the panel should be included into the mesh model in order to obtain the accurate results. With the aim of understanding the accuracy improvement, the first three natural frequencies calculated by two mesh models, including and excluding the thickness of sandwich panel, were compared in the different air layer thicknesses of 2 mm, 10 mm, 100 mm, and infinite air domain. For the case of infinite air domain, the results from both models are almost same. For the other conditions, the natural frequencies calculated using the model including the panel thickness are always lower than those calculated using the model excluding the panel thickness. The reason is that when the sandwich panel thickness is included, the distance of

airflow increase thus resulting in the additional air mass. The difference between both results is presented in **Figure 4.36**, **4.37**, and **4.38** for 1st mode, 2nd mode, and 3rd mode, respectively. The abscissa is the panel thickness (t_b). The ordinate is the difference between both results. The difference becomes larger as the panel thickness increases and as the air layer thickness decreases. The results of three modes are similar in tendency but various in the difference. The difference decreases as the vibration mode order increases. In sum, the consideration of panel thickness is important for the case of thick panel coupled with thin air layer.

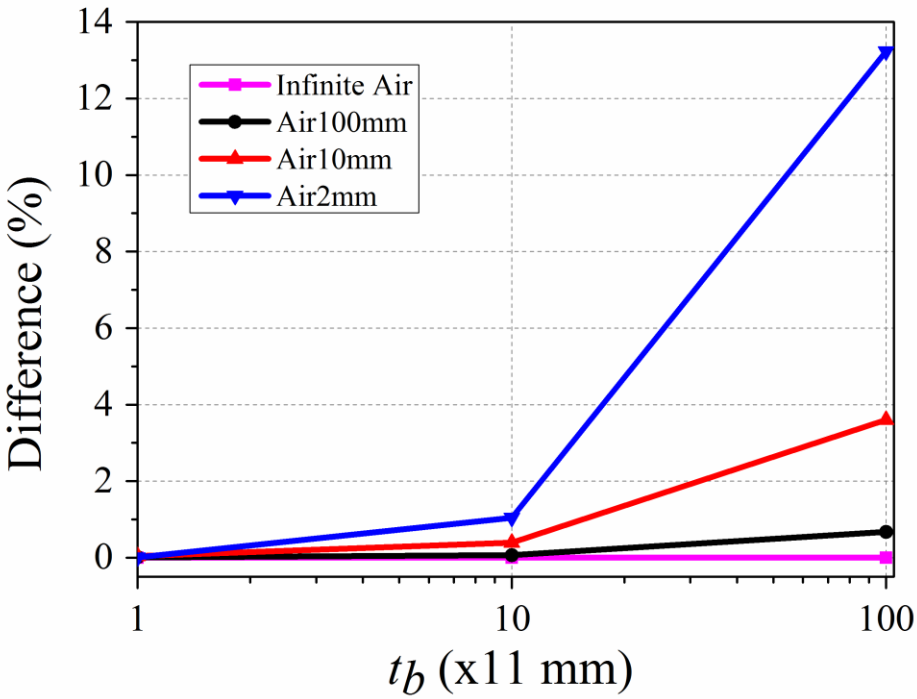

Figure 4.36 Influence of air-panel thickness: Mode1

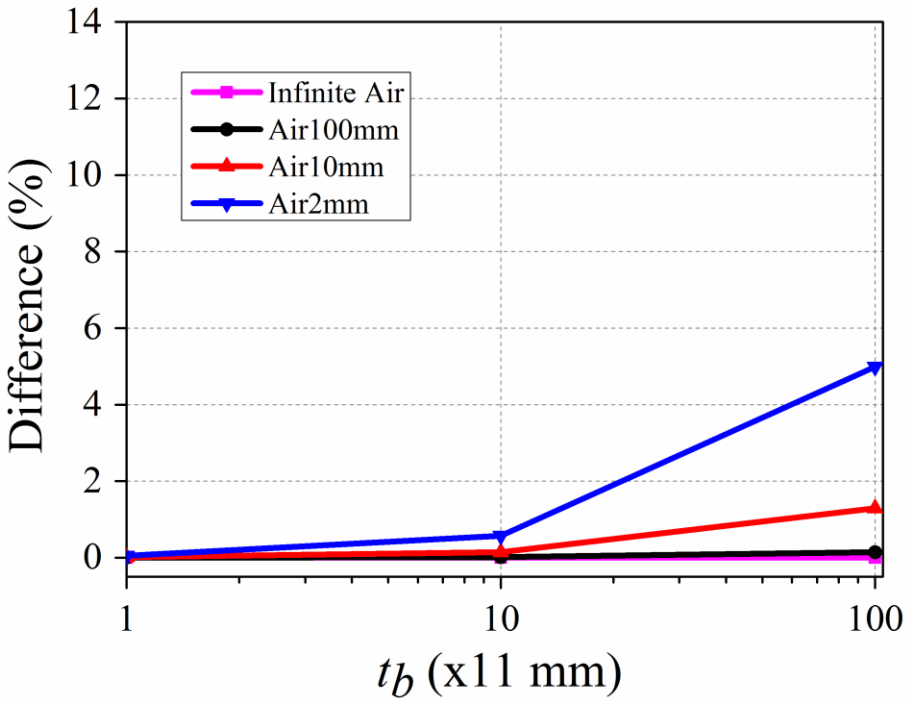

Figure 4.37 Influence of air-panel thickness: Mode2

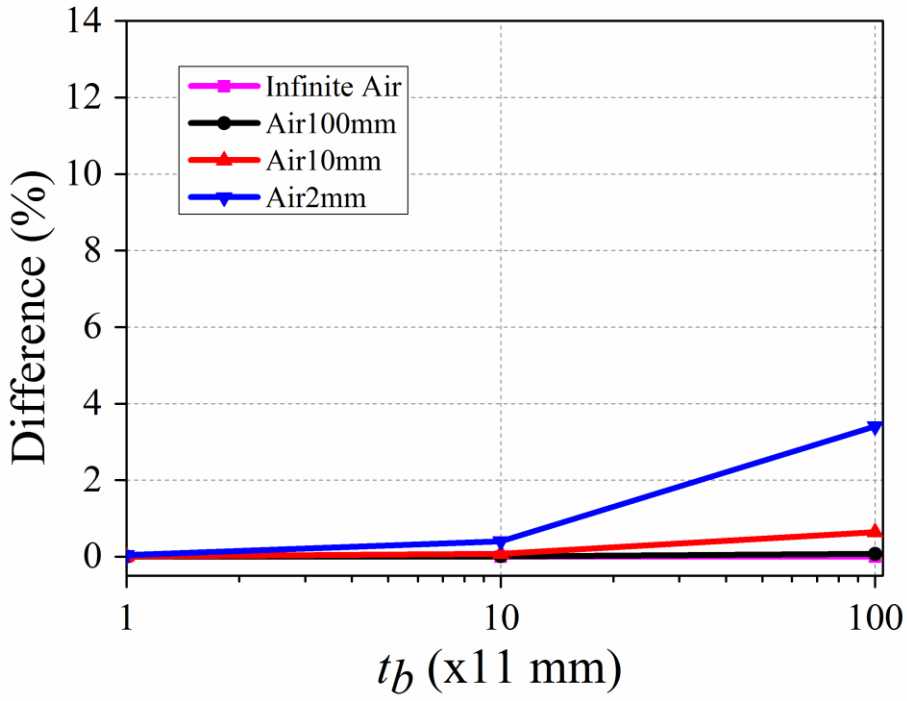

Figure 4.38 Influence of air-panel thickness: Mode3

Chapter 5
Conclusions and Recommendations

5.1 Conclusions

The fundamental natural frequency of a sandwich panel surrounded by air layers was investigated using experiment and numerical simulation. The experiment setup based on modal testing was proposed with the feature of simulating air layers around the sandwich panel. The numerical simulation was originally established for this study. The flexural motion of the sandwich structure was governed by a sixth order differential equation. The motion of the ambient air was governed by Navier-Stokes equations with viscous incompressible flow assumption and the penalty function formulation. The finite element equations of the panel and air were derived in weak form through the Galerkin weighted residual method and combined on the basis of a monolithic approach and eigenvalue problem. The finite element formulation was implemented in an in-house program operating on a Fortran 90 environment. The validation of the formulation was investigated by comparing the obtained results with other analytical solutions and experimental results. For the comparison with the analytical solution of Euler-Bernoulli and Sandwich theory, the results show good agreement with the sandwich theory solutions and indicate the necessity of considering the effect of shear deformation in sandwich core. The comparison between finite element and experimental results shows good concordance with difference less than 3%.

The parametric studies on the influences of shear deformation and ambient air on the natural frequencies were conducted. The achieved results can be concluded as follows:

- The effect of shear deformation causes the reduction in the natural frequencies. As the core shear stiffness weakens, the vibration mode order increases, and/or the sandwich panel thickens, the effect of shear deformation becomes stronger. For the bending vibration analysis of a weak core and/or thick sandwich panel, the effect of shear deformation is essential.
- The effect of air layer that surround the sandwich panel is sorted as an added mass effect and results in the reduction of the natural frequency.
- The air layer thickness is an influential factor. As the air layer thickness becomes thinner, the added mass effect is magnified and thus the natural frequency greatly decreases of more than 80% when the air layer thickness becomes thinner than 3 mm.
- The influence of panel length and mass density indicates the sensitive response on the natural frequency. However, the influence of panel bending stiffness is insignificant when compared with that of panel length and mass density.
- The magnitude of air effect becomes larger as the vibration mode order decreases. The effect of air viscosity is manifest in the case of thin layer and the lower vibration mode order. The inclusion of panel thickness into the finite element mesh model is important especially for the analysis of thick panel coupled with thin air layers.

5.2 Recommendations

Several recommendations for future researches as extension of this study are listed below:

- As explained in Chapter 2, the sandwich specimen was excited by an electromagnetic exciter via a stinger. This excitation method may affect the dynamic behavior of the sandwich panel as an added mass effect and result in the error between the experimental and simulation results. It is interesting to perform the experiment by using non-contact excitation methods, for instance magnetic excitation.
- It is interesting to perform the modal testing on a larger sandwich panel coupled with various condition of ambient air layer, so that the influence of ambient air on the natural frequencies and vibration modes can be fully described.
- More realistic 3-Dimensional finite element model can be developed to fully describe the influence of ambient air. However, to minimize the computation time and effort, 1/8 model can be employed by using the concept of ¼ model, given in Appendix C.
- Not only the influence of ambient air but also the effect of air trapped in sandwich core is significant. To achieve high-accuracy natural frequency, the influence of air trapped in sandwich core can be included into the analytical model.

References

[1] S.M. Hasheminejad, A. Shahsavarifard, M. Shahsavarifard, Dynamic Viscoelastic Effects on Free Vibrations of a Submerged Fluid-filled Thin Cylindrical Shell, J. Vib. Control. 14 (2008) 849–865. doi:10.1177/1077546307084442.

[2] J. Hohe, Effect of core and face sheet anisotropy on the natural frequencies of sandwich shells with composite faces, Int. J. Compos. Mater. 3 (2013) 40–52.

[3] F. Ebrahimi, N.F. nia, Thermo-mechanical vibration analysis of sandwich beams with functionally graded carbon nanotube-reinforced composite face sheets based on a higher-order shear deformation beam theory, Mech. Adv. Mater. Struct. 0 (2016) 1–37. doi:10.1080/15376494.2016.1196786.

[4] M.M. Alipour, An analytical approach for bending and stress analysis of cross/angle-ply laminated composite plates under arbitrary non-uniform loads and elastic foundations, Arch. Civ. Mech. Eng. 16 (2016) 193–210. doi:10.1016/j.acme.2015.11.001.

[5] M.M. Alipour, Effects of elastically restrained edges on FG sandwich annular plates by using a novel solution procedure based on layerwise formulation, Arch. Civ. Mech. Eng. 16 (2016) 678–694. doi:10.1016/j.acme.2016.04.015.

[6] Achilles Petras, Design of Sandwich Structures, Doctoral Thesis, Cambridge University, 1998.

[7] T.M. Carnahan, M.A. Kaiser, Coupled Facility-Payload Vibration Modeling Improvements, in: NAFEMS World Congr. 2015, San Diego, CA, United States, 2015: p. 10. http://ntrs.nasa.gov/search.jsp?R=20150023584 (accessed March 15, 2016).

[8] J. P. Den Hartog, Mechanical Vibrations, Dover Publications, United States, 1985.

[9] William T. Thomson, Marie Dillon Dahleh, Theory of Vibration with Applications, 5 edition, Prentice Hall, 1998.

[10] Benson H. Tongue, Principles of Vibration, 2nd ed., Oxford University Press, 2002.

[11] Y. Wu, S. Li, S. Liu, H.-S. Dou, Z. Qian, Vibration of Hydraulic Machinery, Springer Netherlands, Dordrecht, 2013. http://link.springer.com/10.1007/978-94-007-6422-4 (accessed November 2, 2015).

[12] G. Yuan, W.-K. Jiang, Vibration analysis of stiffened multi-plate structure based on a modified variational principle, J. Vib. Control. (2015) 1077546315621855. doi:10.1177/1077546315621855.

[13] S.M. Han, H. Benaroya, Nonlinear and Stochastic Dynamics of Compliant Offshore Structures, Springer Science & Business Media, 2013.

[14] J.W.S. Rayleigh, The theory of sound, London, Macmillan and co., 1877. http://archive.org/details/theorysound06raylgoog (accessed March 13, 2016).
[15] G. Chen, J. Zhou, Vibration and Damping in Distributed Systems, CRC Press, 1993.
[16] S.M. Han, H. Benaroya, T. Wei, Dynamics of transversely vibrating beams using four engineering theories, J. Sound Vib. 225 (1999) 935–988. doi:10.1006/jsvi.1999.2257.
[17] P.S.P. Timoshenko, On the transverse vibrations of bars of uniform cross-section, Philos. Mag. Ser. 6. 43 (1922) 125–131. doi:10.1080/14786442208633855.
[18] R.A. DiTaranto, Theory of Vibratory Bending for Elastic and Viscoelastic Layered Finite-Length Beams, J. Appl. Mech. 32 (1965) 881–886. doi:10.1115/1.3627330.
[19] D.J. Mead, S. Markus, The forced vibration of a three-layer, damped sandwich beam with arbitrary boundary conditions, J. Sound Vib. 10 (1969) 163–175. doi:10.1016/0022-460X(69)90193-X.
[20] D.J. Mead, A comparison of some equations for the flexural vibration of damped sandwich beams, J. Sound Vib. 83 (1982) 363–377. doi:10.1016/S0022-460X(82)80099-0.
[21] A.C. Nilsson, Wave propagation in and sound transmission through sandwich plates, J. Sound Vib. 138 (1990) 73–94. doi:10.1016/0022-460X(90)90705-5.
[22] D.K. Rao, Vibration of short sandwich beams, J. Sound Vib. 52 (1977) 253–263. doi:10.1016/0022-460X(77)90644-7.
[23] E. Nilsson, A.C. Nilsson, Prediction and measurement of some dynamic properties of sandwich structures with honeycomb and foam cores, J. Sound Vib. 251 (2002) 409–430. doi:10.1006/jsvi.2001.4007.
[24] D. Backström, A.C. Nilsson, Modelling the vibration of sandwich beams using frequency-dependent parameters, J. Sound Vib. 300 (2007) 589–611. doi:10.1016/j.jsv.2006.07.048.
[25] S. Cheng, P. Qiao, F. Chen, W. Fan, Z. Zhu, Free vibration analysis of fiber-reinforced polymer honeycomb sandwich beams with a refined sandwich beam theory, J. Sandw. Struct. Mater. (2015) 1099636215619841. doi:10.1177/1099636215619841.
[26] W.M. Beltman, P.J.M. van der Hoogt, R.M.E.J. Spiering, H. Tijdeman, Air loads on a rigid plate oscillating normall to a fixed surface, J. Sound Vib. 206 (1997) 217–242. doi:10.1006/jsvi.1997.1068.
[27] W.M. Beltman, P.J.M. van der Hoogt, R.M.E.J. Spiering, H. Tijdeman, Implementation and experimental validation of a new viscothermal acoustic finite element for acousto-elastic problems, J. Sound Vib. 216 (1998) 159–185. doi:10.1006/jsvi.1998.1708.

[28] M. Chimeno Manguán, E. Roibás Millán, J. López-Díez, F. Simón, Numerical modelling of structures with thin air layers, Aerosp. Sci. Technol. 38 (2014). doi:10.1016/j.ast.2014.07.008.
[29] M.J.H. Fox, P.N. Whitton, The damping of structural vibration by thin gas films, J. Sound Vib. 73 (1980) 279–295. doi:10.1016/0022-460X(80)90696-3.
[30] G.L. Ghiringhelli, M. Terraneo, E. Vigoni, Improvement of structures vibroacoustics by widespread embodiment of viscoelastic materials, Aerosp. Sci. Technol. 28 (2013) 227–241. doi:10.1016/j.ast.2012.11.003.
[31] Q.W. Liang, C.G. Rodríguez, E. Egusquiza, X. Escaler, M. Farhat, F. Avellan, Numerical simulation of fluid added mass effect on a francis turbine runner, Comput. Fluids. 36 (2007) 1106–1118. doi:10.1016/j.compfluid.2006.08.007.
[32] T. Önsay, Effects of layer thickness on the vibration response of a plate-fluid layer system, J. Sound Vib. 163 (1993) 231–259. doi:10.1006/jsvi.1993.1162.
[33] T. Önsay, Dynamic interactions between the bending vibrations of a plate and a fluid layer attenuator, J. Sound Vib. 178 (1994) 289–313. doi:10.1006/jsvi.1994.1487.
[34] C.A. Powell, D.G. Stephens, Vibrational characteristics of sandwich panels in a reduced-pressure environment, 1966. http://ntrs.nasa.gov/search.jsp?R=19660024166 (accessed March 15, 2016).
[35] C.A. Powell, D.G. Stephens, Vibration of sandwich panels in a vacuum, 1966. http://ntrs.nasa.gov/search.jsp?R=19680065641 (accessed March 15, 2016).
[36] M.A. Scavullo, D.G. Stephens, Investigation of air damping of circular and rectangular plates, a cylinder, and a sphere, 1965. http://ntrs.nasa.gov/search.jsp?R=19650010805 (accessed March 15, 2016).
[37] C.A. Tan, C.D. Mote Jr, Pressure and flow in fluid films constrained between translating and vibrating flexible surfaces, Int. J. Eng. Sci. 29 (1991) 1609–1625. doi:10.1016/0020-7225(91)90131-L.
[38] T.T. Yeh, S.S. Chen, The effect of fluid viscosity on coupled tube/fluid vibrations, J. Sound Vib. 59 (1978) 453–467. doi:10.1016/S0022-460X(78)80010-8.
[39] Anders Nilsson, Bilong Liu, Vibro-Acoustics,Volume 2, Second Edition, Springer-Verlag Berlin Heidelberg, 2015. https://www.springer.com/jp/book/9783662479339 (accessed November 11, 2015).
[40] J.C. Heinrich, B.R. Dyne, On the Penalty Method for Incompressible Fluids, in: E. Oñate, J. Periaux, A. Samuelsson (Eds.), Finite Elem. Method 1990's, Springer Berlin Heidelberg, 1991: pp. 465–476. http://link.springer.com/chapter/10.1007/978-3-662-10326-5_46 (accessed December 11, 2014).

[41] T.J.R. Hughes, W.K. Liu, A. Brooks, Finite element analysis of incompressible viscous flows by the penalty function formulation, J. Comput. Phys. 30 (1979) 1–60. doi:10.1016/0021-9991(79)90086-X.

[42] R.M.S.M. Schulkes, Interactions of an elastic solid with a viscous fluid: Eigenmode analysis, J. Comput. Phys. 100 (1992) 270–283. doi:10.1016/0021-9991(92)90234-P.

[43] R.S. Martin, J.H. Wilkinson, Similarity Reduction of a General Matrix to Hessenberg Form, in: P.D.F.L. Bauer (Ed.), Linear Algebra, Springer Berlin Heidelberg, 1971: pp. 339–358. http://link.springer.com/chapter/10.1007/978-3-662-39778-7_24 (accessed February 27, 2015).

[44] B.N. Parlett, C. Reinsch, Balancing a Matrix for Calculation of Eigenvalues and Eigenvectors, in: P.D.F.L. Bauer (Ed.), Linear Algebra, Springer Berlin Heidelberg, 1971: pp. 315–326. http://link.springer.com/chapter/10.1007/978-3-662-39778-7_22 (accessed February 27, 2015).

[45] G. Peters, J.H. Wilkinson, Eigenvectors of Real and Complex Matrices by LR and QR triangularizations, in: P.D.F.L. Bauer (Ed.), Linear Algebra, Springer Berlin Heidelberg, 1971: pp. 372–395. http://link.springer.com/chapter/10.1007/978-3-662-39778-7_26 (accessed February 27, 2015).

[46] E.P.D. of A.M.U. Grenander, U. Grenander, Mathematical experiments on the computer, Academic Press, 1982.

[47] K.J. Bathe, Finite Element Procedures, Klaus-Jurgen Bathe, Boston, Mass., 2007.

[48] H.C. Elman, D.J. Silvester, A.J. Wathen, Finite Elements and Fast Iterative Solvers: with Applications in Incompressible Fluid Dynamics, Oxford University Press, Oxford, 2005.

[49] P.M. Gresho, R.L. Sani, Incompressible Flow and the Finite Element Method, Volume 2, Isothermal Laminar Flow, 1 edition, Wiley, Chichester, 2000.

[50] D.N. Arnold, D. Boffi, R.S. Falk, Approximation by quadrilateral finite elements, Math. Comput. 71 (2002) 909–922. doi:10.1090/S0025-5718-02-01439-4.

[51] M. Fortin, Old and new finite elements for incompressible flows, Int. J. Numer. Methods Fluids. 1 (1981) 347–364. doi:10.1002/fld.1650010406.

[52] A. Pereira, C. Talischi, G.H. Paulino, I.F.M. Menezes, M.S. Carvalho, Fluid flow topology optimization in PolyTop: stability and computational implementation, Struct. Multidiscip. Optim. 54 (2016) 1345–1364. doi:10.1007/s00158-014-1182-z.

[53] M. Razzaq, Finite element simulation techniques for incompressible fluid structure interaction with applications to bioengineering and optimization (PDF Download Available), Technische Universität Dortmund, 2011.

[54] J.N. Reddy, D.K. Gartling, The Finite Element Method in Heat Transfer and Fluid Dynamics, Third Edition, 3 edition, CRC Press, Boca Raton, Fla., 2010.
[55] H.R. Öz, Calculation of the Natural Frequencies of a Beam–Mass System Using Finite Element Method, Math. Comput. Appl. 5 (2000) 67–76. doi:10.3390/mca5020067.

Appendix A
Derivation for the element coupling interface matrices $[G_B^e]$ $[G_{\bar{A}}^e]$

Starting from the boundary integral term in Equation (3.11) and concerning the continuity condition of the stress components through the discrete boundary of the coupling interface G^e in Equation (3.7), it becomes

$$\begin{aligned}
&\int_{\Omega_1^e} \lfloor N_d \rfloor^T \left((D_B + 2D_f) \frac{\partial^2 \left(\nabla \cdot \sigma_{B_{ij}} \right)}{\partial x^2} - G_c b t_c \left(\nabla \cdot \sigma_{B_{ij}} \right) \right) d\Omega_1^e \\
&= \int_{G^e} \lfloor N_d \rfloor^T \left((D_B + 2D_f) \frac{\partial^2 \sigma_{B_n}}{\partial x^2} - G_c b t_c \sigma_{B_n} \right) dG^e \\
&= \int_{G^e} \lfloor N_d \rfloor^T \left(G_c b t_c \sigma_{n_A} - (D_B + 2D_f) \frac{\partial^2 \sigma_{A_n}}{\partial x^2} \right) dG^e
\end{aligned} \tag{A1}$$

From Equation (3.5) and (3.6), the discrete stress components defined for each of finite elements are expressed as

$$\begin{aligned}
\sigma_{n_A} &= \frac{1}{\varepsilon_p} \left(\frac{\partial u}{\partial x} + \frac{\partial v}{\partial y} \right) + 2\mu \frac{\partial v}{\partial y} \\
&= \frac{1}{\varepsilon_p} \left(\frac{\partial \lfloor N_u \rfloor}{\partial x} \{u^e\} + \frac{\partial \lfloor N_u \rfloor}{\partial y} \{v^e\} \right) + 2\mu \frac{\partial \lfloor N_u \rfloor}{\partial y} \{v^e\} \\
&= \frac{1}{\varepsilon_p} \left\lfloor \frac{\partial N_u}{\partial x} \quad \frac{\partial N_u}{\partial y} \right\rfloor \cdot \{\boldsymbol{u}^e\} + 2\mu \left\lfloor 0 \quad \frac{\partial N_u}{\partial y} \right\rfloor \cdot \{\boldsymbol{u}^e\}
\end{aligned} \tag{A2}$$

$$\begin{aligned}
\sigma_{\tau_A} &= \mu \left(\frac{\partial u}{\partial y} + \frac{\partial v}{\partial x} \right) \\
&= \mu \left(\frac{\partial \lfloor N_u \rfloor}{\partial y} \{u^e\} + \frac{\partial \lfloor N_u \rfloor}{\partial x} \{v^e\} \right) \\
&= \mu \left\lfloor \frac{\partial N_u}{\partial y} \quad \frac{\partial N_u}{\partial x} \right\rfloor \cdot \{\boldsymbol{u}^e\}
\end{aligned} \tag{A3}$$

Substituting Equation (A2) for Equation (A1), we obtain the element coupling

interface matrix of the panel

$$\begin{aligned}
&\int_{G^e}\lfloor N_d \rfloor^T\left(G_c b t_c \sigma_{A_n} - (D_B + 2D_f)\frac{\partial^2 \sigma_{A_n}}{\partial x^2}\right) dG^e \\
&\quad = G_c b t_c \frac{1}{\varepsilon_p}\int_{G^e}\lfloor N_d \rfloor^T \cdot \left\lfloor \frac{\partial N_u}{\partial x} \quad \frac{\partial N_u}{\partial y}\right\rfloor \cdot \{\boldsymbol{u}^e\} dG^e \\
&\qquad - 2G_c b t_c \mu \int_{G^e}\lfloor N_d \rfloor^T \cdot \left\lfloor 0 \quad \frac{\partial N_u}{\partial y}\right\rfloor \cdot \{\boldsymbol{u}^e\} dG^e \\
&\qquad\quad - (D_B + 2D_f)\frac{1}{\varepsilon_p}\int_{G^e}\left\lfloor \frac{\partial^2 N_d}{\partial x^2}\right\rfloor^T \cdot \left\lfloor \frac{\partial N_u}{\partial x} \quad \frac{\partial N_u}{\partial y}\right\rfloor \cdot \{\boldsymbol{u}^e\} dG^e \\
&\qquad\quad + 2(D_B + 2D_f)\mu \int_{G^e}\left\lfloor \frac{\partial^2 N_d}{\partial x^2}\right\rfloor^T \cdot \left\lfloor 0 \quad \frac{\partial N_u}{\partial y}\right\rfloor \cdot \{\boldsymbol{u}^e\} dG^e \\
&\quad = \left[G_B^e\right] \cdot \{\boldsymbol{u}^e\}
\end{aligned} \tag{A4}$$

From the last term in Equation (3.15), concerning the no slip condition, on the discrete boundary of the rigid wall, it becomes

$$-\int_{S_A^e = G^e + W^e}\left(\lfloor N_u \rfloor_n^T \cdot \sigma_{A_n} + \lfloor N_u \rfloor_\tau^T \cdot \sigma_{A_\tau}\right) dS_A^e = -\int_{G^e}\left(\lfloor N_u \rfloor_n^T \cdot \sigma_{A_n} + \lfloor N_u \rfloor_\tau^T \cdot \sigma_{A_\tau}\right) dG^e \tag{A5}$$

Also $\lfloor N_u \rfloor_n$ and $\lfloor N_u \rfloor_\tau$, which denote the normal and tangent components of the shape function matrix $\lfloor N_u \rfloor$ are expressed as

$$\begin{aligned}
&\lfloor N_u \rfloor_n = \lfloor 0 \quad N_u \rfloor \\
&\lfloor N_u \rfloor_\tau = \lfloor N_u \quad 0 \rfloor
\end{aligned} \tag{A6}$$

Substituting Equation (A2), (A3), and (A6) into Equation (A5)

$$\begin{aligned}
&-\int_{G^e}\left(\lfloor N_u \rfloor_n^T \cdot \sigma_{A_n} + \lfloor N_u \rfloor_\tau^T \cdot \sigma_{A_\tau}\right) dG^e \\
&\quad = -\frac{1}{\varepsilon_p}\int_{G^e}\lfloor 0 \quad N_u \rfloor^T \cdot \left\lfloor \frac{\partial N_u}{\partial x} \quad \frac{\partial N_u}{\partial y}\right\rfloor \cdot \{\boldsymbol{u}^e\} dG^e \\
&\qquad - 2\mu \int_{G^e}\lfloor 0 \quad N_u \rfloor^T \cdot \left\lfloor 0 \quad \frac{\partial N_u}{\partial y}\right\rfloor \cdot \{\boldsymbol{u}^e\} dG^e \\
&\qquad\quad - \mu \int_{G^e}\lfloor N_u \quad 0 \rfloor^T \cdot \left\lfloor \frac{\partial N_u}{\partial y} \quad \frac{\partial N_u}{\partial x}\right\rfloor \cdot \{\boldsymbol{u}^e\} dG^e \\
&\quad = -\left[G_A^e\right] \cdot \{\boldsymbol{u}^e\}
\end{aligned} \tag{A7}$$

Appendix B
Free vibration analysis of damped system

Generally, the results obtained from an eigenvalue analysis are an eigenvalue (λ) and eigenvector ($\boldsymbol{z}$). The vibration can be expressed as a function of time $f(t)$

$$f(t) = e^{\lambda t}\boldsymbol{z} + e^{\bar{\lambda} t}\bar{\boldsymbol{z}} \tag{B1}$$

Here, $\bar{\lambda}$ is the complex conjugate of the eigenvalue (λ) and $\bar{z}$ is the complex conjugate of the eigenvector ($\boldsymbol{z}$).

Since the panel vibrating in air is considered as a damped system, both eigenvalue and eigenvector are the complex quantities, which can be expressed as follows:

$$\lambda = -\alpha + i\beta \tag{B2}$$

$$\boldsymbol{z} = \boldsymbol{x} + i\boldsymbol{y} \tag{B3}$$

Substituting Equation (B2) and (B3) into (B1), $f(t)$ is expressed as follows:

$$f(t) = 2e^{-\alpha t}\left(\boldsymbol{x}\cdot\cos\beta t - \boldsymbol{y}\cdot\sin\beta t\right) \tag{B4}$$

$$f(t) = 2e^{-\gamma\omega_0 t}\left(\boldsymbol{x}\cdot\cos\omega_0\sqrt{1-\gamma^2}t - \boldsymbol{y}\cdot\sin\omega_0\sqrt{1-\gamma^2}t\right) \tag{B5}$$

where

$$\omega_0 = \sqrt{\alpha^2+\beta^2} \tag{B6}$$

$$\gamma = \frac{\alpha}{\sqrt{\alpha^2+\beta^2}} \tag{B7}$$

The physical meaning of Equation (B5) can explained as follows:

$2e^{-\gamma\omega_0 t}$ represents the amplitude of vibration, $\left(\boldsymbol{x}\cdot\cos\omega_0\sqrt{1-\gamma^2}t - \boldsymbol{y}\cdot\sin\omega_0\sqrt{1-\gamma^2}t\right)$ is the

sinusoidal vibration, ω_0 is the natural frequency without damping, γ $(0<\gamma<1)$ is the damping coefficient ratio served as an indicator of the effect of damping term.

Appendix C
Modelling of quarter model

C.1 ½ Model

For the consideration of ½ model, the geometry and restraints of mesh models as shown in **Figure 3.4** and **3.5** are symmetric between left- and right-half. **Figure C.1** shows the sketch of a vibrating panel coupled with ambient air on the 1st mode (odd mode), in which the dash line represents the symmetrical edge and the displacement of the panel and air velocity vectors are symmetric. The symmetry displacement condition is given that in the symmetrical edge, the rotation of the panel and the air velocity in X-direction equal to zero. **Figure C.2** illustrates the sketch of a vibrating panel coupled with ambient air on the 2nd mode (even mode), in which the displacement of the panel and air velocity vectors are anti-symmetric and the dash line is the edge of anti-symmetry. The lateral displacement of panel and the air velocity in Y-direction equal to zero at the edge of anti-symmetry. For the condition of odd mode and even mode, the ½ model can be applied by considering only half-left.

C.2 ¼ model

To apply for ¼ model, the anti-symmetry condition between upper and lower part of the ½ model is considered. **Figure C.3** and **C.4** present the left half of the sketch of a vibrating panel coupled with ambient air on the 1^{st} and 2^{nd} mode,

respectively. From **Figure C.4** and **C.5**, as the panel displaces upward, the air flows downward. The air velocity in upper and lower part is reverse in X-direction. The relation of air velocity in upper and lower-part can be concluded as follows:

$$u_U = -u_L \tag{C1}$$

$$v_U = v_L \tag{C2}$$

Here, u_U and v_U are the air velocity of upper part in X- and Y-direction, respectively. u_L and v_L are the air velocity of lower part in X- and Y-direction, respectively.

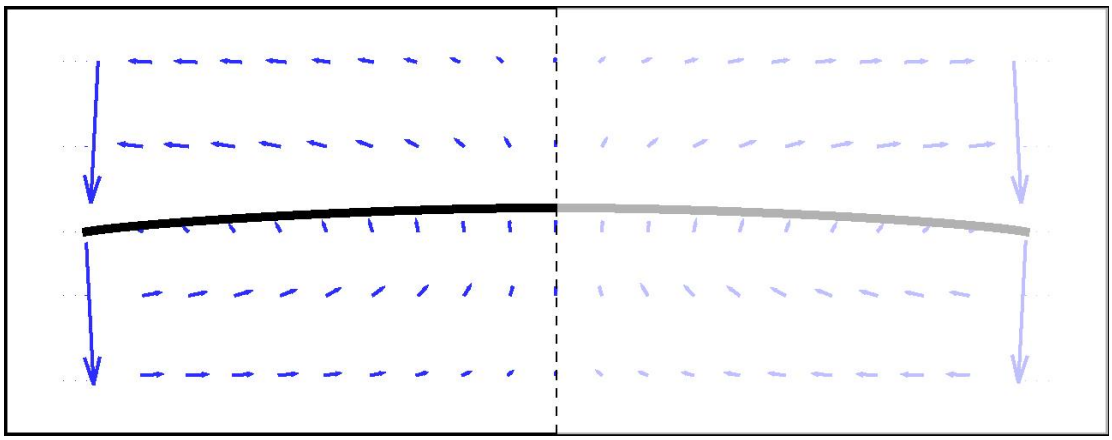

Figure C.1 Sketch of a vibrating panel coupled with ambient air on the 1st mode

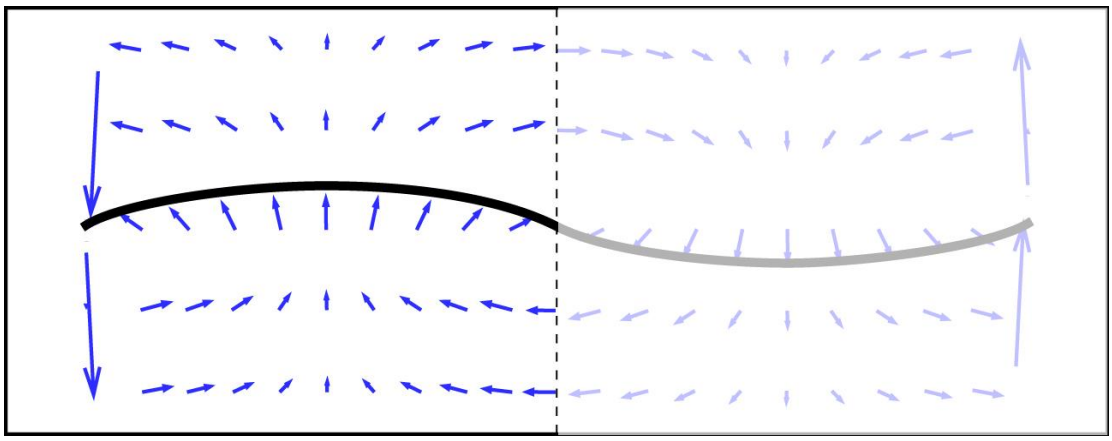

Figure C.2 Sketch of a vibrating panel coupled with ambient air on the 2nd mode

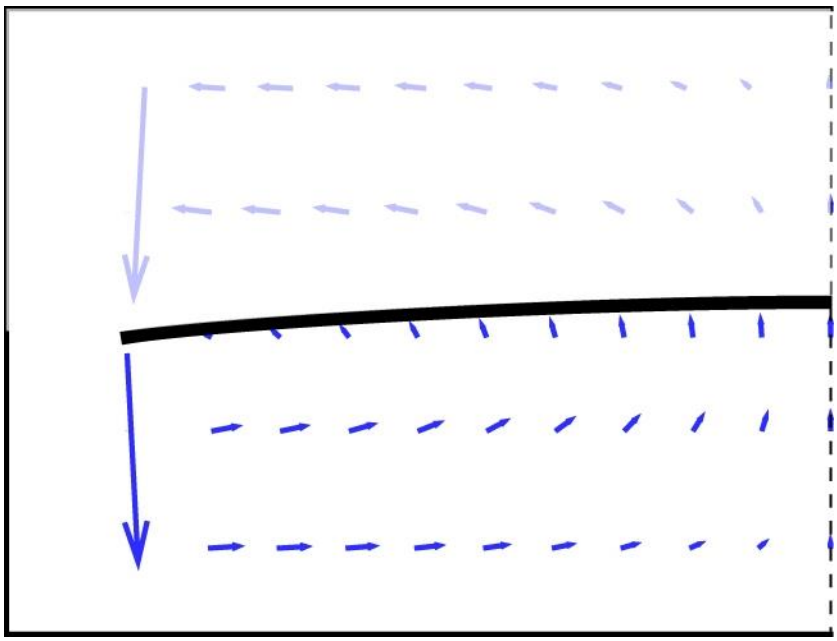

Figure C.3 Sketch of a vibrating panel coupled with ambient air on the 1st mode (½ model)

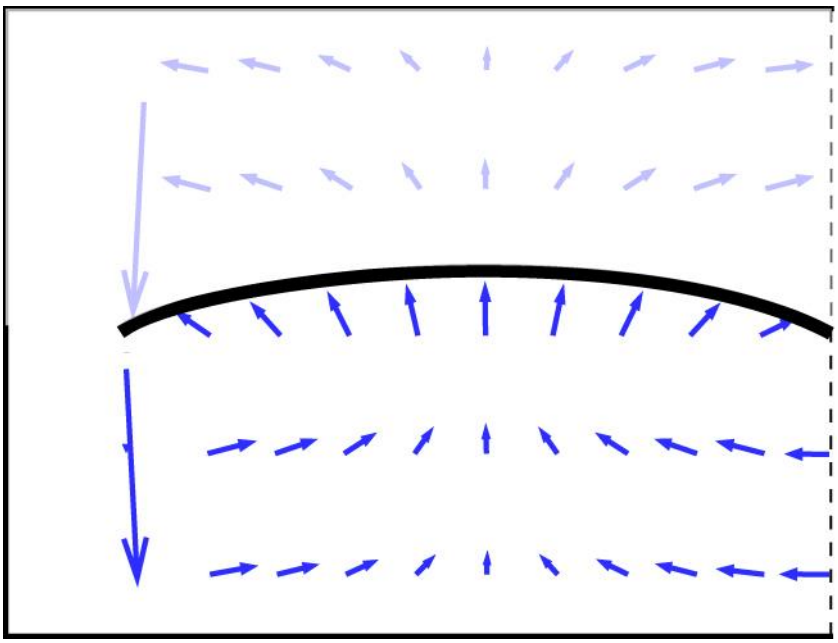

Figure C.4 Sketch of a vibrating panel coupled with ambient air on the 2nd mode (½ model)

The total mass matrix is expressed as below. u_M and v_M are the air velocity of medium part in X- and Y-direction, respectively. d' is the time derivative of panel displacement.

$$[M]\{\boldsymbol{w}\} = \begin{bmatrix} M_{11} & M_{12} & 0 & 0 & 0 & 0 & 0 \\ M_{21} & M_{22} & M_{23} & 0 & 0 & 0 & 0 \\ 0 & M_{32} & M_{33} & 0 & 0 & 0 & 0 \\ 0 & 0 & 0 & M_{44} & M_{45} & 0 & 0 \\ 0 & 0 & 0 & M_{54} & M_{55} & M_{56} & M_{57} \\ 0 & 0 & 0 & 0 & M_{65} & M_{66} & 0 \\ 0 & 0 & 0 & 0 & M_{75} & 0 & M_{77} \end{bmatrix} \begin{Bmatrix} u_L \\ u_M \\ u_U \\ v_L \\ v_M \\ v_U \\ d' \end{Bmatrix} \tag{C3}$$

Here, in the equation of the 2nd row, substituting u_U with $-u_L$.

$$[M_{21}]\{u_L\} + [M_{22}]\{u_M\} + [M_{23}]\{u_U\} = \left([M_{21}] - [M_{23}]'\right)\{u_L\} + [M_{22}]\{u_M\} \tag{C4}$$

Here, $[M_{23}]'$ is obtained by arranging the column of $[M_{23}]$ to be $[M_{23}]'\{u_L\} = [M_{23}]\{u_U\}$.

Also, from the symmetry of the model, the 3rd row can be removed because $[M_{11}]\{u_L\} = [M_{12}]\{u_M\}$ in the 1st column and $[M_{32}]\{u_M\} = [M_{33}]\{u_U\}$ in the 3rd column are the same system of the equation. Then, by determining $v_U = v_L$ the equation of the 5th row can be expressed as follows:

$$\begin{aligned} &[M_{54}]\{v_L\} + [M_{55}]\{v_M\} + [M_{56}]\{v_U\} + [M_{57}]\{d'\} \\ &\quad = \left([M_{54}] - [M_{56}]'\right)\{v_L\} + [M_{55}]\{v_M\} + [M_{57}]\{d'\} \end{aligned} \tag{C5}$$

As the same manner, $[M_{56}]'$ is arranged from the column of $[M_{56}]$ based on $[M_{23}]'\{u_L\} = [M_{23}]\{u_U\}$. Furthermore, by considering that row 4 and row 6 are the same system of equations, the total mass matrix $[M]$ is reduced as follows:

$$[M]\{\boldsymbol{w}\}=\begin{bmatrix} M_{11} & M_{12} & 0 & 0 & 0 \\ M_{21}-M'_{23} & M_{22} & 0 & 0 & 0 \\ 0 & 0 & M_{44} & M_{45} & 0 \\ 0 & 0 & M_{54}-M'_{56} & M_{55} & M_{57} \\ 0 & 0 & 0 & M_{75} & M_{77} \end{bmatrix}\begin{Bmatrix} u_L \\ u_M \\ v_L \\ v_M \\ d' \end{Bmatrix} \tag{C6}$$

The total stiffness matrix $[K]$and the total damping matrix $[C]$are expressed as follows:

$$[K]\{\boldsymbol{w}\}=\begin{bmatrix} 0 & 0 & 0 & 0 & 0 & 0 & 0 \\ 0 & 0 & 0 & 0 & 0 & 0 & 0 \\ 0 & 0 & 0 & 0 & 0 & 0 & 0 \\ 0 & 0 & 0 & 0 & 0 & 0 & 0 \\ 0 & 0 & 0 & 0 & K_{55} & 0 & K_{57} \\ 0 & 0 & 0 & 0 & 0 & 0 & 0 \\ 0 & 0 & 0 & 0 & K_{75} & 0 & K_{77} \end{bmatrix}\begin{Bmatrix} u_L \\ u_M \\ u_U \\ v_L \\ v_M \\ v_U \\ d' \end{Bmatrix} \tag{C7}$$

$$[C]\{\boldsymbol{w}\}=\begin{bmatrix} C_{11} & C_{12} & 0 & C_{14} & C_{15} & 0 & 0 \\ C_{21} & C_{22} & C_{23} & C_{24} & C_{25} & C_{26} & 0 \\ 0 & C_{32} & C_{33} & 0 & C_{35} & C_{36} & 0 \\ C_{41} & C_{42} & 0 & C_{44} & C_{45} & 0 & 0 \\ C_{51} & C_{52} & C_{53} & C_{54} & C_{55} & C_{56} & 0 \\ 0 & C_{62} & C_{63} & 0 & C_{65} & C_{66} & 0 \\ 0 & C_{72} & 0 & C_{74} & 0 & C_{76} & 0 \end{bmatrix}\begin{Bmatrix} u_L \\ u_M \\ u_U \\ v_L \\ v_M \\ v_U \\ d' \end{Bmatrix} \tag{C8}$$

In the same manner, the total stiffness matrix $[K]$and the total damping matrix $[C]$ are reduced as follows:

$$[K]\{\boldsymbol{w}\}=\begin{bmatrix} 0 & 0 & 0 & 0 & 0 \\ 0 & 0 & 0 & 0 & 0 \\ 0 & 0 & 0 & 0 & 0 \\ 0 & 0 & 0 & K_{55} & K_{57} \\ 0 & 0 & 0 & K_{75} & K_{77} \end{bmatrix}\begin{Bmatrix} u_L \\ u_M \\ v_L \\ v_M \\ d' \end{Bmatrix} \tag{C9}$$

$$[C]\{\boldsymbol{w}\} = \begin{bmatrix} C_{11} & C_{12} & C_{14} & C_{15} & 0 \\ C_{21} - C'_{23} & C_{22} & C_{24} + C'_{26} & C_{25} & 0 \\ C_{41} & C_{42} & C_{44} & C_{45} & 0 \\ C_{51} - C'_{53} & C_{52} & C_{54} + C'_{56} & C_{55} & 0 \\ 0 & C_{72} & C_{74} + C'_{76} & 0 & 0 \end{bmatrix} \begin{Bmatrix} u_L \\ u_M \\ v_L \\ v_M \\ d' \end{Bmatrix} \tag{C10}$$

Appendix D
Instability of continuous function between pressure elements

As explained in Chapter 3, the utilization of pressure approximation continuous between adjacent elements leads to the increase of the bandwidth of $[P]^{-1}$ and thus the error in calculation. This section demonstrates the problem of using the pressure approximation continuous between adjacent elements. The pressure distributions of Q_1-Q_1 element combination, continuous between adjacent pressure elements, are investigated and compared with those of Q_2-P_{-1}, discontinuous between adjacent pressure elements.

Figure D.1 illustrates the pressure distribution of Q_1-Q_1 element, where GAP is 1 mm, SIDE is 100 mm, and the panel vibrates in the fundamental mode and deforms upward. For the reason that both sides are symmetry, only the half left is presented to identify their details. Corresponding to **Figure D.1**, the plot of normalized pressure distribution at the center of the panel is presented in **Figure D.2**. From the **Figure D.1** and **D.2**, the value of pressure distribution fluctuates on each node of Y-direction. Generally, when the panel displaces upward, the pressure increases on the upper part of the panel and the pressure should drop at the lower part. However, the obtained checkerboard pressure distribution is impossible in reality.

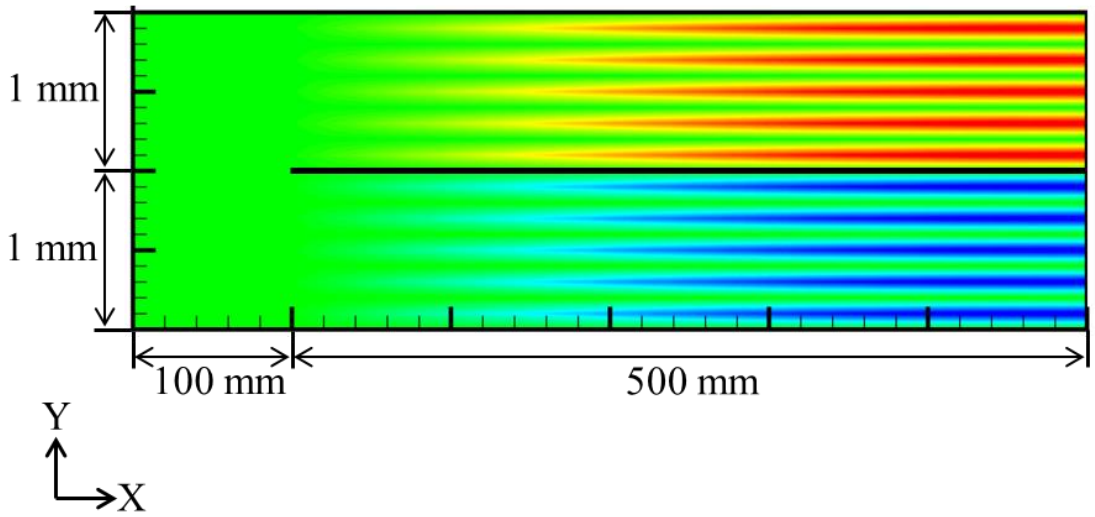

Figure D.1 Pressure distribution of Q_1-Q_1 element

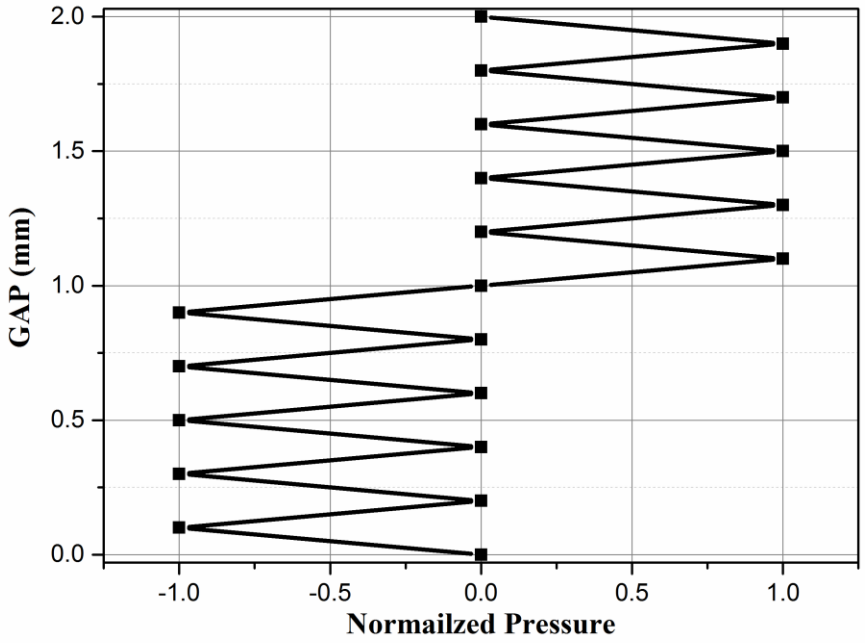

Figure D.2 Pressure distribution of Q_1-Q_1 element (at center of the panel)

To further verify the explanation, the pressure distribution of Q_1-Q_1 element is investigated with increasing the number of air elements in Y-direction to twice of

Figure D.1 condition. As shown in **Figure D.3**, even if the number of element is increased, the pressure distribution is still obtained in the checkerboard form. Moreover, the pressure distribution of Q_1-Q_1 element is examined with increasing GAP and SIDE to 1000 mm. It also illustrates the checkerboard pattern as presented in **Figure D.4**.

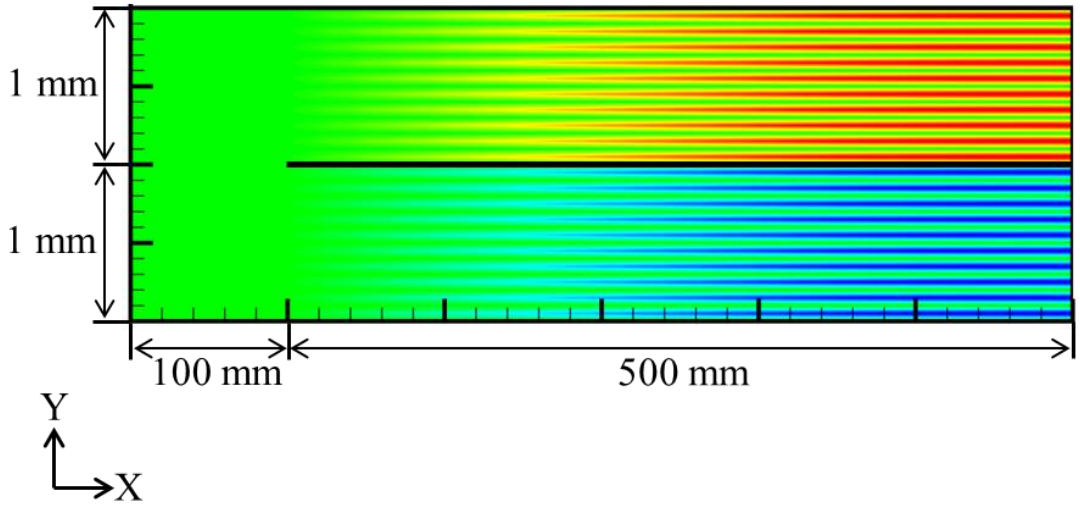

Figure D.3 Pressure distribution of Q_1-Q_1 element
(increasing the number of element in Y-direction)

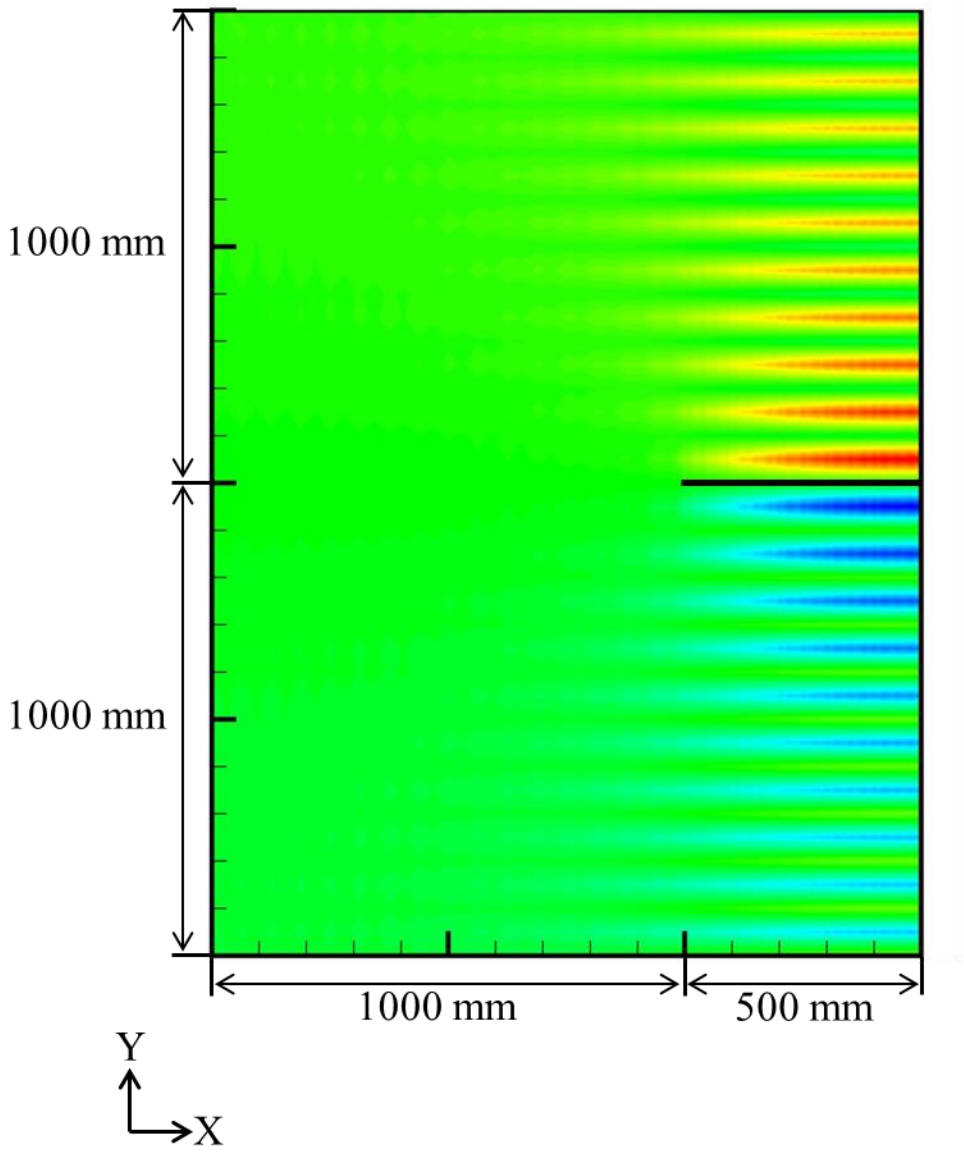

Figure D.4 Pressure distribution of Q_1-Q_1 element (increasing GAP and SIDE)

To compare the pressure distributions of Q_1-Q_1 and Q_2-P_{-1}, the identical conditions of **Figure D.1** and **Figure D.4** are adopted. The pressure distribution of Q_2-P_{-1} element, where GAP is 1 mm and SIDE is 100 mm is presented in **Figure D.5** and its plot of normalized pressure distribution at the center of the panel is presented in **Figure D.6**. The pressure distribution of Q_2-P_{-1} element, where GAP and SIDE are 1,000 mm is presented in **Figure D.7**. The pressure distributions obtained by using

Q_2-P_{-1} element are reasonable. The investigation in this section can confirm the explanation of selecting the discontinuous elements for the approximation of pressure field in Chapter 3.

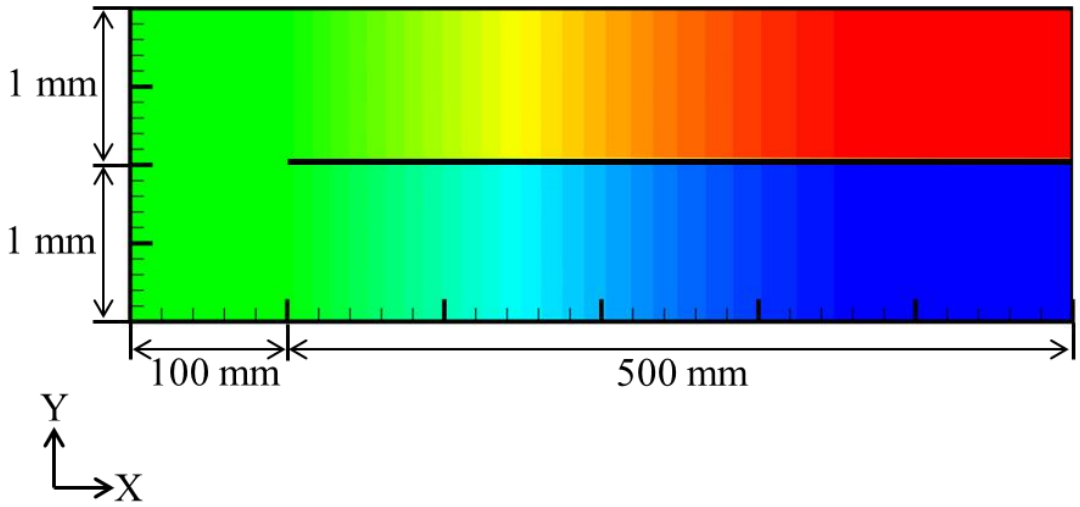

Figure D.5 Pressure distribution of Q_2-P_{-1} element

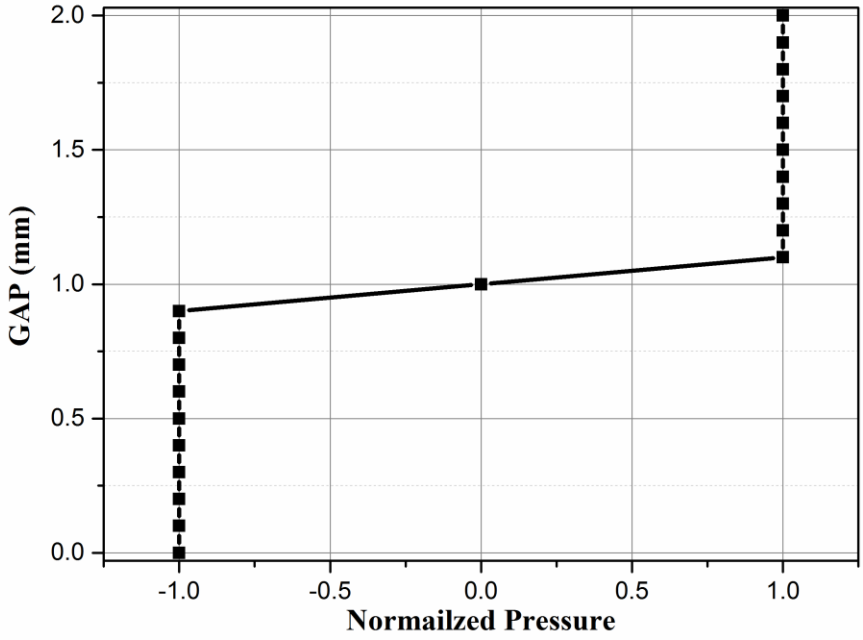

Figure D.6 Pressure distribution of Q_2-P_{-1} element (at center of the panel)

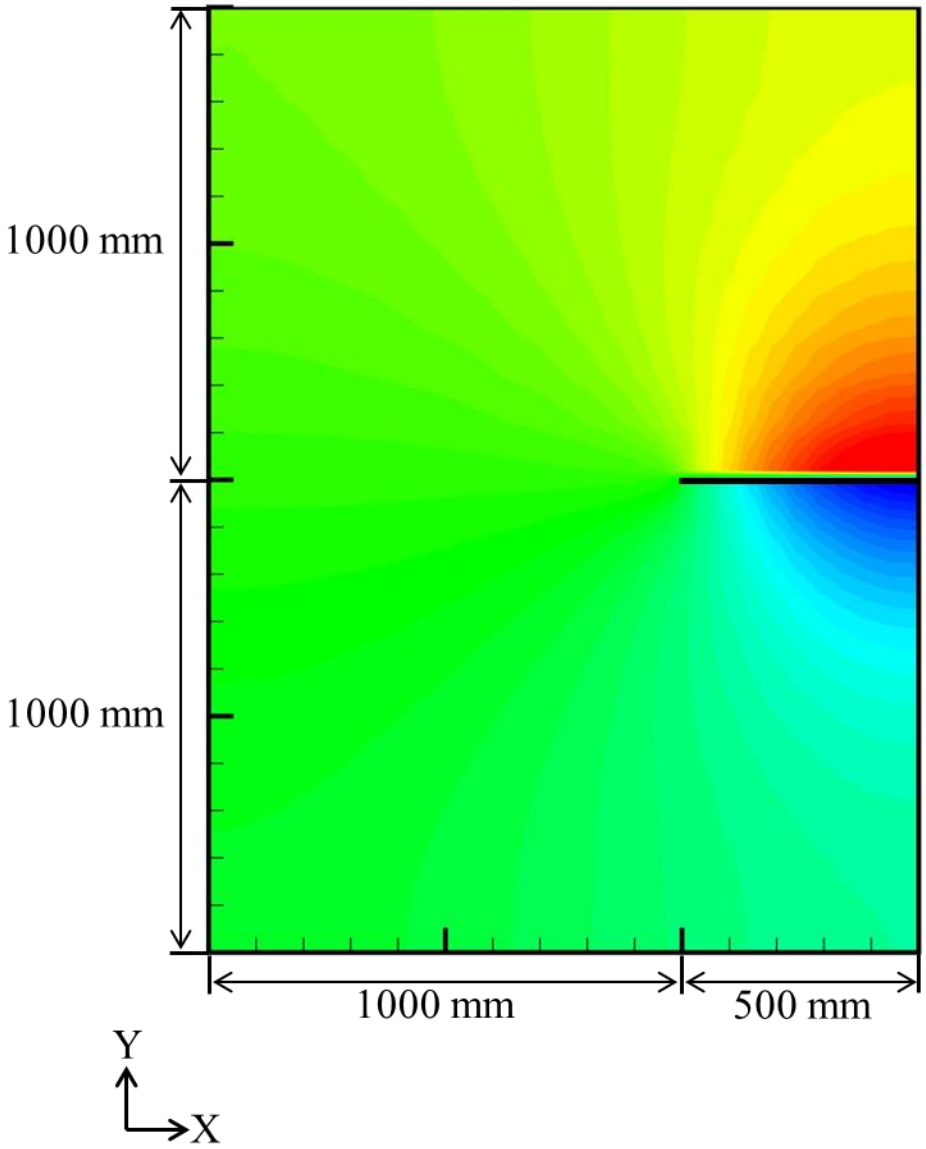

Figure D.7 Pressure distribution of Q_2-P_{-1} element (increasing GAP and SIDE)

Appendix E
Validation of fluid region

In this section, the validity of the air region is examined by comparing the air flow velocity vector and pressure distributions obtained from finite element model to those from finite difference model.

E.1 Finite difference modeling

Unlike the finite element model, the finite difference model is formulated by including the convective acceleration term into the Navier-Stokes equations in order to clarify that the spatial effect can be neglected in this study. The governing equations of the air region can be expressed by the Navier-Stokes equations and the continuity equation in non-dimensional form as follows:

$$\frac{\partial U}{\partial T}+U\frac{\partial U}{\partial X}-V\frac{\partial U}{\partial Y}=-\frac{\partial P}{\partial X}+\frac{1}{\mathrm{Re}}\left(\frac{\partial^2 U}{\partial X^2}+\frac{\partial^2 U}{\partial Y^2}\right) \tag{E1}$$

$$\frac{\partial V}{\partial T}+U\frac{\partial V}{\partial X}-V\frac{\partial V}{\partial Y}=-\frac{\partial P}{\partial X}+\frac{1}{\mathrm{Re}}\left(\frac{\partial^2 V}{\partial X^2}+\frac{\partial^2 V}{\partial Y^2}\right) \tag{E2}$$

$$\frac{\partial U}{\partial X}+\frac{\partial V}{\partial Y}=0 \tag{E3}$$

Here, the following dimensionless variables are used as follows:

$$X=\frac{x}{L_0},\ Y=\frac{y}{L_0},\ U=\frac{u}{U_0},\ V=\frac{v}{V_0},\ T=\frac{tU_0}{L_0},\ P=\frac{p}{\rho_0 U_0^2},\ \mathrm{Re}=\frac{\rho U_0 L_0}{\mu} \tag{E4}$$

The subscript zero refers a dimensional variable. L, U, V, ρ, p, t, μ, and Re denote length, velocity in x direction, velocity in y direction, mass density, pressure, time, viscosity coefficient, and the Reynolds number, respectively.

Appendix E
Validation of fluid region

The governing equations are discretized by the finite difference method, with a staggered grid in which the pressure is defined at the cell center and the velocity components are defined at the cell boundaries as shown in **Figure E.1.**

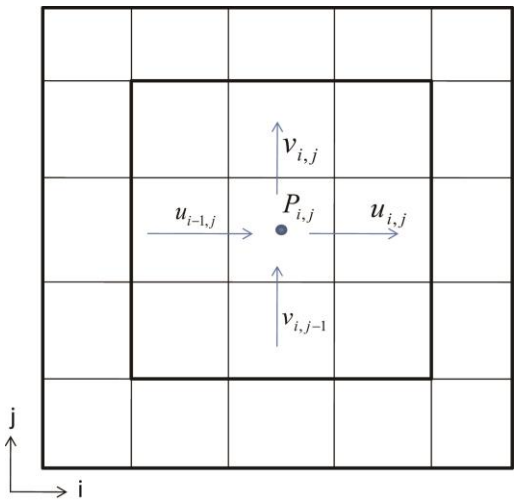

Figure E.1 Staggered grid

The continuity and momentum equation can be discretized as follows:

$$DIV_{i,j}^{n+1} = 0 \tag{E5}$$

$$\frac{U_{i,j}^{n+1} - U_{i,j}^{n}}{\Delta T} + CNVU_{i,j}^{n} = -\frac{P_{i+1,j}^{n+1} - P_{i,j}^{n+1}}{\Delta X} + DIFU_{i,j}^{n} \tag{E6}$$

$$\frac{V_{i,j}^{n+1} - V_{i,j}^{n}}{\Delta T} + CNVV_{i,j}^{n} = -\frac{P_{i,j+1}^{n+1} - P_{i,j}^{n+1}}{\Delta Y} + DIFV_{i,j}^{n} \tag{E7}$$

$$DIV = \frac{\partial U}{\partial X} + \frac{\partial V}{\partial Y},\ CNVU = U\frac{\partial U}{\partial X} + V\frac{\partial U}{\partial Y},\ CNVV = U\frac{\partial V}{\partial X} + V\frac{\partial V}{\partial Y},$$

$$DIFU = \frac{1}{\mathrm{Re}}\left(\frac{\partial^2 U}{\partial X^2} + \frac{\partial^2 U}{\partial Y^2}\right),\ DIFV = \frac{1}{\mathrm{Re}}\left(\frac{\partial^2 V}{\partial X^2} + \frac{\partial^2 V}{\partial Y^2}\right) \tag{E8}$$

Where superscripts n and n+1 represent current and next time step, respectively and subscripts denote the corresponding cell face position as shown in **Figure E.1**. The pressure gradients and diffusion terms are approximated using a second-order central

difference scheme, while the convective terms are approximated by a first-order upwind difference scheme.

The continuity equation is discretized at *i,j*

$$DIV_{i,j}^{n+1} = \frac{U_{i,j}^{n+1} - U_{i-1,j}^{n+1}}{\Delta X} + \frac{V_{i,j}^{n+1} - V_{i,j-1}^{n+1}}{\Delta Y} = 0 \tag{E9}$$

The *U*-momentum equation is discretized at *i,j*

$$CNVU_{i,j}^{n} = \left(U_{i,j} \frac{U_{i+1,j} - U_{i-1,j}}{2\Delta X} - \frac{|U_{i,j}|\Delta X}{2} \frac{U_{i-1,j} - 2U_{i,j} + U_{i+1,j}}{\Delta X^2} \right)^n + \left(V \frac{U_{i,j+1} - U_{i,j-1}}{2\Delta Y} - \frac{|V|\Delta Y}{2} \frac{U_{i,j-1} - 2U_{i,j} + U_{i,j+1}}{\Delta Y^2} \right)^n \tag{E10}$$

$$V = \frac{V_{i,j} + V_{i,j-1} + V_{i+1,j} + V_{i+1,j-1}}{4} \tag{E11}$$

$$DIFU_{i,j}^{n} = \frac{1}{\mathrm{Re}} \left(\frac{U_{i-1,j} - 2U_{i,j} + U_{i+1,j}}{\Delta X^2} + \frac{U_{i,j-1} - 2U_{i,j} + U_{i,j+1}}{\Delta Y^2} \right)^n \tag{E12}$$

The *V*-momentum equation is discretized at *i,j*

$$CNVV_{i,j}^{n} = \left(U \frac{V_{i+1,j} - V_{i-1,j}}{2\Delta X} - \frac{|U|\Delta X}{2} \frac{V_{i-1,j} - 2V_{i,j} + V_{i+1,j}}{\Delta X^2} \right)^n + \left(V_{i,j} \frac{V_{i,j+1} - V_{i,j-1}}{2\Delta Y} - \frac{|V_{i,j}|\Delta Y}{2} \frac{V_{i,j-1} - 2V_{i,j} + V_{i,j+1}}{\Delta Y^2} \right)^n \tag{E13}$$

$$U = \frac{U_{i,j} + U_{i,j-1} + U_{i+1,j} + U_{i+1,j-1}}{4} \tag{E14}$$

$$DIFV_{i,j}^{n} = \frac{1}{\mathrm{Re}} \left(\frac{V_{i-1,j} - 2V_{i,j} + V_{i+1,j}}{\Delta X^2} + \frac{V_{i,j-1} - 2V_{i,j} + V_{i,j+1}}{\Delta Y^2} \right)^n \tag{E15}$$

The calculation of velocity and pressure fields is performed by HSMAC (Highly Simplified Marker And Cell) method, in which the pressure and velocity components are corrected iteratively until the continuity equation is satisfied. The

equation for the pressure correction is expressed as

$$ {}^{m+1}P_{i,j}^{n+1} = {}^{m}P_{i,j}^{n+1} - \frac{\omega\, {}^{m}DIV_{i,j}^{n+1}}{\left(\frac{\partial DIV_{i,j}}{\partial P_{i,j}}\right)^{n+1}} = {}^{m}P_{i,j}^{n+1} + {}^{m}\delta P_{i,j}^{n+1} \tag{E16} $$

where the superscript m is the variable representing the number of iterations and ω is relaxation coefficient. Generally the relaxation coefficient is determined to be about 1.7.

The iterative procedure of this method consists of the following steps: First, the velocity component is predicted using the discretized momentum equation (E6) and (E7). Then, the divergence of each discretized cell is calculated by the discretized continuity equation (E9). After that, the pressure is corrected iteratively by using

$$ {}^{m}\delta P_{i,j}^{n+1} = -\frac{\omega\, {}^{m}DIV_{i,j}^{n+1}}{2\Delta T\left(\frac{1}{\Delta X^{2}} + \frac{1}{\Delta Y^{2}}\right)} \tag{E17} $$

After the pressure correction, the velocity is updated. The procedure is reiterated until the continuity equation is satisfied.

In order to analyze the air domain by finite difference method, the following boundary condition is given as the theoretical expression of the transient mode of the panel without solving the equation as a rigid wall.

$$ V\left(X, \frac{Y}{2}\right) = A \cdot \sin\left(\frac{n\pi X}{L}\right)\cos\left(2\pi f_0 T\right) \tag{E18} $$

where f_0 refers the natural frequency determined by the finite element model and A is the maximum amplitude of the panel.

E.2 Comparison of air flow velocity vector and pressure distribution

The comparisons of air flow velocity vector and pressure distribution, while the panel vibrates and drives the ambient air, are presented here in various GAP and SIDE conditions. The panel length and vibration amplitude are determined to be 1000 mm and 1 mm, respectively.

First, the SIDE is set for 1000 mm, which is large enough to neglect the effect of lateral wall while the GAP is set to be 1 mm. The flow velocity vector (SIDE of 1000 mm and GAP of 1 mm) obtained from finite element model and the finite difference model is presented in **Figure E.2** and **E.3**, respectively. For the reason that both sides are symmetry, only the half left is presented throughout this section. The flow velocity vector of both models shows well agreement. At the center of the panel, the flow vectors are dominant in vertical direction and tend to change to horizontal direction when they approach the panel end. At the panel end, the flow vectors wrap around in the vicinity rather than the entire space up to the lateral wall.

To differentiate between finite element and finite difference flow velocity vector, the magnified superposition of finite element and finite difference flow velocity vector is presented in **Figure E.4.** The magnification is pointed around the panel end. The back vector belongs to the finite element model and the pink vector is the finite difference model. The flow velocity vectors obtained from finite element and finite difference model are fairly identical. They appear as poiseuille flow due to the dominance of viscous effect when the GAP is small.

The pressure distribution (SIDE of 1000 mm and GAP of 1 mm) obtained from finite element model and the finite difference model is presented in **Figure E.5**

and **E.6**, respectively. Both results show good agreement where the pressure is constant in vertical direction and the pressure magnitude gradually decreases from the center of the panel. By comparing the maximum pressure magnitude, the difference between both models is only 1.63%.

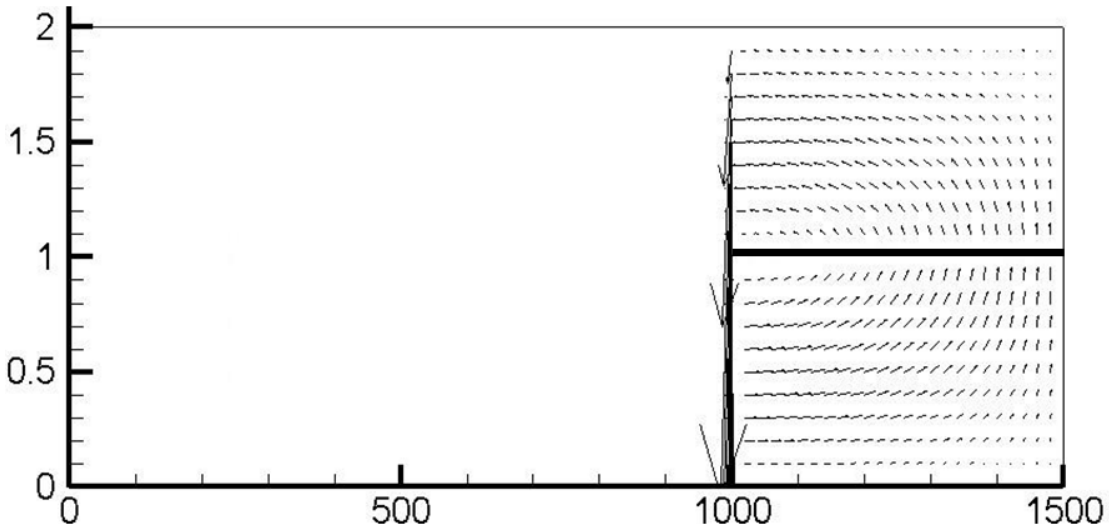

Figure E.2 FEM flow velocity vector: GAP of 1 mm and SIDE of 1000 mm

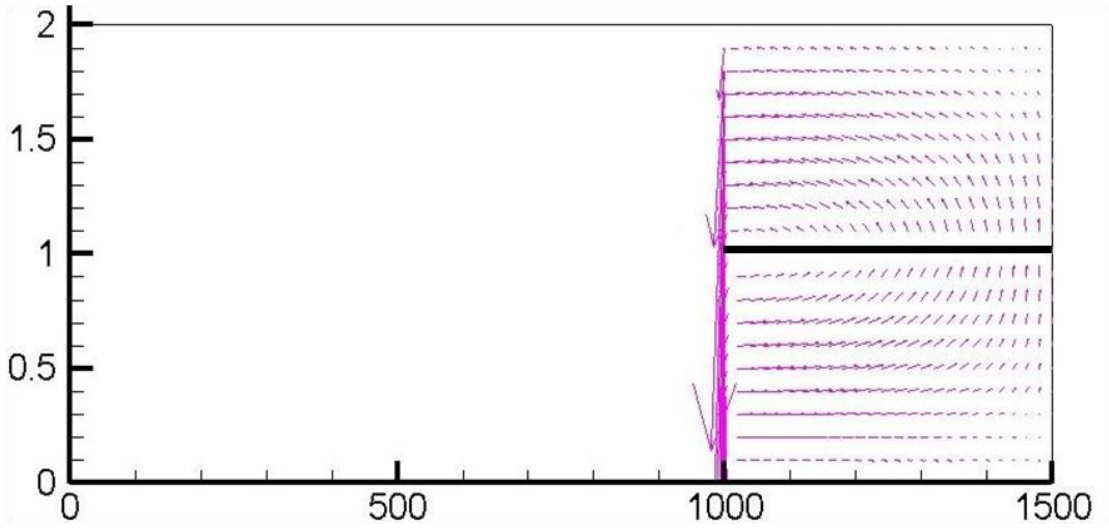

Figure E.3 FDM flow velocity vector: GAP of 1 mm and SIDE of 1000 mm

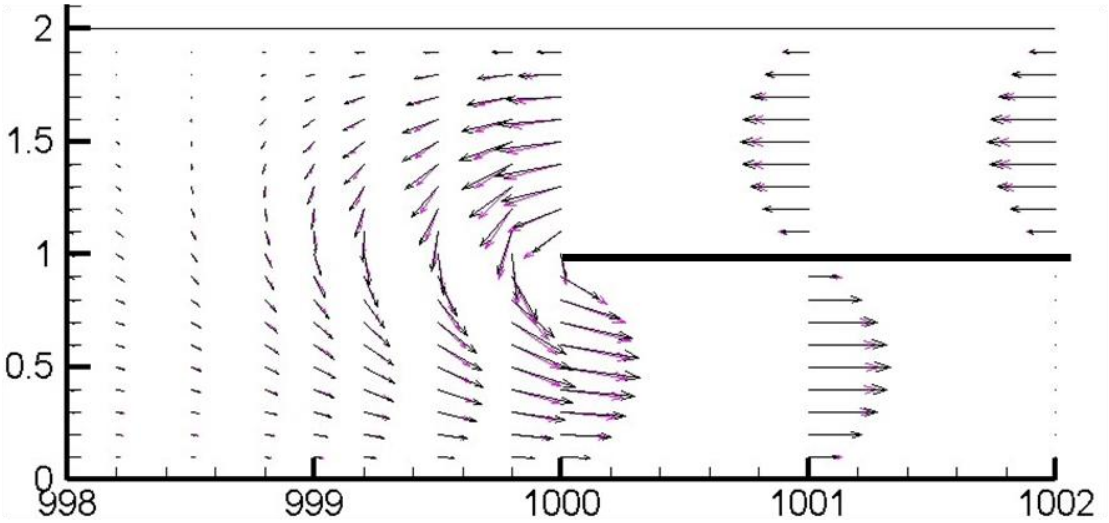

Figure E.4 Magnified superposition of FEM and FDM flow velocity vector: GAP of 1 mm and SIDE of 1000 mm

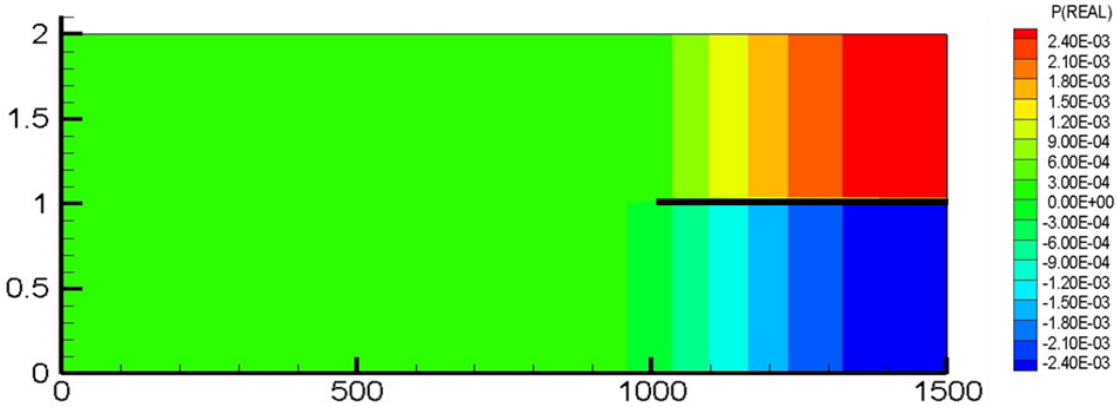

Figure E.5 FEM pressure distribution: GAP of 1 mm and SIDE of 1000 mm

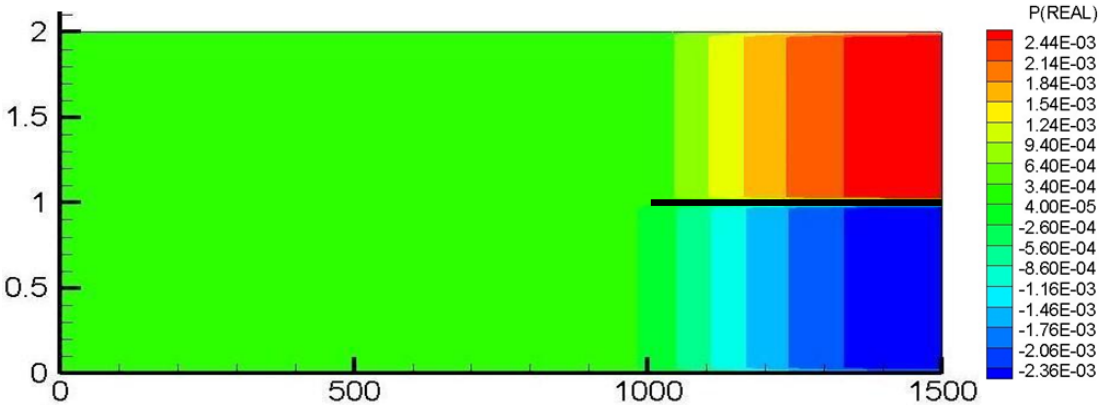

Figure E.6 FDM pressure distribution: GAP of 1 mm and SIDE of 1000 mm

Secondly, the GAP is set to be 10 mm while the SIDE is still same at 1000 mm. The flow velocity vector (SIDE of 1000 mm and GAP of 10 mm) obtained from finite element model and the finite difference model is presented in **Figure E.7** and **E.8**, respectively. The trends of the air flow velocity vector are in good agreement even the GAP is changed. The magnified superposition of finite element and finite difference flow velocity vector around the panel end is presented in **Figure E.9**. The back and pink vector belong to the finite element and finite difference model, respectively. The flow velocity vector obtained from both model is similar to laminar flow. When compared with the flow profile of the previous condition, the ratio of boundary layer occupying the air layer decreases referring to the decrease of viscous effect.

The pressure distribution (SIDE of 1000 mm and GAP of 10 mm) obtained from finite element model and the finite difference model is presented in **Figure E.10** and **E.11**, respectively. As same as the previous condition, both results show good agreement and the pressure is constant in vertical direction and its magnitude gradually decreases from the center of the panel. By comparing the maximum pressure magnitude, the difference between both models is only 0.99%. The better accuracy as compared with the condition of GAP of 1 mm is because the large GAP results the less complicated influence of air flow.

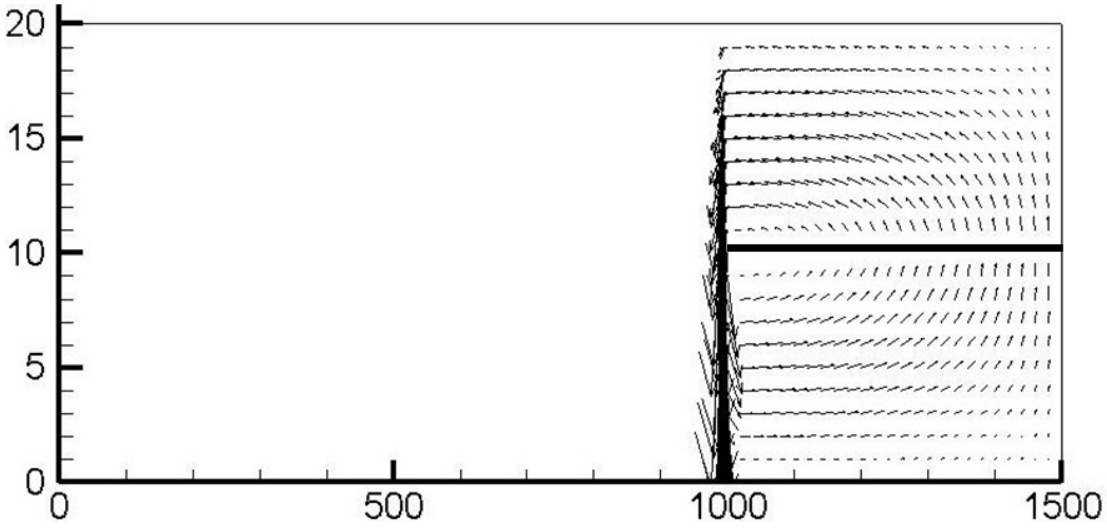

Figure E.7 FEM flow velocity vector: GAP of 10 mm and SIDE of 1000 mm

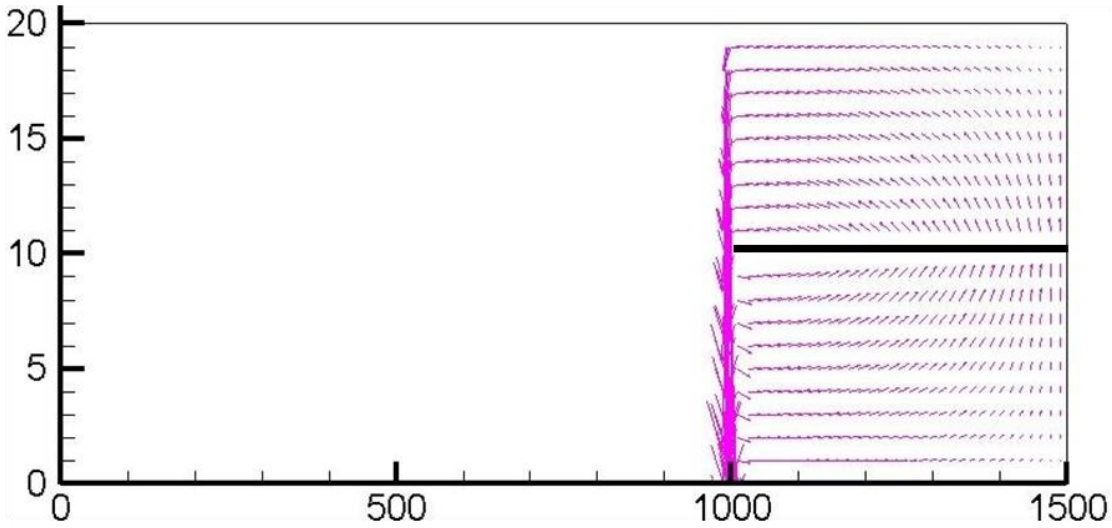

Figure E.8 FDM flow velocity vector: GAP of 10 mm and SIDE of 1000 mm

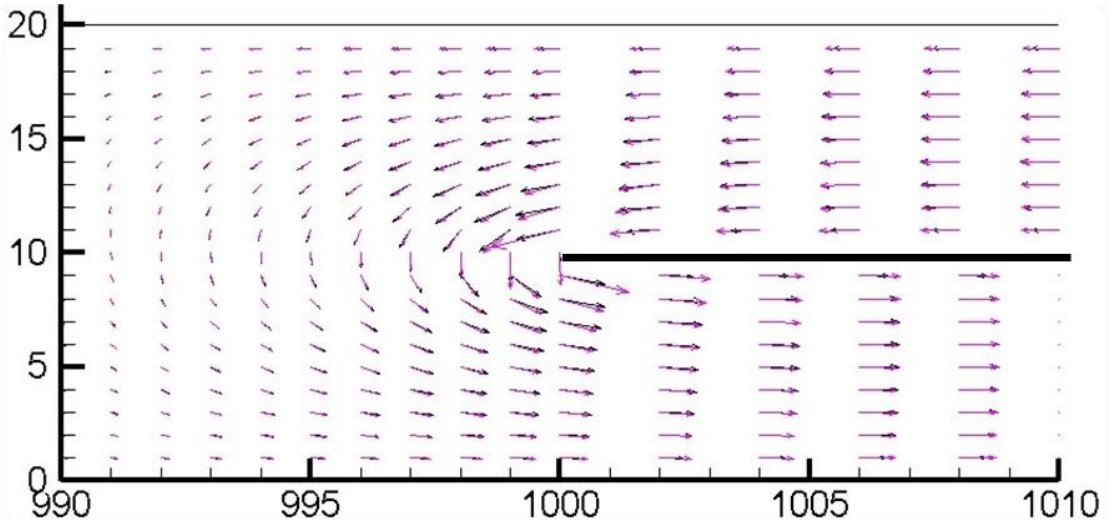

Figure E.9 Magnified superposition of FEM and FDM flow velocity vector: GAP of 10 mm and SIDE of 1000 mm

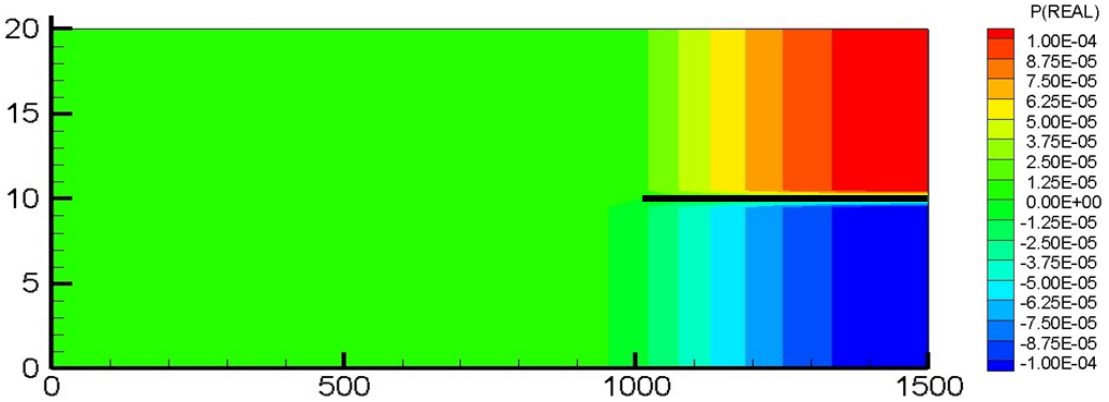

Figure E.10 FEM pressure distribution: GAP of 10 mm and SIDE of 1000 mm.

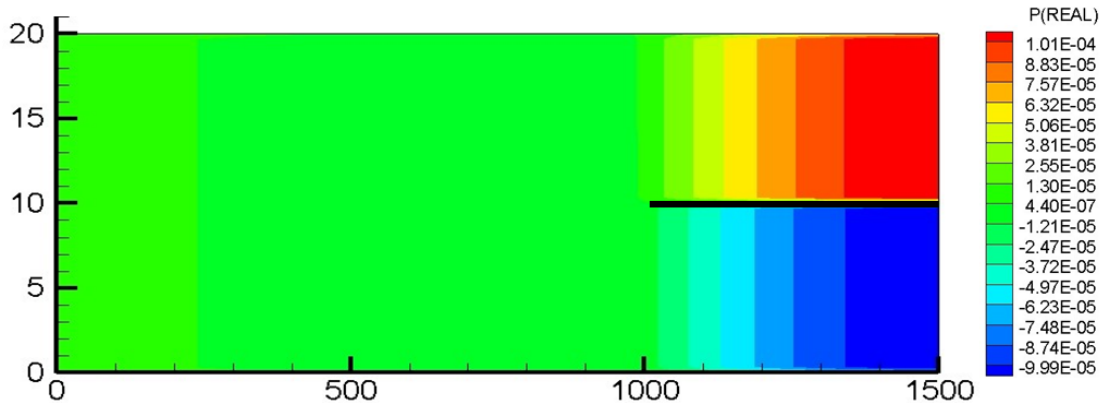

Figure E.11 FDM pressure distribution: GAP of 10 mm and SIDE of 1000 mm

Thirdly, the SIDE is set to be 100 mm while the GAP is 1 mm. The flow velocity vector (SIDE of 100 mm and GAP of 1 mm) obtained from finite element model and the finite difference model is presented in **Figure E.12** and **E.13**, respectively. The trends of the air flow velocity vector are in good agreement even the SIDE is changed. The magnified superposition of finite element and finite difference flow velocity vector around the panel end is presented in **Figure E.14**. The back and pink vector belong to the finite element and finite difference model, respectively. The flow velocity vector obtained from both model is similar to poiseuille flow.

The pressure distribution (SIDE of 100 mm and GAP of 1 mm) obtained from finite element model and the finite difference model is presented in **Figure E.15** and **E.16**, respectively. The tendency of results obtained from both models is in good agreement and similar to those of previous section. By comparing the maximum pressure magnitude, the difference between both models is 1.89%.

In summary, although the GAP and/or SIDE are changed, the air flow velocity vector and pressure distribution obtained from both models still shows good agreement. Thus, the validity of fluid region is confirmed in this part.

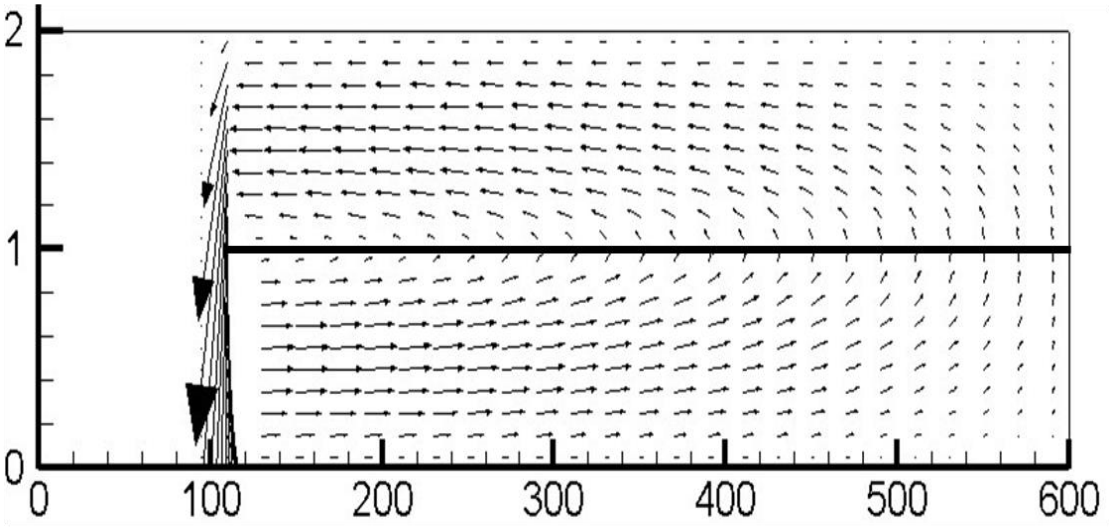

Figure E.12 FEM flow velocity vector: GAP of 1 mm and SIDE of 100 mm

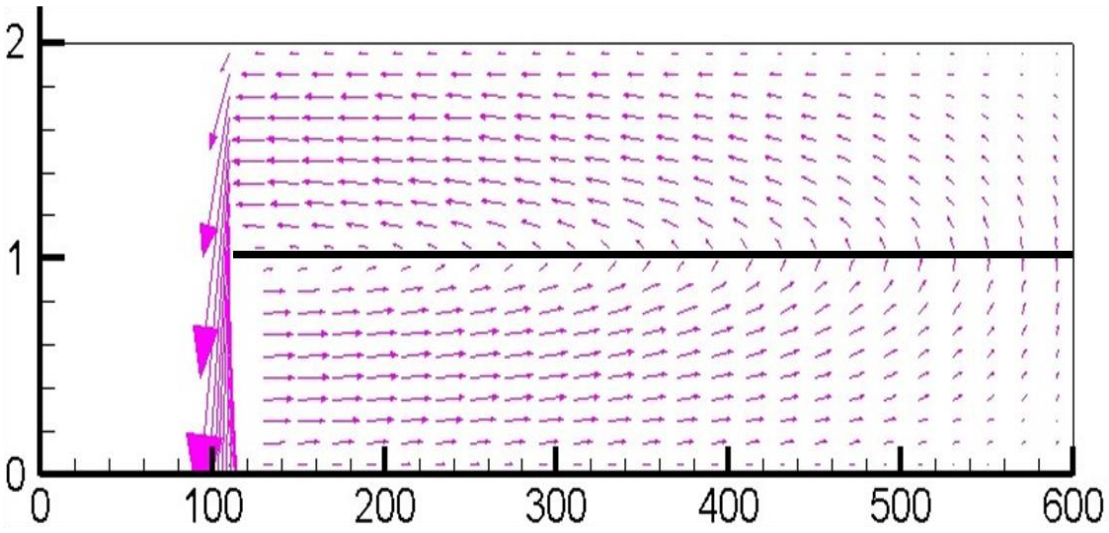

Figure E.13 FDM flow velocity vector: GAP of 1 mm and SIDE of 100 mm

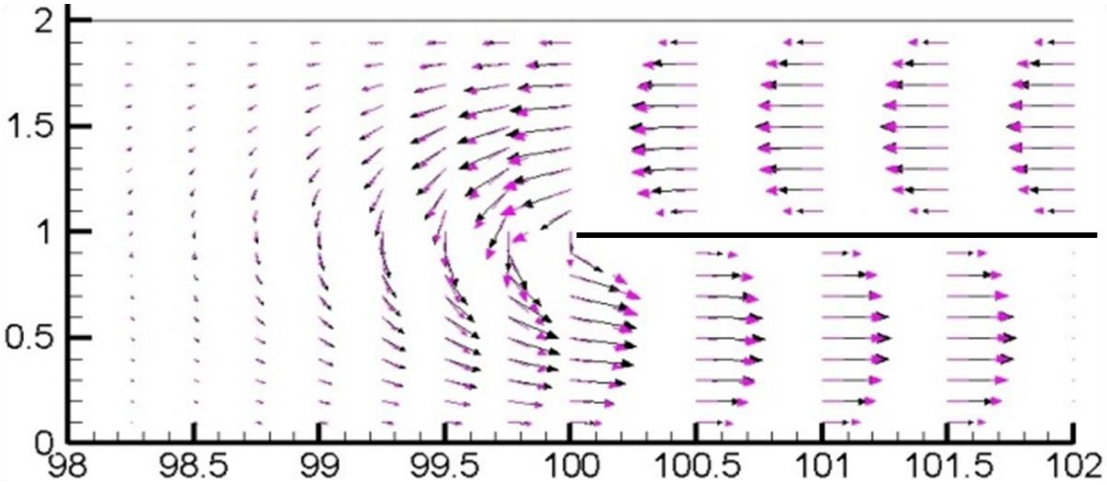

Figure E.14 Magnified superposition of FEM and FDM flow velocity vector: GAP of 1 mm and SIDE of 100 mm

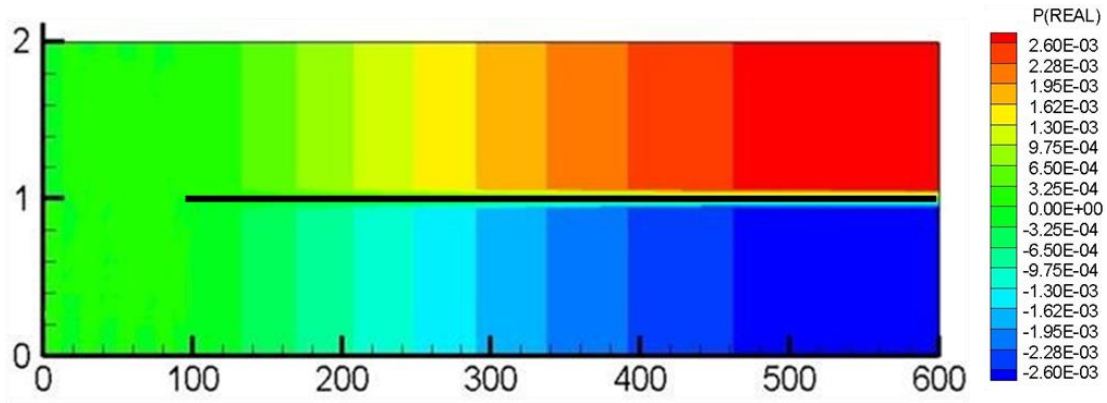

Figure E.15 FEM pressure distribution: GAP of 1 mm and SIDE of 100 mm

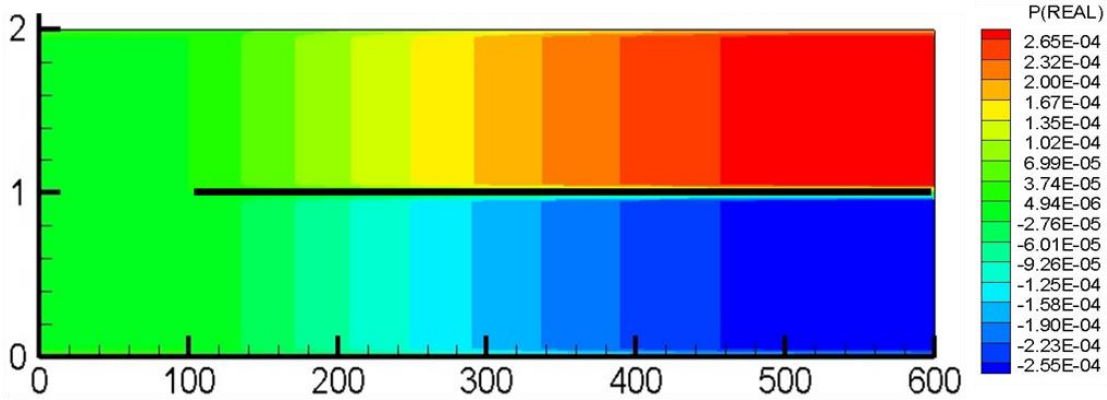

Figure E.16 FDM pressure distribution: GAP of 1 mm and SIDE of 100 mm

In addition, the validation of the fluid region is further studied by varying the vibrational amplitude of the panel. The maximum pressure magnitudes obtained from finite difference and finite element model are compared in the condition of GAP of 1 mm and SIDE of 1000 mm. As shown in **Figure E.17 (a)**, when the amplitude is less than 1 mm, the difference of pressure magnitudes obtained from finite difference and finite element model is less than 2%, which reveals the reliability of the finite element model. On the other hand, when the amplitude is greater than 1 mm as shown in **Figure E.17 (b)**, the difference gradually increases because the accuracy of the finite element analysis declines outside the range of micro-vibration. However, the vibration amplitude of sandwich panels is considered to be very small because the linear eigenvalue problem is performed in this study. The difference of the results obtained from finite difference and finite element model is acceptable. Therefore, the reliability of the finite element model is verified in this section.

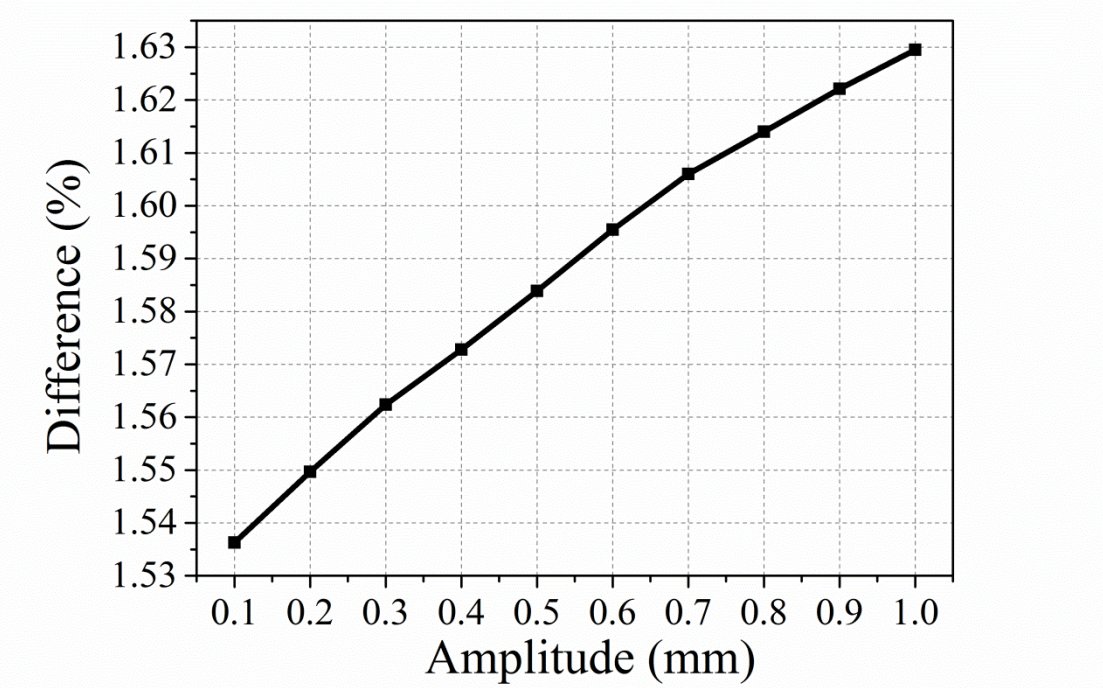

(a)

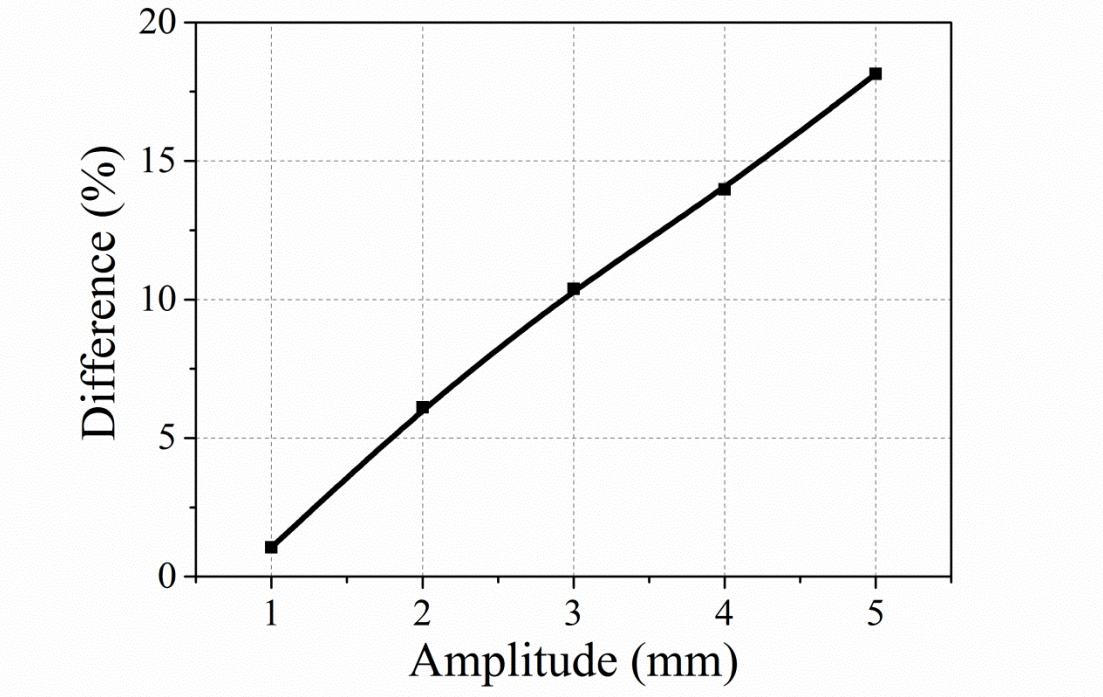

(b)

Figure E.17 Difference of pressure magnitude obtained from finite difference and finite element model **(a)** small amplitude **(b)** large amplitude

Acknowledgements

My deepest gratitude goes first to Prof. Naoyuki Watanabe for his expert guidance and untiring encouragements during my PhD study at Tokyo Metropolitan University. I would like to extend my gratitude to my dissertation committee: Prof. Koichi Kitazono, Prof. Hironori Sahara, and Prof. Ayumu Inasawa, for their insightful review, comments, and encouragement. I would like to express a huge thanks to Tokyo Metropolitan Government for the generous funding and scholarship under the project of Asian Network of Major Cities 21 and Asian Human Resources Fund program. I would like to deeply thank to Asst. Prof. Dr. Preecha Karin, who recommended me for this excellent scholarship. I would like to express my sincerest thanks and appreciation to Asst. Prof. Dr. Monsak Pimsarn, Dr. Sarawut Lerspalungsanti, Dr. Sittikorn Lapapong, and Dr. Augustine Supachai Supavai for their generous support, guidance and encouragement to pursue my PhD degree.

I would like to gratefully acknowledge the support from former and current members of Watanabe Laboratory, especially Dr. Satoshi Morooka, Dr. Atsushi Kondo, Dr. Arief Yuhanto, Dr. Agus Trilaksono, Dr. Ridlo Nasution, Dr. Jonny Herwan, Mr. Worawat Parasilp, Mr. Prabij Joshi, Mr. Yosuke Oishi, Mr. Yasuhito Mikami, Mr. Norimasa Goto, Mr. Takuya Yoshida, Ms Tomoko Inoue, Mr. Naoto Yamada et al. Many thanks to Prof. Ayumu Inasawa, my resident advisor, and all staffs of Tokyo Metropolitan University for their kind help and support.

Most important, I would like to thank my parent and sister for all their lover and support. I gratefully dedicate this success to my parents who always stand by me with encouragement and financial support.

Vita

Saharat Chanthanumataporn was born in Bangkok, capital city of Thailand, in November 1986. He received his bachelor of engineering from the Department of Mechanical Engineering, Silpakorn University, Thailand, in 2009. He received his master of automotive engineering (TAIST-Tokyo Tech program), from King Mongkut's Institute of Technology Ladkrabang, Thailand, in 2013. He served as research assistant for design and development of regenerative braking system for retrofitted electric vehicle at National Science and Technology Development Agency, Thailand, 2011-2013. He pursued his doctoral degree at the Department of Aerospace Engineering, Tokyo Metropolitan University, Japan, Under the Asian Human Resources Fund program, in October 2013.